Multiple Detection and Tracking in Complex Time-Varying Environments

by

Meng Zhou

A Dissertation Presented in Partial Fulfillment
of the Requirement for the Degree
Doctor of Philosophy

Approved November 2014 by the
Graduate Supervisory Committee:

Antonia Papandreou-Suppappola, Chair
Cihan Tepedelenlioglu
Narayan Kovvali
Visar Berisha

ARIZONA STATE UNIVERSITY

December 2014

ABSTRACT

This work considers the problem of multiple detection and tracking in two complex time-varying environments, urban terrain and underwater. Tracking multiple radar targets in urban environments is first investigated by exploiting multipath signal returns, wideband underwater acoustic (UWA) communications channels are estimated using adaptive learning methods, and multiple UWA communications users are detected by designing the transmit signal to match the environment.

For the urban environment, a multi-target tracking algorithm is proposed that integrates multipath-to-measurement association and the probability hypothesis density method implemented using particle filtering. The algorithm is designed to track an unknown time-varying number of targets by extracting information from multiple measurements due to multipath returns in the urban terrain. The path likelihood probability is calculated by considering associations between measurements and multipath returns, and an adaptive clustering algorithm is used to estimate the number of target and their corresponding parameters. The performance of the proposed algorithm is demonstrated for different multiple target scenarios and evaluated using the optimal subpattern assignment metric.

The underwater environment provides a very challenging communication channel due to its highly time-varying nature, resulting in large distortions due to multipath and Doppler-scaling, and frequency-dependent path loss. A model-based wideband UWA channel estimation algorithm is first proposed to estimate the channel support and the wideband spreading function coefficients. A nonlinear frequency modulated signaling scheme is proposed that is matched to the wideband characteristics of the underwater environment. Constraints on the signal parameters are derived to optimally reduce multiple access interference and the UWA channel effects. The signaling scheme is compared to a code division multiple access (CDMA) scheme to demon-

strate its improved bit error rate performance. The overall multi-user communication system performance is finally analyzed by first estimating the UWA channel and then designing the signaling scheme for multiple communications users.

TABLE OF CONTENTS

Page

LIST OF FIGURES

LIST OF TABLES

LIST OF ACRONYMS

ACE Adaptive Clustering Estimation

BER Bit Error Rate

CDMA Code-Division Multiple Access

CT Constant Turn

CV Constant Velocity

DLS Direct Least-Square

DP-GMM Dirichlet Process Gaussian Mixture Modeling

FDMA Frequency-Division Multiple Access

FDR False Discovery Rate

FM Frequency Modulation

FOV Field-of-View

FT Fourier Transform

HFM Hyperbolic Frequency Modulated

IF Instantaneous Frequency

IMM Interactive Multiple Model

INF Intensity Function

JPDA Joint Probabilistic Data Association

LFM Linear Frequency Modulated

LOS Line-of-Sight

LTV Linear Time-Varying

MAI Multiple Access Interference

MHT Multiple Hypothesis Tracking

MMA Measurement-to-Multipath Association

MPD Matching Pursuit Decomposition

MT Mellin Transform

NFM Nonlinear Frequency Modulated

NSF Narrowband Spreading Function

OFDM Orthogonal Frequency-Division Multiplex

OSPA Optimal Subpattern Assignment

PF Particle Filter

PHD Probability Hypothesis Density

PLP Path Likelihood Probability

PN Pseudo Noise

PPV Positive Predictive Value

RFS Random Finite Set

RMSE Root Mean-Squared Error

SDMA Space-Division Multiple Access

SNR Signal-to-Noise Ratio

TDMA Time-Division Multiple Access

TPR True Positive Rate

UWA Underwater Acoustic

WSF Wideband Spreading Function

Chapter 1

INTRODUCTION

1.1   Signal Transmission in Complex Environments

Multiple detection and tracking in complex environments is important in numer-
ous applications including radar, sonar and communications. The complex envi-
ronment can cause various undesired effects, such as multipath reflections in ur-
ban environments and wideband distortions in underwater acoustic communications,
which make detection and tracking challenging. Therefore, the detection and tracking
schemes and processing methodologies need to be designed to match these environ-
ments.

During the last decades, target tracking has been widely used for civil and mili-
tary applications such as surveillance, navigation and traffic control [2, 3]. The key
problem of target tracking is to simultaneously estimate and track the target state pa-
rameters, such as location and velocity. After transmission, a signal is reflected from
the target and the return signal is matched to the transmitted signal to determine if
the presence of the target can be detected. Originally designed for rural environments,
where the line-of-sight (LOS) signal is most often available, radar systems have been
widely used as a sensing modality for tracking. As technology progressed and warfare
demands increase, there has been a increased demand for a radar system which is
capable of tracking targets in urban environments. Unfortunately, due to multiple
and inconsistent returns from multiple objects in the complex environments, most
radar systems fail when operated in urban terrain [4]. This problem becomes even
worse in urban areas such as cities, where the large number of man-made structures

such as buildings cause undesirable signal returns.

Recently, research in underwater communications has increased due to new technologies such as unmanned underwater vehicles and underwater sensor networks. Underwater communications are challenging as the underwater acoustic (UWA) channel is highly time-varying, resulting in undesired signal distortions. Due to the slow speed of sound in underwater environments, the UWA channel exhibits wideband properties, resulting in time delay and Doppler scale signal distortions. In order to design a successful UWA communication system, it is important to have both accurate channel estimation algorithms as well as transmitted signals to match the UWA channel.

1.2 Urban Environment and Target Tracking

When tracking a target in an urban environment, the main challenges include, obscuration and shadowing, dense clutter, multipath reflections, and mutiple measurements originating from the same target. These challenges become even more problematic when there is time-varying number of targets present.

With regard to obscuration and shadowing, the most common solutions are either to employ airborne radar systems with very steep grazing angles or to deploy more sensors at different views. Dense clutter has been well-studied and various methods have been proposed to mitigate or eliminate clutter including estimation techniques [5–7] and adaptive waveform design methods [8–10].

Traditionally, when clutter is present, the measurement-to-track association methods are implemented to eliminate false measurements [2]. Multiple hypothesis tracking (MHT) is an algorithm for tracking multiple target in clutter [2]. MHT first performs measurement-to-track association on a sequence of measurements, and then it filters each data association hypothesis. However, as the MHT is an exhaustive approach, it is computationally expensive [2, 11, 12]. As an alternative, the joint

probabilistic data association (JPDA) method estimates the states by summing all the association hypothesis weighted by likelihood probabilities [13, 14]. Specifically, JPDA considers associations that survive after validation and combines those associations according to their likelihood. The JPDA is computationally less intensive [2, 15], however it requires that the number of targets is known and its performance decreases when the targets are close to each other [11, 16].

When the number of targets is time-varying, due to new targets entering the field-of-view (FOV), and existing targets leaving the FOV, the aforementioned MHT and JPDA approaches fail to work. An alternative solution to the multi-target tracking problem is to view the set of observations collectively, and try to estimate the set of target states directly, when the correct measurement-to-track association is unobservable [17]. The disadvantage of this approach is that the continuity of the individual target tracks are not maintained. One such method for multi-target tracking uses random finite set theory [18], in an approach analogous to the recursion used in Bayesian filtering by constructing multiple target posterior distributions. However, the time required for calculating joint multi-target likelihood probability density functions grows exponentially with the number of targets, therefore for sequential target estimation, this method is not practical for real time implementation.

A practical alternative to Bayesian multiple target tracking is the probability hypothesis density (PHD) filter that propagates first-order statistical moments [19] In [20–22], the PHD filter has been used to solve the traffic flow estimation and control problem. However, it has not been considered for tracking multiple targets in urban environments.

Another challenging problem with urban environments is the presence of multipath due to reflections from surrounding structures. Traditionally, measurements from multipath have been considered as interference, and previous solutions were pri-

marily focused on mitigating the effects of multipath [23–27]. Recently, the research focus has shifted from multipath mitigation to studying multipath returns for gaining additional target information. In [28, 29], it has been shown that when processed properly, multipath signal returns can provide auxiliary information about the target, which was previously unattainable with LOS returns only. By utilizing prior knowledge about the environment, such as road maps and building locations, multipath signal returns can be exploited to improve target detection obtained from LOS measurements [30]. Additionally, multipath exploitation allows the detection and tracking of targets without LOS, thereby decreasing the obscuration effects of the buildings and increasing the visible area of the environment [29]. This advantage subsequently allows airborne radar systems to better observe the urban environments with lower grazing angles and fewer platforms, presenting less expensive solution. Finally, by studying the reflectivity characteristics of the environment, the adversal effects of clutter can be reduced to increase detection and tracking performance [8]. In [1], particle filtering was combined with measurement-to-track association and waveform design to track a single target in clutter in an urban environment.

One of the most challenging problems for tracking multiple targets in urban environments is that each target can generate a time-varying number of signal returns/measurements. For example, a target can produce LOS signal return as well as multipath signal returns. In order to successfully track the targets, the signal returns must be associated to their corresponding signal paths. In [1], it is assumed that this association can be performed for one target by comparing the return signal strengths and time delays to the transmitted signal. However, for multiple targets, this association process can be computationally expensive and sometimes infeasible.

1.3   Underwater Acoustic Environments and Wireless Communications

Multi-user underwater acoustic (UWA) communications is difficult due to the wideband nature of the UWA channel. As a result, schemes for multiple access, channel modeling, and receiver design present more challenging problems. Traditional multiple access methods do not provide adequate signaling for multiple users in UWA channels. Such schemes include frequency-division multiple access (FDMA), time-division multiple access (TDMA), code-division multiple access (CDMA), and space-division multiple access (SDMA) [31]. For FDMA, the system signaling dimensions are divided along the frequency axis into non-overlapping channels, and each user is assigned a different frequency channel. For TDMA, the system signaling dimensions are divided along the time axis into non-overlapping channels, and each user is assigned a different time slot. For CDMA, the information signals of different users are modulated by orthogonal or non-orthogonal spreading codes. For SDMA, different spatial locations are assigned to different uses. Orthogonal frequency-division multiplex (OFDM) is a special case of FDMA, where each user is assigned an overlapping but orthogonal channel [32]. Existing UWA communication schemes do not fully exploit the potential of matching signaling schemes to discrete time-scale models of the wideband UWA environment. OFDM has been extensively used in UWA communication schemes, but coupled with appropriate post-processing as it is not robust to Doppler scaling effects [33, 34]. In [33], the distorted OFDM due to Doppler scaling is compensated at the receiver using resampling and then any remaining Doppler is removed using intercarrier interference reduction techniques. In [34], a multiple resampling OFDM receiver front-end is designed to have each resampling branch deal with each path with a different Doppler scaling factor. CDMA techniques have been widely used for multi-user UWA communications [35, 36]. Adaptive multi-user de-

tection techniques are applied in [35] instead of assuming an UWA channel model with multiple Doppler scaling paths at the receiver. In [37], a spread spectrum hyperbolic frequency modulation scheme is used that potentially matches the UWA communication channel. However, the assumed model uses only a single Doppler scale path and the multiple time delay paths can distort any possible scale diversity as no conditions are provided on the signal. A nonlinear frequency modulated (NFM) signaling scheme is developed in [38] by deriving constraints on the nonlinear phase function of the transmit signal to achieve orthogonality; the scheme, combined with frequency-hopping CDMA, is used in a multi-user communications scheme in [38, 39]. In [40], chirp modulation, with a zero cross-correlation condition, is combined with CDMA for frequency-nonselective and frequency-selective fading channels. Similar chirp modulation is applied to an ultra-wideband scheme in [41] and a multiple-input multiple-output multi-user scheme in [42]. Note, however, that signaling schemes that are matched to the wideband UWA channel have not yet been designed for multiple communications users. Such schemes are necessary since the demand for UWA communications has been increasing due to new underwater based applications [43, 44].

The highly time-varying nature of the wideband underwater environment can cause undesirable distortions to propagating acoustic signals [45–47]. Depending on the depth, communication frequency, and communication range, the UWA channel can be characterized by different model types such as wideband or dispersive [45–50]. In general, the dispersive channel model is used for shallow water and low frequency communications, whereas the wideband channel model is used for deep water and medium to high frequency communications [45–50]. In particular, UWA communication signals, with 0.3 to 20 kHz spectral components whose bandwidths are comparable to their central frequencies, have wideband properties due to the

fast movement of scatterers in the UWA channel, and the resulting signal distortions are multipath and Doppler scale changes. A discrete time-scale canonical model was proposed to represent the wideband channel received signal as the linear superposition of discrete time shifts and Doppler scalings of the transmitted signal, weighted by the wideband spreading function (WSF) coefficients [48]. The existing wideband UWA channel estimation algorithms assume that the channel support, i.e., Doppler scale spread and time delay spread. In [47], two algorithms including direct least square algorithm which assumes the knowledge of the channel support and MPD algorithm which creates a large dictionary, have shown the success of estimating the real UWA channel, however, the performance of how close the estimated channel coefficients compared to the true channel coefficients is not analyzed.

1.4 Thesis Contributions

Although many advances have been made in the areas of urban tracking and underwater communications, an important problem that still remains is one involving detection and estimation of multiple objects/users. Toward this end, we developed new algorithms for tracking multiple targets in the urban environment and detecting multiple users in underwater communications, as summarized next.

1.4.1 Multi-Target Tracking in Urban Environments

Our contributions in urban terrain multi-target tracking are summarized as follows.

- We proposed a new method for tracking multiple targets in urban environments by modifying the PHD filter to include measurement-to-multipath association (MMA). MMA uses the dominant path likelihood probability instead of the joint likelihood probability from all possible paths. Due to the presence of mul-

8

tipath, each target may generate more than one measurement, while traditional target tracking algorithms usually assume one target can generate at most one measurement at each time step. There are two types of data associations, one is measurement-to-track association, which associates the measurement to its corresponding target or clutter, the other is path-to-measurement association, which associates the measurement to its corresponding path (LOS or multipath reflection). It has been shown that data association methods are computationally expensive, and the computational complexity grows exponentially with the number of targets as well as the number of paths generated by them [2, 11, 12]. The PHD filter, implemented using particle filtering, is used to overcome the measurement-to-track association as well as allow for highly nonlinear measurement models, and the MMA approach resolves the problem of path-to-measurement associations.

- An adaptive clustering algorithm is proposed to iteratively estimate both the time-varying number of targets in the FOV as well as their corresponding state parameters.

1.4.2 Multi-user Underwater Acoustic Communications

Our contributions in multi-user underwater communications are summarized as follows.

- We proposed a wideband UWA channel estimation algorithm, which can estimate the channel support as well as the WSF coefficients. Unlike traditional wideband UWA channel estimation algorithms, this method integrates a direct least-squares approach with MPD time-frequency feature extraction and Dirichlet process Gaussian mixture modeling (DP-GMM). The use of DP-GMM al-

lows the estimation the wideband channel support. Initially, the MPD method is used to extract the channel features including Doppler scales, time shifts and WSF coefficients. Then the features are clustered using the DP-GMM algorithm, which clusters and estimates the number of Doppler scale paths as well as the Doppler scale values. The algorithm has two stages. During the first stage, the MPD is integrated with the direct least-squares approach to provide an initial estimate for the Doppler scale values. The DP-GMM is used during the second stage. The two-stage process is repeated to remove any Doppler scale paths with very small corresponding coefficients using thresholding process to estimate the channel Doppler support and WSF coefficients. Numerical simulations demonstrate the improved channel estimation performance of the proposed algorithm when compared to MPD and direct least-squares.

- We proposed a single-user communications signaling scheme for wideband UWA channels using hyperbolic frequency modulated (HFM) signals. The signal design exploits a time-scale canonical representation for wideband time-varying channels. Using signals with hyperbolic time-frequency signatures results in matching the underwater acoustic environment to achieve scale diversity since HFMs can be shown to be scale invariant. Note that signals with nonlinear time-frequency signatures such as hyperbolic have been shown to match the time-frequency characteristics of cetacean mammal sounds.

- We have extended the HFM signaling scheme for multiple user UWA communications by combining it with CDMA to improve multiuser detection performance. For this scheme, the transmitted symbols are represented by HFM signals with uniquely designed frequency-modulation (FM) rate parameters, and each user is distinguished by a unique pseudo random noise (PN) code.

10

- We proposed a new multi-user UWA communications scheme by designing the FM rate of the HFM signals. By imposing constrains on the FM rate, we demonstrate that we can minimize the correlation between two HFM signals in an UWA channel. Based on these constrains, we assign each symbol of each user a unique FM rate which forces the HFM signals to become orthogonal; an additional constraint ensures that the interference between users due to different time-scale paths is minimized. Numerical simulations demonstrate the improved bit error rate (BER) performance of the proposed scheme when compared to CDMA.

1.5   Thesis Organization

The thesis is organized as follows. In Chapter 2, we provide a brief introduction on state space modeling, and Bayesian inference methods such as the Kalman filter and particle filter. In Chapter 3, we provides an overview on existing representations of narrowband and wideband complex environments. We propose a modified PHD filter algorithm with multipath-to-measurement association for multi-target tracking in urban environments in Chapter 4. Specifically, we first provide the state space model for tracking multiple targets in urban terrain with clutter and multiple kinematic models. We then persent the proposed tracking method together with an adaptive clustering algorithm. Finally, we demonstrate the improved tracking performance of the new approach in a test urban environment based on the optimal subpattern assignment (OSPA) metric [51]. In Chapter 5, we propose a new estimation approach for wideband UWA channels based on integrating adaptive learning methods with time-frequency techniques. We discuss previously proposed methods for wideband channel estimation, including a conventional direct least-squared algorithm and the matching pursuit decomposition (MPD) time-frequency based method. We also

provide simulation results to compare the improved estimation performance of our method for estimating both the wideband channel support as well as the wideband channel coefficients. In Chapter 6, we propose the HFM signaling scheme for both single and multiple users. We first demonstrate the achieved scale diversity using HFM signaling for single user communications, and then we extend it for multi-user UWA communications by deriving constrains on the HFM rates. Finally, we demonstrate the improved BER performance of the HFM signaling schemes and compare them to traditional schemes currently used for UWA communications.

Chapter 2

STATE SPACE FORMULATION AND BAYESIAN APPROACH

2.1   Dynamic System

In order to analyze a dynamic system and estimate its time-varying state parameters, a state space representation of the system is required that is characterized by two models. The first model describes the evolution of the state with time (system model) and the second model relates the noisy measurements to the state (measurement model). As these are probabilistic models that can be used to update system information on receipt of new measurements, they are ideally suited to Bayesian inference approaches [3].

The Bayesian approach to dynamic state estimation attempts to construct the posterior probability density function (pdf) of the state based on all available received measurements. This pdf can be used to obtain an estimate of the state. A measure of the accuracy of the estimate can also be obtained. As the state is dynamically varying, its estimate is required every time a measurement is received. This can be achieved using a Bayesian recursive filter. A recursive filtering approach processes received data sequentially rather than as a batch and as a result, data does not need to be stored or reprocessed when a new measurement becomes available. Such a filter consists of essentially two stages: prediction and update. The prediction stage uses the system model to predict the state at the current time step given the state at the previous time step. The current state is also affected by an additive random process that models possible errors in the state model. During the update stage, the latest measurement is used to modify the prediction pdf. This is achieved using Bayes

theorem, which is the mechanism for updating knowledge about the target state when new information is available from new data.

2.2   State Space Model

Using the state model, the target state vector $\mathbf{x}_k$ at time step k can be written as

$$\mathbf{x}_k = \mathbf{f}_k(\mathbf{x}_{k-1}, \mathbf{w}_{k-1}), \tag{2.1}$$

where $\mathbf{f}_k$ is the target state function which models the state evolution, and $\mathbf{w}_{k-1}$ is the random process that represents possible errors in the model and is usually assumed to be Gaussian.

Given the measurement vector $\mathbf{z}_k$, the measurement model can be written as

$$\mathbf{z}_k = \mathbf{h}_k(\mathbf{x}_k, \mathbf{v}_k), \tag{2.2}$$

where $\mathbf{h}_k$ is the measurement function that models the relationship between the measurement and the current target state, and $\mathbf{v}_k$ is the measurement noise.

2.3   Bayesian Inference Approach

The Bayesian inference approach assumes that the target tracking process can be fully characterized by the posterior pdf. Specifically, if the posterior pdf from the previous time step $k-1$ is $p(\mathbf{x}_{k-1}|\mathbf{z}_{k-1})$, the predicted pdf can be calculated using the Chapman-Kolmogorov equation as [3]

$$p(\mathbf{x}_k|\mathbf{z}_{k-1}) = \int p(\mathbf{x}_k|\mathbf{x}_{k-1})p(\mathbf{x}_{k-1}|\mathbf{z}_{k-1}) \, d\mathbf{x}_{k-1}, \tag{2.3}$$

where $p(\mathbf{x}_k|\mathbf{x}_{k-1})$ is the prior pdf obtained from the state equation. Using the predicted pdf, the updated posterior pdf $p(\mathbf{x}_k|\mathbf{z}_k)$ at time step k, can be calculated using Bayes' rule as

$$p(\mathbf{x}_k|\mathbf{z}_k) = \frac{p(\mathbf{z}_k|\mathbf{x}_k)p(\mathbf{x}_k|\mathbf{z}_{k-1})}{p(\mathbf{z}_k)}, \tag{2.4}$$

where $p(\mathbf{z}_k|\mathbf{x}_k)$ is the likelihood function obtained from the measurement equation. Note that, it is assumed that all processes are Markov processes of order one, i.e., current state only depends on the previous state.

The recurrence relation in Equations (2.3) and (2.4) form the basis for the optimal Bayesian solution for estimation the state as $\hat{\mathbf{x}}_k = E[\mathbf{x}_k|\mathbf{z}_k] = \int p(\mathbf{x}_k|\mathbf{z}_k)d\mathbf{x}_k$, where $E[\cdots]$ denotes statistical expectation.

2.3.1   Kalman Filter

The Kalman filter provides a recursive optimal solution to the state space estimation problem under certain conditions. These conditions confine the model error process and the measurement noise to be Gaussian, and the dynamic state model and measurement model to be linear [3].

Using linear models, the state space model can be rewritten as

$$\mathbf{x}_k = \mathbf{F}_k\mathbf{x}_{k-1} + \mathbf{w}_{k-1}, \tag{2.5}$$

$$\mathbf{z}_k = \mathbf{H}_k\mathbf{x}_k + \mathbf{v}_k, \tag{2.6}$$

where $\mathbf{F}_k$ and $\mathbf{H}_k$ are known linear matrices, and $\mathbf{w}_k$ and $\mathbf{v}_k$ are zero-mean Gaussian random processes with covariance matrices Q_{k-1} and R_k, respectively. The solution of the Kalman filter is given by

$$p(\mathbf{x}_{k-1}|\mathbf{z}_{k-1}) = \mathcal{N}(\mathbf{x}_{k-1}; \mathbf{m}_{k-1|k-1}, \mathbf{P}_{k-1|k-1}) \tag{2.7}$$

$$p(\mathbf{x}_k|\mathbf{z}_{k-1}) = \mathcal{N}(\mathbf{x}_k; \mathbf{m}_{k|k-1}, \mathbf{P}_{k|k-1}) \tag{2.8}$$

$$p(\mathbf{x}_k|\mathbf{z}_k) = \mathcal{N}(\mathbf{x}_k; \mathbf{m}_{k|k}, \mathbf{P}_{k|k}), \tag{2.9}$$

where

$$\mathbf{m}_{k|k-1} = \mathbf{F}_k \, \mathbf{m}_{k-1|k-1} \tag{2.10}$$

$$\mathbf{P}_{k|k-1} = Q_{k-1} + \mathbf{F}_k \, \mathbf{P}_{k-1|k-1} \, \mathbf{F}_k^T \tag{2.11}$$

$$\mathbf{m}_{k|k} = \mathbf{m}_{k|k-1} + \mathbf{K}_k(\mathbf{z}_k - \mathbf{H}_k \, \mathbf{m}_{k|k-1}) \tag{2.12}$$

$$\mathbf{P}_{k|k} = \mathbf{P}_{k|k-1} - \mathbf{K}_k \, \mathbf{H}_k \, \mathbf{P}_{k|k-1}. \tag{2.13}$$

and $\mathcal{N}(\mathbf{x}; \mathbf{m}, \mathbf{P})$ states that the random vector $\mathbf{x}$ has a Gaussian distribution with mean $\mathbf{m}$ and the covariance matrix $\mathbf{P}$. The Kalman gain can be calculated as

$$\mathbf{S}_k = \mathbf{H}_k \, \mathbf{P}_{k|k-1} \, \mathbf{H}_k^T + R_k, \tag{2.14}$$

where

$$\mathbf{K}_k = \mathbf{P}_{k|k-1} \, \mathbf{H}_k^T \, \mathbf{S}_k^{-1}. \tag{2.15}$$

2.3.2 Particle Filter

The particle filter (PF) provides an alternative solution to the state space estimation problem when the random processes are non-Gaussian and/or the dynamic state model and measurement model are nonlinear [3]. At each time step, the PF approximates the posterior pdf by a weighted set of particles, and at the end of every recursion, the target state can be estimated based on the particles and their corresponding weights.

During the prediction step at time step k, the PF assumes that the posterior pdf $p(\mathbf{x}_{k-1}|\mathbf{z}_{k-1})$ from the previous time step $k-1$ can be approximated using N_s particles $\mathbf{x}_{k-1}^{(i)}$ and associated normalized weights $w_{k-1}^{(i)}$, $i = 1, 2, \ldots, N_s$ as

$$p(\mathbf{x}_{k-1}|\mathbf{z}_{k-1}) \approx \sum_{i=1}^{N_s} w_{k-1}^{(i)} \, \delta(\mathbf{x}_{k-1} - \mathbf{x}_{k-1}^{(i)}), \tag{2.16}$$

then the predicted pdf can be approximated as

$$p(\mathbf{x}_k|\mathbf{z}_{k-1}) \approx \sum_{i=1}^{N_s} w_{k|k-1}^{(i)} \delta(\mathbf{x}_k - \mathbf{x}_k^{(i)}), \tag{2.17}$$

where the particles are obtained from the importance density $q(\cdot|\mathbf{x}_{k-1}^{(i)}, \mathbf{z}_k)$ as

$$\mathbf{x}_k^{(i)} \sim q(\mathbf{x}_k|\mathbf{x}_{k-1}^{(i)}, \mathbf{z}_k), \tag{2.18}$$

and the particle weights remain the same

$$w_{k|k-1}^{(i)} = w_{k-1}^{i}. \tag{2.19}$$

During the update step, based on the received measurements $\mathbf{z}_k$, the particle weights are updated using

$$w_k^{(i)} = w_{k|k-1}^{(i)} \frac{p(\mathbf{z}_k|\mathbf{x}_k^{(i)}) \, p(\mathbf{x}_k^{(i)}|\mathbf{x}_{k-1}^{(i)})}{q(\mathbf{x}_k|\mathbf{x}_{k-1}^{(i)}, \mathbf{z}_k)}, \tag{2.20}$$

and the posterior pdf at time step k can be approximated as

$$p(\mathbf{x}_k|\mathbf{z}_k) \approx \sum_{i=1}^{N_s} w_k^{(i)} \delta(\mathbf{x}_k - \mathbf{x}_k^{(i)}). \tag{2.21}$$

It can be shown that as the number of particles approach infinity, the approximation approaches the true posterior pdf. Note that the importance density is normally selected to be the prior pdf, that is, $q(\mathbf{x}_k^{(i)}|\mathbf{x}_{k-1}^{(i)}, \mathbf{z}_k) = p(\mathbf{x}_k^{(i)}|\mathbf{x}_{k-1}^{(i)})$ [3].

A common problem with the PF is the degeneracy phenomenon, where after a few iterations, all but a few particles have negligible weight. In order to solve the degeneracy problem, the resampling process is implemented after every update step as summarized in Table 1.

The overall PF algorithm is summarized in Table 2.

$$[\{\mathbf{x}_k^{(j)}, w_k^{(j)}\}_{j=1}^{N_s}] = \text{RESAMPLE}\,[\{\mathbf{x}_k^{(i)}, w_k^{(i)}\}_{i=1}^{N_s}]$$

Initialize the cumulate density function (CDF): $c_1 = 0$

FOR $i = 2 : N_s$

      Construct CDF: $c_i = c_{i-1} + w_k^{(i)}$

END FOR

Let index u_1 be the uniformly distributed between 0 and $1/N_s$

FOR $j = 1 : N_s$

      $u_j = u_1 + (j-1)/N_s$

      WHILE $u_j > c_i$

          $i > i + 1$

      END WHILE

      Assign particle: $\mathbf{x}_k^{(j)} = \mathbf{x}_k^{(i)}$

      Assign weight: $w_k^{(j)} = 1/N_s$

END FOR

Table 1: Particle Filtering Resampling Algorithm.

$$[\{\mathbf{x}_k^{(i)}, w_k^{(i)}\}_{j=1}^{N_s}] = \text{PF}\,[\{\mathbf{x}_{k-1}^{(i)}, w_{k-1}^{(i)}\}_{i=1}^{N_s}, \mathbf{z}_k]$$

FOR $i = 1 : N_s$

      Draw $\mathbf{x}_k^{(i)} \sim q(\mathbf{x}_k | \mathbf{x}_{k-1}^{(i)}, \mathbf{z}_k)$

      Assign particle weights $w_{k|k-1}^{(i)} = w_{k-1}^{(i)}$

      $w_k^{(i)} = w_{k|k-1}^{(i)} \dfrac{p(\mathbf{z}_k | \mathbf{x}_k^{(i)})\, p(\mathbf{x}_k^{(i)} | \mathbf{x}_{k-1}^{(i)})}{q(\mathbf{x}_k | \mathbf{x}_{k-1}^{(i)}, \mathbf{z}_k)}$

END FOR

Calculate total weight: $w = \sum_{i=1}^{N_s} w_k^{(i)}$

FOR $i = 1 : N_s$

      Normalize $w_k^{(i)} = w_k^{(i)}/w$

END FOR

Resample using the algorithm in Table 1

$$[\{\mathbf{x}_k^{(j)}, w_k^{(j)}\}_{j=1}^{N_s}] = \text{RESAMPLE}\,[\{\mathbf{x}_k^{(i)}, w_k^{(i)}\}_{i=1}^{N_s}]$$

Table 2: Particle Filtering Algorithm.

Chapter 3

LINEAR TIME-VARYING SYSTEM REPRESENTATIONS

Linear time-varying (LTV) system representations have been widely used to model systems or environments that are characterized by propagation, dispersive scattering and rapid time variations. The characterization of LTV systems has been studied in many areas such as the advent of troposcatter, inoscatter and moon communication links, radar astronomy systems [52–54], and underwater acoustic channels [55]. In order to represent an LTV system, two-dimensional (2-D) kernel functions which match the systems characteristics are used. For example, for a narrowband LTV system, the time-varying impulse response is used to characterize the system, which provides the effect of the system to an impulse signal. The narrowband LTV system can also be characterized by the narrowband spreading function (NSF) which is a measure of the spread of time and frequency shifts induced by a narrowband LTV system. The NSF provides an interpretation of the system output as a weighted superposition of time and frequency shifts on the input signal [52, 55]. In addition, the Weyl symbol is a time-frequency (TF) representation which is related to the spreading function via Fourier transformations, and it can be interpreted as the 2-D transfer function of a narrowband LTV system [56–59]. The narrowband LTV representations have been widely used for radar signal design [60], pulse shaping in multicarrier communications [61–63], and wireless channel modeling [64, 65]. In [66], the narrowband LTV model has been used to characterize fast fading wireless communication channels in terms of the multipath and Doppler distortion caused by the channel.

The narrowband LTV system model can successfully model the system when the signal has a small fractional bandwidth (ratio of signal bandwidth over carrier frequency), and every frequency component is shifted by a constant frequency. However, when the motion becomes fast and the signal has a large fractional bandwidth, the system causes Doppler scale changes to the signal(expansions or compressions in time), and the wideband LTV system model needs to be used. For a wideband system, each frequency is shifted by a varying amount due to Doppler scaling [67, 68]. The wideband system model has been widely used in applications such as underwater and airborne acoustics [69, 70], ultra wideband radar [71], synthetic aperture sonar [66] and ultrasonic biomedical imaging systems [72, 73].

In this chapter, we provide a review on the narrowband and wideband system characterization, focusing on system representation in term of corresponding spreading function characterizations.

3.1 Narrowband System Representations

For an LTV narrowband system $\mathcal{L}$ with an input signal $x(t)$, the output signal $(\mathcal{L}x)(t)$ is given by [74]

$$(\mathcal{L}x)(t) = \int_{-\infty}^{\infty} K_{\mathcal{L}}(t, \tau)x(\tau)d\tau, \tag{3.1}$$

where $K_{\mathcal{L}}(t, \tau)$ is the 2-D kernel function that uniquely characterizes the system $\mathcal{L}$. The narrowband spreading function (SF) is defined as the Fourier transform of the kernel $K_{\mathcal{L}}(t, \tau)$ in (3.1):

$$\mathrm{SF}_{\mathcal{L}}(\tau, \nu) = \int_{-\infty}^{\infty} K_{\mathcal{L}}(t + \frac{\tau}{2}, t - \frac{\tau}{2})e^{-j2\pi\nu t}dt. \tag{3.2}$$

The SF provides an attractive representation for a narrowband LTV system in terms of the effect of the system on the input signal [52, 55, 58, 75]. Specifically, the output of

20

a narrowband LTV system can be represented as the superposition of time-frequency shifted versions of the input signal $x(t)$, weighted by the SF, i.e.,

$$(\mathcal{L}x)(t) = \int_{-\infty}^{\infty} \int_{-\infty}^{\infty} \mathrm{SF}_{\mathcal{L}}(\tau, \nu) e^{-j\pi\tau\nu} (\mathcal{M}_{\nu}\mathcal{S}_{\tau}x) d\nu d\tau. \tag{3.3}$$

where $\mathcal{S}_{\tau}$ is the time shift operator defined as

$$(\mathcal{S}_{\tau}x)(t) = x(t - \tau), \tag{3.4}$$

and $\mathcal{M}_{\nu}$ is the frequency shift operator defined as

$$(\mathcal{M}_{\nu}x)(t) = x(t)e^{j2\pi\nu t}, \tag{3.5}$$

Combining the two operators as in Equation (3.3), we obtian

$$(\mathcal{M}_{\nu}\mathcal{S}_{\tau}x)(t) = x(t - \tau)e^{j2\pi\nu t} \tag{3.6}$$

3.2   Wideband System Representations

3.2.1   Wideband LTV System

For a wideband LTV system $\mathcal{B}$ with an input signal $x(t)$, the output $(\mathcal{B}x)(t)$ can be characterized by a superposition of time shifts and scale changes, weighted by the wideband spreading function (WSF),

$$(\mathcal{B}x)(t) = \int_{-\infty}^{\infty} \int_{-\infty}^{\infty} \mathrm{WSF}_{\mathcal{B}}(\tau, a)(\mathcal{S}_{\tau}\mathcal{C}_{a}x)(t) d\tau da. \tag{3.7}$$

where $\mathcal{S}_{\tau}$ is defined in Equation (3.4) and the scale change operator $\mathcal{C}_{a}$ is defined as

$$(\mathcal{C}_{a}x)(t) = \sqrt{|a|}x(at).$$

The combined waveform

$$(\mathcal{S}_{\tau}\mathcal{C}_{a}x)(t) = \sqrt{|a|}x(a(t - \tau)) \tag{3.8}$$

represents a wideband signal model that resulted from the transmitted signal $x(t)$ reflecting off fast moving point scatterers. Specifically, the time shift τ is the propagation delay, and the Doppler scaling $a = \frac{1+v/c}{1-v/c}$ provides information on the on the radial velocity component v of the scatterer, where c is the speed of propagation of the signal in the system.

Due to physical restrictions on the system such as velocity and path loss, we can assume that the WSF has a compact support in the correlative (τ, a) domain, i.e.,

$$\text{WSF}_{\mathcal{B}}(\tau, a) = 0, \quad \forall [\tau, a] \notin [0, T_d] \times [A_0, A_1]. \tag{3.9}$$

Here, T_d is the multipath delay spread and $A_d = A_1 - A_0$ is the Doppler scale spread. From the previous analysis, if the velocities in the system are continuously distributed in the range $v \in [v_0, v_1]$, then $A_0 \approx 1 - 2v_0/c$, $A_1 \approx 1 + 2v_1/c$, thus $A_d \approx 2(v_0 + v_1)/c$ can provide an intuitive measure of the rapidness of the motion present in the system.

3.2.2 Discrete Time-Scale System Representation

Mellin Transform The Mellin transform of a signal $x(t)$ defined as

$$\text{MT}_x(\beta) = \int_0^\infty \frac{1}{\sqrt{t}} x(t) e^{j2\pi\beta \ln \frac{t}{t_r}} dt, \tag{3.10}$$

where $\beta \in \mathbb{R}$ is the Mellin variable, and $t_r > 0$ is a normalization time constant (normally assumed to be 1. The inverse Mellin transform is defined as

$$x(t) = \int_{-\infty}^\infty \frac{1}{\sqrt{t}} \text{MT}_x(\beta) e^{-j2\pi\beta \ln \frac{t}{t_r}} d\beta, \quad t > 0 \tag{3.11}$$

As demonstrated next, the Mellin transform of the input signal to a wideband system provides information on the system's Doppler scale spread.

Sampling The Time-Scale Parameters   The output $y(t)$ of a wideband time-varying system, given an input signal $x(t)$, can be written as,

$$y(t) = \int_0^\infty \int_{-\infty}^\infty \chi(\tau, a) \sqrt{a}\, x(a(t - \tau))d\tau da, \qquad (3.12)$$

where $\chi(\tau, a)$ denotes the wideband spreading function (WSF). We assume that the transmitted signal $x(t)$ has its Fourier transform $X(f)$ bounded within $f \in [-W/2, W/2]$, and its Mellin transform $\mathrm{MT}_x(\beta)$ bounded within $\beta \in [-\beta_0/2, \beta_0/2]$. Based on these support assumptions, (3.12) can be re-written as the 2-D summation, [48]

$$y(t) = \sum_{m \in \mathbb{Z}} \sum_{n \in \mathbb{Z}} \hat{\chi}(\frac{n}{a_0^m W}, a_0^m)\, a_0^{\frac{m}{2}}\, x(a_0^m t - \frac{n}{W})), \qquad (3.13)$$

where $a_0 = e^{1/\beta_0}$ is the basic scaling factor, and and $\hat{\chi}(\frac{n}{a_0^m W}, a_0^m)$ is a 2-D smoothed version of the WSF $\chi(\tau, a)$, which can be calculated as,

$$\hat{\chi}(\tau, a) = \int_0^\infty \int_{-\infty}^\infty \chi(\tau', a')\mathrm{sinc}(aW(\tau - \tau'))\mathrm{sinc}\left(\frac{\ln a - \ln a'}{\ln a_0}\right) d\tau' da'. \qquad (3.14)$$

The steps for obtaining Equation (3.13) from Equation (3.12) are based on sampling the parameter τ and a in Equation (3.12). We first sample the scale parameter a using the Mellin transform. First note that we can rewrite Equation (3.12) as

$$
\begin{aligned}
y(t) &= \int_\tau \left[\int_a \theta^*(a; \tau)g(a(t - \tau)/t_r)da \right] d\tau \\
&= \int_\tau s(c; t, \tau)d\tau.
\end{aligned}
\qquad (3.15)
$$

where

$$\theta^*(a; \tau) = \chi^*(\tau, a)\sqrt{a} \qquad (3.16)$$

$$g(a) = x(at_r) \qquad (3.17)$$

$$s(c; t, \tau) = \int_a \theta^*(a; \tau) g(ac) da \qquad (3.18)$$

Using the multiplicative convolution property of the Mellin transform, it can be shown that

$$\text{MT}_s(\beta; \tau) = \text{MT}_\theta^*(\beta; \tau) \text{MT}_g(\beta) \qquad (3.19)$$

Using the inverse Mellin transform of $s(c; t, \tau)$ and Equation (3.19), we can express

$$
\begin{aligned}
s(c; t, \tau) &= \int \sqrt{1} c \text{MT}_s(\beta; \tau) \exp(-j2\pi\beta \ln(c)) d\beta \\
&= \int \frac{1}{c} \text{MT}_\theta^*(\beta; \tau) \text{MT}_g(\beta) \exp(-j2\pi\beta \ln(c)) d\beta
\end{aligned} \qquad (3.20)
$$

Replacing Equation (3.20) in (3.15), we obtain

$$
\begin{aligned}
y(t) &= \int_\tau s(c; t, \tau) d\tau \\
&= \int_\tau \int_\beta \sqrt{1}(t - \tau)/t_r \text{MT}_\theta^*(\beta; \tau) \text{MT}_g(\beta) \exp(-j2\pi\beta \ln(t - \tau/t_r)) d\beta
\end{aligned} \qquad (3.21)
$$

If we let the Mellin support of $g(a)$ to be within $\beta \in (-\beta_0/2, \beta_0/2)$, then we can replace $\text{MT}_g(\beta)$ in Equation (3.21) with

$$\text{MT}_g(\beta) = P_{\beta_0}(\beta) \text{MT}_g(\beta) \qquad (3.22)$$

where $P_{\beta_0}(\beta)$ is a rectangular window whose value is 1 for $-\beta_0/2 \leq \beta \leq \beta_0/2$ and zero otherwise. Replacing (3.22) in (3.21), we obtain

$$y(t) = \int_\tau \int_\beta \sqrt{1}(t - \tau)/t_r \text{MT}_\theta^*(\beta; \tau) P_{\beta_0}(\beta) \text{MT}_g(\beta) \exp(-j2\pi\beta \ln(t - \tau/t_r)) d\beta \qquad (3.23)$$

Considering $\text{MT}_\theta^*(\beta; \tau) P_{\beta_0}(\beta)$ in (3.23), we can express its Fourier series to obtain

$$\text{MT}_\theta^*(\beta; \tau) P_{\beta_0}(\beta) = (1/\beta_0) \sum_m a_m(\tau) e^(- j2\pi(m/\beta_0)\beta) \qquad (3.24)$$

Using the inverse Fourier series of (3.24), we can obtain

$$
\begin{aligned}
a_m(\tau) &= \int \text{MT}_\theta^*(\beta; \tau) P_{beta_0}(\beta) e^(j2\pi(m/\beta_0)\beta) d\beta \\
&= \int_{-\beta_0/2}^{\beta_0/2} \text{MT}_\theta^*(\beta; \tau) e^(j2\pi(m/\beta_0)\beta) d\beta
\end{aligned} \qquad (3.25)
$$

We let $1/\beta_0 = \ln(a_0)$ and replace the MT of $\text{MT}_\theta^*(\beta; \tau)$ in (3.25) to obtain

$$
\begin{aligned}
\alpha_m(\tau) &= \int_0^\infty \chi^*(\tau, a') \left[\int_{-\frac{1}{2\ln a_0}}^{\frac{1}{2\ln a_0}} e^{-j2\pi\beta' \ln a'} e^{j2\pi m \ln a_0 \beta'} d\beta' \right] da' \\
&= \int_{A_0}^{A_1} \chi^*(\tau, a') \frac{1}{\ln a_0} \operatorname{sinc}(m - \frac{\ln a'}{\ln a_0}) da'.
\end{aligned}
\tag{3.26}
$$

Substituting Equation (3.26) and Equation (3.24) into Equation (3.23), we can rewrite Equation (3.23) as

$$
\begin{aligned}
y(t) &= \int_0^\infty \int_{-\infty}^\infty \sum_{m \in \mathbb{Z}} \chi(\tau, a') \operatorname{sinc}\left(m - \frac{\ln a'}{\ln a_0} \right) \cdot \\
&\qquad \left(\int_{-\infty}^\infty \text{MT}_x(\beta) e^{-j2\pi\beta \ln \frac{a_0^m(t-\tau)}{t_r}} \frac{d\beta}{\sqrt{t - \tau}} \right) d\tau \, da' \\
&= \sum_{m \in \mathbb{Z}} \int_{-\infty}^\infty \left(\int_0^\infty \chi(\tau, a') \operatorname{sinc}\left(m - \frac{\ln a'}{\ln a_0} \right) da' \right) a_0^{\frac{m}{2}} x(a_0^m(t - \tau)) d\tau.
\end{aligned}
\tag{3.27}
$$

If we define the scale-smoothed version of $\chi(\tau, a)$ as,

$$
\tilde{\chi}(\tau, a) = \int_0^\infty \chi(\tau, a') \operatorname{sinc}\left(\frac{\ln a - \ln a'}{\ln a_0} \right) da',
\tag{3.28}
$$

then (3.27) can be re-written as

$$
y(t) = \sum_{m \in \mathbb{Z}} \int_{-\infty}^\infty \tilde{\chi}(\tau, a_0^m) \, a_0^{\frac{m}{2}} \, x(a_0^m(t - \tau)) d\tau.
\tag{3.29}
$$

Note that the scale parameter in (3.12) is geometrically sampled as $a = a_0^m$, where a_0 is the basic scaling factor, and m is an integer.

Next, we demonstrate the sampling of the time delay parameter using the Fourier transform (FT). We assume that the FT of $\tilde{\chi}(\tau, a)$ and $x(\tau)$ (with respect to τ) are represented by $\tilde{U}(f; a)$ and $X(f)$, respectively. From the inverse Fourier transform property of the frequency multiplication, Equation (3.29) can be re-written as

$$
y(t) = \sum_{m \in \mathbb{Z}} \int_{-\infty}^\infty \tilde{U}(f; a_0^m) \, a_0^{-\frac{m}{2}} \, X(a_0^{-m} f) \, e^{j2\pi ft} df.
\tag{3.30}
$$

25

We also assume that $X(f)$ is bandlimited to $[-\frac{W}{2}, \frac{W}{2}]$. Then $a_0^{-\frac{m}{2}} X(a_0^{-m}f)$ is ban-dlimited to $[-\frac{a_0^m W}{2}, \frac{a_0^m W}{2}]$. Thus, $a_0^{-\frac{m}{2}} X(a_0^{-m}f)$ can be replaced by

$P_{a_0^m W}(f)\, a_0^{-\frac{m}{2}} X(a_0^{-m}f)$, where $P_{f_0}(f) = 1$ for $-\frac{f_0}{2} \le f \le \frac{f_0}{2}$, and zero otherwise.

Then, we have

$$\tilde{U}(f; a_0^m)\, P_{a_0^m W}(f) \;=\; \frac{1}{a_0^m W} \sum_{n\in\mathbb{Z}} \gamma_n(a_0^m)\, e^{-j2\pi \frac{nf}{a_0^m W}}, \tag{3.31}$$

where the Fourier coefficient $\gamma_n(a_0^m)$ for a fixed m can be calculated as

$$
\begin{aligned}
\gamma_n(a_0^m) &= \int_{-\infty}^{\infty} \tilde{U}(f; a_0^m)\, P_{a_0^m W}(f)\, e^{j2\pi \frac{n}{a_0^m W} f}\, df \\
&= \int_{-\frac{a_0^m W}{2}}^{\frac{a_0^m W}{2}} \left(\int_{-\infty}^{\infty} \tilde{\chi}(\tau', a_0^m)\, e^{-j2\pi \tau' f}\, d\tau' \right) e^{j2\pi \frac{n}{a_0^m W} f}\, df \\
&= \int_{-\infty}^{\infty} \tilde{\chi}(\tau', a_0^m) \int_{-\frac{a_0^m W}{2}}^{\frac{a_0^m W}{2}} e^{j2\pi f \frac{n}{a_0^m W} - \tau'}\, df\, d\tau' \\
&= a_0^m W \int_{-\infty}^{\infty} \tilde{\chi}(\tau', a_0^m)\, sinc(n - a_0^m W\tau')\, d\tau'.
\end{aligned}
\tag{3.32}
$$

Substituting Equation (3.32) and Equation (3.31) into Equation (3.30), we have

$$
\begin{aligned}
y(t) &= \sum_{m\in\mathbb{Z}} \sum_{n\in\mathbb{Z}} \left(\int_{-\infty}^{\infty} \tilde{\chi}(\tau', a_0^m)\, \mathrm{sinc}(n - a_0^m W\tau')\, d\tau' \right) \cdot \\
&\qquad\qquad\qquad \left(\int_{-\infty}^{\infty} a_0^{-\frac{m}{2}} X(a_0^{-m}f)\, e^{j2\pi f(t - \frac{n}{a_0^m W})}\, df \right) \\
&= \sum_{m\in\mathbb{Z}} \sum_{n\in\mathbb{Z}} \left(\int_{-\infty}^{\infty} \int_{-\infty}^{\infty} \tilde{\chi}(\tau', a')\, \mathrm{sinc}\left(m - \frac{\ln a'}{\ln a_0} \right) \mathrm{sinc}(n - a_0^m W\tau')\, d\tau'\, da' \right) \cdot \\
&\qquad\qquad\qquad a_0^{-\frac{m}{2}}\, x(a_0^m t - \frac{n}{W}).
\end{aligned}
\tag{3.33}
$$

It can be observed that for a fixed m, the time delay parameter is uniformly sampled as $\tau = n/(a_0^m W)$, where n is an integer. The time-smoothed version of $\tilde{\chi}(\tau, a_0^m)$ can be thus written as

$$\hat{\chi}(\tau, a_0^m) \;=\; \int_{-\infty}^{\infty} \tilde{\chi}(\tau', a_0^m)\, \mathrm{sinc}(a_0^m W(\tau - \tau'))\, d\tau'. \tag{3.34}$$

26

Finite Approximation If the WSF $\chi(\tau, a)$ is nonzero for $A_0 \leq a \leq A_1$, and $0 < \tau < T_d$, then (3.12) can be written as

$$y(t) = \int_{A_0}^{A_1} \int_0^{T_d} \chi(\tau, a) \sqrt{a}\, x(a(t - \tau))d\tau da. \tag{3.35}$$

Moreover, the infinite summation in (3.13) can be approximated as

$$y(t) \approx \sum_{m=M_0}^{M_1} \sum_{n=0}^{N(m)} \hat{\chi}(\frac{n}{a_0^m W}, a_0^m)\, a_0^{\frac{m}{2}}\, x(a_0^m t - \frac{n}{W}), \tag{3.36}$$

where the summation limits are determined as $M_0 = \lfloor \ln A_0 \ln a_0 \rfloor$, $M_1 = \lceil \ln A_1 \ln a_0 \rceil$, and $N(m) = \lceil a_0^m W T_d \rceil$, where $\lfloor \cdot \rfloor$ denotes the floor and $\lceil \cdot \rceil$ denotes the ceil.

Since $A_0 \leq a \leq A_1$, then (3.28) can be re-written as

$$\tilde{\chi}(\tau, a_0^m) = \int_{\ln A_0}^{\ln A_1} \chi(\tau, e^\gamma) \operatorname{sinc}\left(\frac{m \ln a_0 - \gamma}{\ln a_0} \right) e^\gamma d\gamma. \tag{3.37}$$

where the mth coefficient $\tilde{\chi}(\tau, a_0^m)$ is significantly nonzero only when $M_0 \leq m \leq M_1$, where $M_0 = \lfloor \ln A_0 / \ln a_0 \rfloor$ and $M_1 = \lceil \ln A_1 / \ln a_0 \rceil$.

Since $0 \leq \tau \leq T_d$, Equation (3.34) can be re-written as

$$\hat{\chi}(\frac{n}{a_0^m W}, a_0^m) = \int_0^{T_d} \tilde{\chi}(\tau', a_0^m) \operatorname{sinc}(n - a_0^m W \tau')d\tau' \tag{3.38}$$

where $0 \leq n \leq N(m)$, and $N(m) = \lceil a_0^m W T_d \rceil$.

Thus, the discrete version of Equation (3.35) can be written as [48]

$$y(t) \approx \sum_{m=M_0}^{M_1} \sum_{n=0}^{N(m)} \chi_{n,m}\, x_{n,m}(t), \tag{3.39}$$

where

$$\chi_{n,m} = \hat{\chi}(\frac{n}{a_0^m W}, a_0^m), \tag{3.40}$$

and $\chi_{n,m}(t)$ is a time-shifted and scaled version of $x(t)$, that is,

$$x_{n,m}(t) = a_0^{\frac{m}{2}}\, x(a_0^m t - \frac{n}{W}). \tag{3.41}$$

Chapter 4

MULTI-TARGET TRACKING IN URBAN TERRAIN

In this chapter, we propose a modified PHD filter for multiple target tracking that incorporates a multipath-to-measurement association (MMA) scheme to solve the problem of the multiple measurements due to the dense urban environment. When a measurement is received, it needs to be associated to a target (measurement-to-track association) as well as to a particular type of measurement such as LOS or a one-bounce reflection (multipath-to-measurement association). By using the PF-PHD and treating the measurements from all targets as an RFS, the measurement-to-track association problem is avoided. The proposed PF-PHD-MMA deals with the multipath-to-measurement association by calculating the path likelihood probability. We also incorporate clutter and multiple kinematic models [3], together with an adaptive k-means algorithm in order to estimate both the number of targets and their corresponding states.

This chapter is organized as follows. In Section 4.1, we provide the state space model for tracking multiple targets in urban terrain with clutter and multiple kinematic models. The proposed modified PF-PHD with multipath-to-measuremet association is described in Section 4.2. In Section 4.3, numerical simulation results are shown to demonstrate the improved tracking performance in a test bench urban environment based on the optimal subpattern assignment (OSPA) metric [51].

4.1 State Space Model for Urban Tracking

4.1.1 Target State Model

We consider the problem of tracking a time-varying number L_k of targets at time step k using an airborne radar. The state parameter vector of the lth target, $l = 1, \ldots, L_k$ is given by $\mathbf{x}_{k,l} = [x_{k,l} \ \dot{x}_{k,l} \ y_{k,l} \ \dot{y}_{k,l}]^{\mathrm{T}}$. Here, $(x_{k,l} \ y_{k,l})$ and $(\dot{x}_{k,l} \ \dot{y}_{k,l})$, are the target's two-dimensional (2-D) position and velocity Cartesian coordinates, respectively, and T denotes vector transpose. The kinematic state motion equation is given by

$$\mathbf{x}_{k,l} = \mathbf{F}\mathbf{x}_{k-1,l} + \mathbf{w}_{k-1}, \tag{4.1}$$

where matrix $\mathbf{F}$ provides the evolution of the target parameters over a duration of Δt seconds. The matrix changes depending on whether the target moves with constant velocity (CV) or maneuvers with constant turn (CT) rate ω as follows

$$\mathbf{F}_{\mathrm{CV}} = \begin{bmatrix} 1 & \Delta t & 0 & 0 \\ 0 & 1 & 0 & 0 \\ 0 & 0 & 1 & \Delta t \\ 0 & 0 & 0 & 1 \end{bmatrix},$$

$$\mathbf{F}_{\mathrm{CT}} = \begin{bmatrix} 1 & \frac{1}{\omega}\sin(\omega\Delta t) & 0 & -\frac{1}{\omega}[1 - \cos(\omega\Delta t)] \\ 0 & \cos(\omega\Delta t) & 0 & -\sin(\omega\Delta t) \\ 0 & \frac{1}{\omega}[1 - \cos(\omega\Delta t)] & 1 & \frac{1}{\omega}\sin(\omega\Delta t) \\ 0 & \sin(\omega\Delta t) & 0 & \cos(\omega\Delta t) \end{bmatrix}$$

The modeling error random process $\mathbf{w}_k$ in (4.1) is assumed zero-mean additive white Gaussian with covariance matrix

$$\mathbf{Q} = q \begin{bmatrix} \Delta t^3/3 & 0 & \Delta t^2/2 & 0 \\ \Delta t^2/2 & 0 & \Delta t & 0 \\ 0 & \Delta t^3/3 & 0 & \Delta t^2/2 \\ 0 & \Delta t^2/2 & 0 & \Delta t \end{bmatrix}$$

where q is a constant scaling term.

4.1.2 Measurement Model

We assume that, at time step k, the M_k measurements, $\mathbf{Z}_k = \{\mathbf{z}_{k,1}, \ldots \mathbf{z}_{k,M_k}\}$, form a random finite set [19]. We also assume that there are N_r possible combinations of measurement paths or regions from the targets as well as clutter. For example, two possible paths from the radar to the target is an LOS path and a path due to an one-bounce reflection off a building. Depending on the different types of measurements, we denote by $\rho_{k,l}$ the region in the 2-D plane where the lth target is located at time step k. For example, one region may consist of only LOS measurements for the lth target, whereas another region may consist of both LOS and one-bounce reflections off a specific wall of a building.

The ith measurement at time step k, $\mathbf{z}_{k,i} = [r_{k,i} \; \dot{r}_{k,i}]^{\mathrm{T}}$, consists of range $r_{k,i}$ and range rate $\dot{r}_{k,i}$ measurements, $i = 1, \ldots, M_k$. The model for the measurement generated from the lth target with state vector $\mathbf{x}_{k,l}$ in region $\rho_{k,l}$ depends on the function $\mathbf{h}_{k,i}(\cdot)$, and it is given by

$$\mathbf{z}_{k,i} = \mathbf{h}_{k,i}(\mathbf{x}_{k,l}, \rho_{k,l}) + \mathbf{v}_{k,i},$$

30

where $\mathbf{v}_{k,i}$ is the corresponding measurement noise. Next, we provide this model relationship between range and range-rate measurements and target state $\mathbf{x}_{k,l}$ for different regions.

Model for LOS-only Region

An LOS path is obtained when the transmitted signal directly reaches the target or the path is independent of the building walls. Assuming the airborne radar is located at (x_R, y_R, z_R), the range of the lth target associated with an LOS path is given by

$$r_{k,l}^{(\text{LOS})} = \sqrt{(x_{k,l} - x_R)^2 + (y_{k,l} - y_R)^2 + z_R^2}, \tag{4.2}$$

and the corresponding range-rate is given by

$$\dot{r}_{k,l}^{(\text{LOS})} = \Big((x_{k,l} - x_R)\, \dot{x}_{k,l} + (y_{k,l} - y_R)\, \dot{y}_{k,l} \Big) / r_{k,l}^{(\text{LOS})}. \tag{4.3}$$

Note that, as the height of the radar and the target are assumed to remain the same during tracking, we do not include a range-rate contribution in the z-direction.

Model for One-bounce Multipath Region

If the measurement $\mathbf{z}_{k,i}$ is obtained from a target multipath reflection, then the measurement model depends on the geometry between the target and the building that the signal reflected off as well as the total number of signal reflections. The specular multipath phenomenology in the X band in urban areas is well-known, particularly in SAR [76, 77], where reconstructed images exhibit bright spots due to corner-reflector returns from building-road intersections [78]. Here, we assume that all reflections are specular, or that the angle of incidence equals the angle of reflection for all reflected rays.

We assume that there are $\mathcal{L}$ buildings in the surveillance area and that each building has $\mathcal{J}$ walls. We denote by $w_{\ell,j}$ the jth wall of the ℓth building, $\ell = 1, \ldots, \mathcal{L}$

and $j = 1, \ldots, \mathcal{J}$. Whereas in [1] we assumed that the buildings have prism shapes, with all the walls either parallel or perpendicular to the x-coordinate and the y-coordinate, here we assume that the building can have any shape and the walls can be in any direction. Fig. 4.1 demonstrates the path of a single-bounce reflection from wall $w_{\ell,j}$.
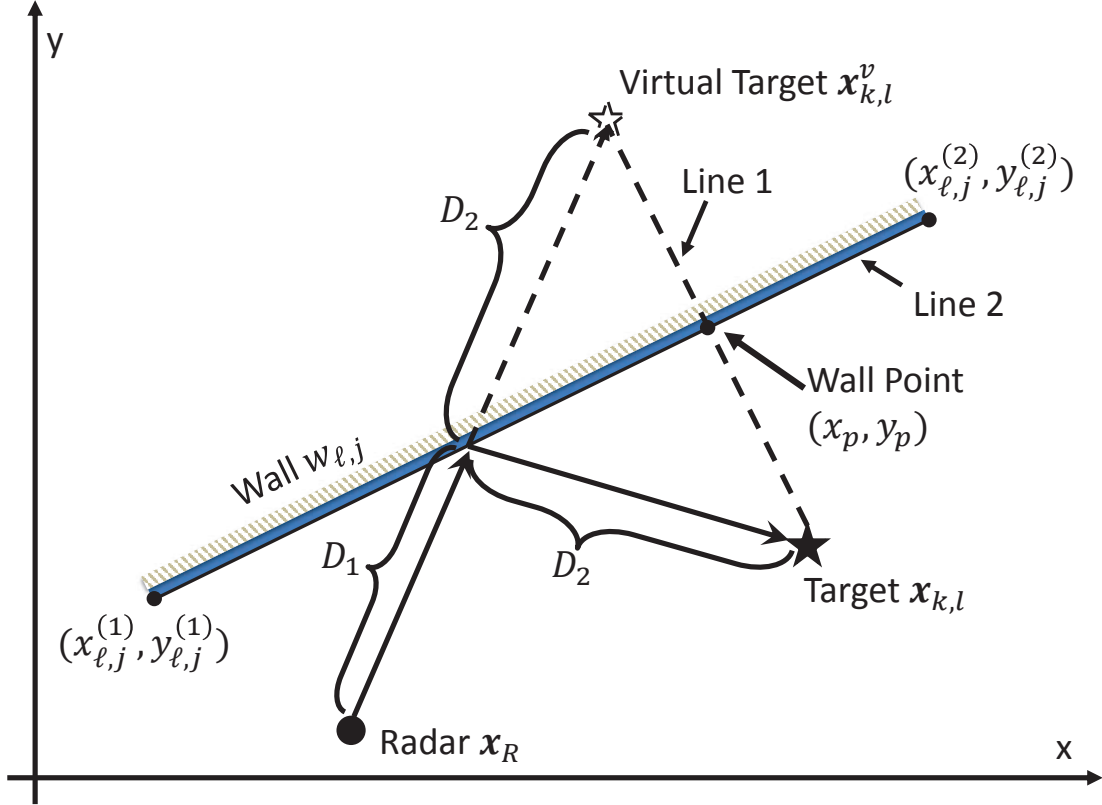
Figure 4.1: 2-D Geometry of The True Target $\mathbf{x}_{k,l}$, Virtual Target $\mathbf{x}_{k,l}^v$, and Building Wall $w_{\ell,j}$ After One Bounce.

The range from the radar to the target $\mathbf{x}_{k,l}$ can be calculated as $r_{k,l}^{(w_{\ell,j})} = D_1 + D_2$. As the multipath is due to a specular reflection, the distance between the radar and the true target is equal to the distance between the radar and the virtual target. Thus, the range and range-rate of the signal reflected once from the jth wall of the
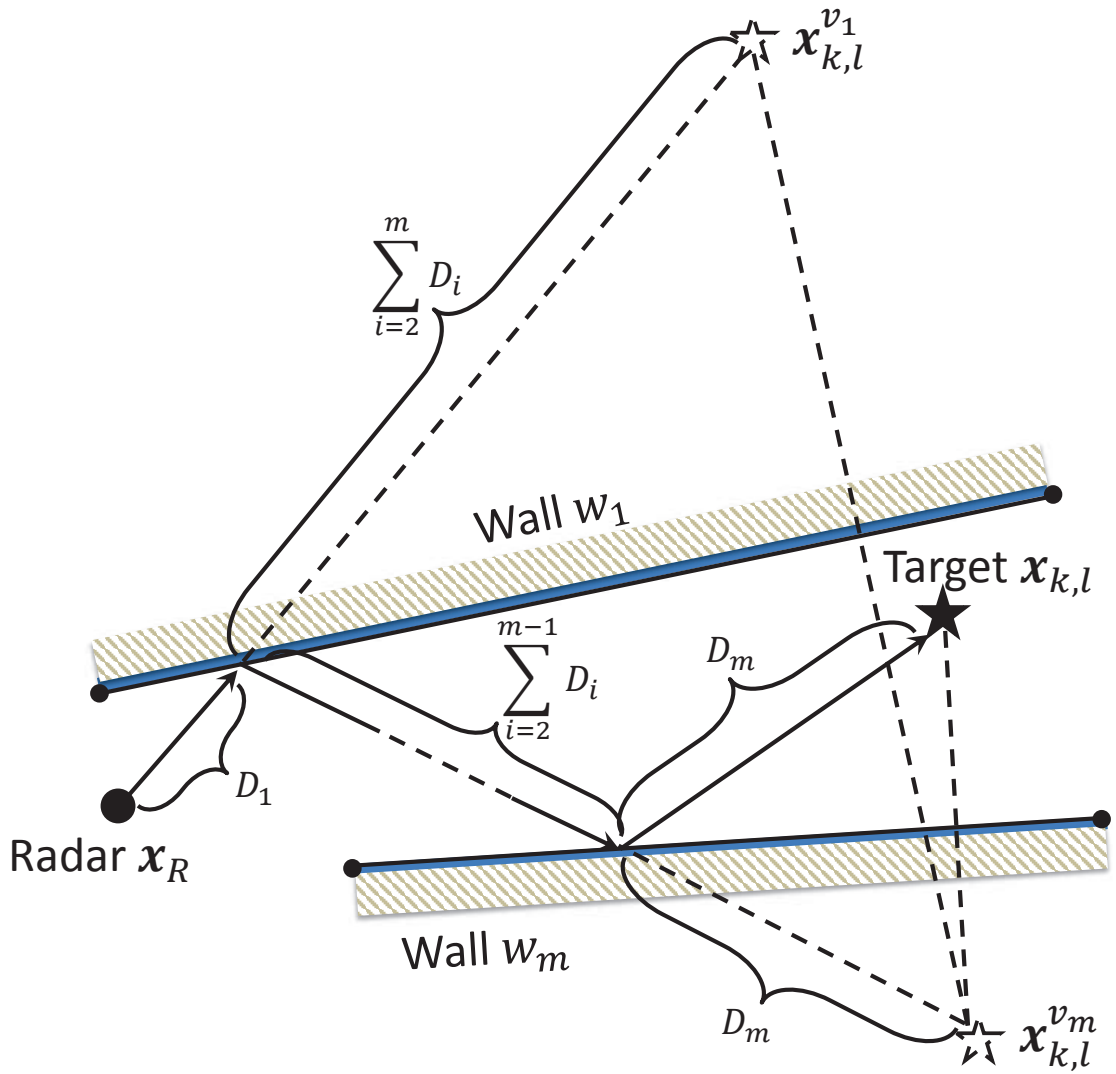
Figure 4.2: Geometry of The True Target, Multiple Virtual Targets, and Building Walls After m Bounces.

Step I: Find point (x_p, y_p) on $w_{\ell,j}$ (jth wall of ℓth building)

I(a) Line 2 is the line between points $\left(x_{\ell,j}^{(1)}, y_{\ell,j}^{(1)}\right)$ and $\left(x_{\ell,j}^{(2)}, y_{\ell,j}^{(2)}\right)$ on wall $w_{\ell,j}$. Find slope of Line 2:
$$\alpha_2 = (y_{\ell,j}^{(1)} - y_{\ell,j}^{(2)})/(x_{\ell,j}^{(1)} - x_{\ell,j}^{(2)})$$

I(b) Line 1 is the line between point (x_p, y_p) and the target location $(x_{k,l}, y_{k,l})$. Find slope of Line 1:
$$\alpha_1 = (y_p - y_{k,l})/(x_p - x_{k,l})$$

I(c) Since Line 1 and Line 2 are orthogonal, relate slopes
$$\alpha_1 = -1/\alpha_2$$

I(d) Relate slope α_2 and point (x_p, y_p) on Line 1
$$\alpha_2 = \left(y_p - y_{\ell,j}^{(2)}\right)/\left(x_p - x_{\ell,j}^{(2)}\right)$$

I(e) Solve for (x_p, y_p) using the relations in I(a)-I(d)

Step II: Use (x_p, y_p) to find lth virtual target location:
$$x_{k,l}^v = 2x_p - x_{k,l}, \quad y_{k,l}^v = 2y_p - y_{k,l}$$

Table 1: Computation of The 2-D Location of The lth Virtual Target Assuming One-Bounce From Wall $w_{\ell,j}$, As in Fig. 4.1.

ℓth building, can be calculated, respectively, as

$$r_{k,l}^{(w_{\ell,j})} = \sqrt{(x_{k,l}^v - x_R)^2 + (y_{k,l}^v - y_R)^2 + z_R^2}, \tag{4.4}$$

$$\dot{r}_{k,l}^{(w_{\ell,j})} = \left((x_{k,l}^v - x_R)\dot{x}_{k,l}^v + (y_{k,l}^v - y_R)\dot{y}_{k,l}^v\right)/r_{k,l}^{(w_{\ell,j})}, \tag{4.5}$$

where $(x_{k,l}^v, y_{k,l}^v)$ and $(\dot{x}_{k,l}^v, \dot{y}_{k,l}^v)$ are the 2-D location and velocity coordinates of the virtual target, respectively. The location of the virtual target $\mathbf{x}_{k,l}^v$ can be computed using specular reflection properties as summarized in Table 1. For this computation, we assume that the coordinates of the two corner points, $(x_{\ell,j}^{(1)}, y_{\ell,j}^{(1)})$ and $(x_{\ell,j}^{(2)}, y_{\ell,j}^{(2)})$, of the jth wall of the ℓth building are known.

Model for Multiple-bounces Region

We extend the model for one-bounce measurement to m bounces off multiple buildings. Fig. 4.2 demonstrates the relationship between the radar, the true target, m

Step I: Use point on wall w_m and target location $\mathbf{x}_{k,l}$ in Table 1 to obtain location of the mth virtual target $\mathbf{x}_{k,l}^{v_m}$
Step II: For $i = 2, \ldots, m$, use point on wall w_{m+1-i} and virtual target location $\mathbf{x}_{k,l}^{v_{m+2-i}}$ to obtain $\mathbf{x}_{k,l}^{v_{m+1-i}}$
Virtual target location after m bounces: $\mathbf{x}_{k,l}^{v} = \mathbf{x}_{k,l}^{v_1}$

Table 2: Obtain Virtual Target Location $\mathbf{x}_{k,l}^{v}$ After m Bounces.

walls and m virtual targets. We assume that, at time step k, the transmitted signal is reflected m times from walls in the order of $\{w_1, w_2, \ldots, w_m\}$. As the final measurement does not depend on the sides of the walls of the different buildings, we now denote the ith reflected wall as w_i, $i = 1, \ldots, m$. From Fig. 4.2, the range of the lth target can be calculated as $r_{k,l}^{(m)} = \sum_{i=1}^{m} D_i$. Due to specular reflections, the distance between the radar location $\mathbf{x}_R$ and the true target location $\mathbf{x}_{k,l}$ can be calculated as the distance between the radar and the virtual target $\mathbf{x}_{k,l}^{v_1} = \mathbf{x}_{k,l}^{v}$. The steps for computing the location of the virtual point $\mathbf{x}_{k,l}^{v}$ are summarized in Table 2. Using this location, we can obtain the range and range-rate measurements, respectively, of the lth target at time step k after m paths as

$$
\begin{aligned}
r_{k,l}^{(m)} &= \sqrt{(x_{k,l}^{v} - x_R)^2 + (y_{k,l}^{v} - y_R)^2 + z_R^2} \\
\dot{r}_{k,l}^{(m)} &= \left((x_{k,l}^{v} - x_R)\dot{x}_{k,l}^{v} + (y_{k,l}^{v} - y_R)\dot{y}_{k,l}^{v} \right) / r_{k,l}^{(m)} .
\end{aligned}
$$

4.1.3 Test Urban Environment Measurement Model

We consider a test urban environment that follows the road map in Fig. 4.3. We assume that the SNR in the LOS region is 20 dB and that every additional reflection off a building wall results in about 10 dB signal energy loss [1]. Multipath returns from more than two reflections are ignored as the signal strength is too weak to be

detected by the radar. As a result, we only consider signal reflection paths up to two bounces. For this test environment, there are five possible different measurement models: Model 1 (M1, LOS-only), Model 2 (M2, LOS and one-bounce), Model 3 (M3, one-bounce), Model 4 (M4, two one-bounces), and Model 5 (M5, no measurement due to shadowing). Table 3 provides eight possible regions (or path combinations) with the indicated measurement models for the test urban environment.
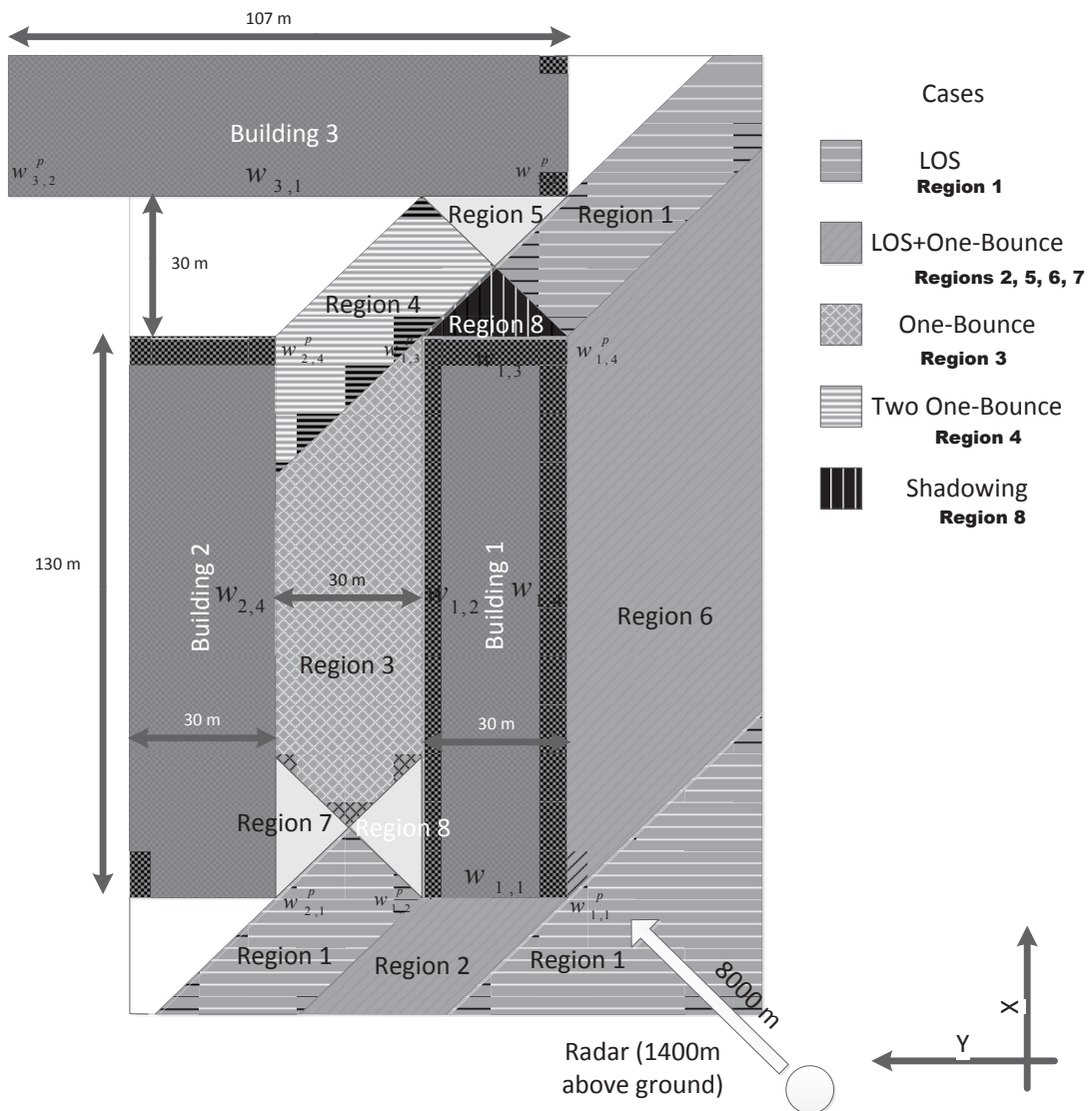

Figure 4.3: Simulated Map of Test Urban Environment [1].

Region 1:	LOS (M1)
Region 2:	LOS and one-bounce from wall $w_{1,1}$ (M2)
Region 3:	One-bounce from wall $w_{2,4}$ (M3)
Region 4:	Two one-bounces from walls $w_{2,4}$, $w_{3,1}$ (M4)
Region 5:	LOS and one-bounce from wall $w_{3,1}$ (M2)
Region 6:	LOS and one-bounce from wall $w_{1,4}$ (M2)
Region 7:	LOS and one-bounce from wall $w_{2,4}$ (M2)
Region 8:	Shadowing (M5)

Table 3: Eight Possible Regions Corresponding to Five Possible Measurement Models for The Test Urban Environment.

LOS-only region: When a target is in the LOS-only region, there is only one measurement (Model M1) generated by the target and is given by

$$\mathbf{z}_{k,i}^{\text{(LOS)}} = 2 \left[r_{k,l}^{\text{(LOS)}} \quad \dot{r}_{k,l}^{\text{(LOS)}} \right]^{\mathsf{T}} + \mathbf{v}_{k,i}, \tag{4.6}$$

where $r_{k,l}^{\text{(LOS)}}$ and $\dot{r}_{k,l}^{\text{(LOS)}}$ are defined in (4.2) and (4.3), respectively. Note that range and range-rate appear twice in (4.6) since we assume a transceiver radar system; the measurement includes the signal transmitted from the radar to the target and the signal reflection from the target to the radar.

LOS and one-bounce from wall $w_{\ell,j}$ region: There are two paths combined in this measurement model (Model M2), LOS and multipath from wall $w_{\ell,j}$. This provides three possible measurement combinations, radar–target–radar, radar–wall–target–wall–radar and radar–wall–target–radar paths, generated by the lth target that are given by the RFS $\{\mathbf{z}_{k,i}^{\text{(LOS)}}, \mathbf{z}_{k,i}^{(w_{\ell,j})}, \mathbf{z}_{k,i}^{\text{(LOS, }w_{\ell,j})}\}$. Here, $\mathbf{z}_{k,i}^{\text{(LOS)}}$ is given in (4.6), and

$$\mathbf{z}_{k,i}^{(w_{\ell,j})} = 2 \left[r_{k,l}^{(w_{\ell,j})} \quad \dot{r}_{k,l}^{(w_{\ell,j})} \right]^{\mathsf{T}} + \mathbf{v}_{k,i} \tag{4.7}$$

$$\mathbf{z}_{k,i}^{\text{(LOS, }w_{\ell,j})} = \left[(r_{k,l}^{(w_{\ell,j})} + r_{k,l}^{\text{(LOS)}}) \quad (\dot{r}_{k,l}^{(w_{\ell,j})} + \dot{r}_{k,l}^{\text{(LOS)}}) \right]^{\mathsf{T}} + \mathbf{v}_{k,i}, \tag{4.8}$$

where $r_{k,l}^{(w_{\ell,j})}$ and $\dot{r}_{k,l}^{(w_{\ell,j})}$ are given in (4.4) and (4.5), respectively. Note that this

measurement RFS is in Regions 2, 5, 6, and 7 for the indicated walls in Table 3.

One-bounce from wall $w_{\ell,j}$ region: If there is only one-bounce from wall $w_{\ell,j}$, then the target generates one measurement (Model M3), $\mathbf{z}_{k,i}^{(w_{\ell,j})}$ in (4.7), corresponding to the radar–wall–target–wall–radar path. This measurement RFS is in Region 3 of the test environment.

Two one-bounces from walls w_{ℓ_1,j_1} and w_{ℓ_2,j_2} region: If there are two one-bounces, then the target can generate three possible measurement combinations, radar–w_{ℓ_1,j_1}–target–w_{ℓ_1,j_1}–radar, radar–w_{ℓ_2,j_2}–target–w_{ℓ_2,j_2}–radar, and radar–w_{ℓ_1,j_1}–target–w_{ℓ_2,j_2}–radar.

The resulting RFS measurement set (Model M4) is given by $\{\mathbf{z}_{k,i}^{(w_{\ell_1,j_1})}, \ \mathbf{z}_{k,i}^{(w_{\ell_2,j_2})}, \ \mathbf{z}_{k,i}^{(w_{\ell_1,j_1},\ w_{\ell_2,j_2})}\}$, where $\mathbf{z}_{k,i}^{(w_{\ell_1,j_1})}$ and $\mathbf{z}_{k,i}^{(w_{\ell_2,j_2})}$ are defined in (4.7) and

$$\mathbf{z}_{k,i}^{(w_{\ell_1,j_1},\ w_{\ell_2,j_2})} = [r_{k,l}^{(w_{\ell_1,j_1})} + r_{k,l}^{(w_{\ell_2,j_2})} \ \dot{r}_{k,l}^{(w_{\ell_1,j_1})} + \dot{r}_{k,l}^{(w_{\ell_2,j_2})}]^{\mathbf{T}} + \mathbf{v}_{k,i}.$$

This measurement RFS is in Region 4 of the test environment.

Shadowing region: If a target is in the shadowing region, no measurement is observed (Model M5); this is the case for Region 8 of the test environment.

4.1.4   Clutter Model

We assume a uniformly distributed clutter model in a validation region with volume V_k. Measurements within the validation region are used to update the tracking, whereas measurements outside the validation region are discarded. The probability that m false alarms are obtained at time k is $\Pr(m_k = m) = \exp(-\zeta V_k)(\zeta V_k)^m/(m!)$. Here, we assume that the number of false alarms is Poisson distributed with average ζV_k, where ζ is the clutter density [78]. For urban environments, the probability of detection, P_{D}, varies dynamically for a given desirable probability of false alarm P_{FA} since it depends on the signal-to-noise ratio $\mathrm{SNR}_{\rho_{k,l}}$ at region $\rho_{k,l}$ of the predicted

target position. Specifically, the probability of detection is $P_\mathrm{D} = P_\mathrm{FA}^{1/(1+\mathrm{SNR}_{\rho_{k,l}})}$.

4.2   Multiple Target Tracking with MMA

4.2.1   Probability Hypothesis Density Filter

Given $\mathbf{X}_{k-1} = \{\mathbf{x}_{k-1,1}, \ldots, \mathbf{x}_{k-1,L_k}\}$, the multi-target state RFS at time $k-1$, the state RFS at time k is formed by combining the RFS of targets that remain in the FOV from the previous time step $\mathbf{X}_{k|k-1}^\mathrm{rem}$, of targets spawned from the previous time step $\mathbf{X}_{k|k-1}^\mathrm{sp}$, and of new targets that enter the FOV $\mathbf{X}_k^\mathrm{new}$. The measurement RFS can consist of both targets as well as clutter $\mathbf{Z}_k^\mathrm{clt}$ at time step k. It is assumed that the clutter and target measurement RFS are independent and the target measurement RFS are mutually independent.

The PF-PHD uses the assumption that the predicted multiple-target posterior density $p(\mathbf{x}_k|\mathbf{Z}_{k-1})$ can be characterized by the intensity function (IFN) $\lambda(\mathbf{x}_k|\mathbf{Z}_{k-1})$. Thus, given the posterior INF $\lambda(\mathbf{x}_{k-1}|\mathbf{Z}_{k-1})$ at time step $k-1$, the predicted INF at time step k can be obtained as

$$\lambda(\mathbf{x}_k|\mathbf{Z}_{k-1}) = \int \Big[\mathrm{P}_{k|k-1}^\mathrm{rem}(\mathbf{x}_{k-1}) p(\mathbf{x}_k|\mathbf{x}_{k-1}) + \lambda^\mathrm{sp}(\mathbf{x}_k|\mathbf{Z}_{k-1}) \Big]$$
$$\cdot \lambda(\mathbf{x}_{k-1}|\mathbf{Z}_{k-1}) \, d\mathbf{x}_{k-1} + \lambda^\mathrm{new}(\mathbf{x}_k|\mathbf{Z}_k) \tag{4.9}$$

where $\lambda^\mathrm{sp}(\mathbf{x}_k|\mathbf{Z}_{k-1})$ is the INF of the targets spawned at the previous time step $(k-1)$, $\lambda^\mathrm{new}(\mathbf{x}_k|\mathbf{Z}_k)$ is the INF of new targets entering the FOV, and $\mathrm{P}_{k|k-1}^\mathrm{rem}(\mathbf{x}_{k-1})$ is the probability that a target present at $k-1$ remains in the FOV at k. The posterior INF is given by

$$\lambda(\mathbf{x}_k|\mathbf{Z}_k) = (1 - \mathrm{P}_\mathrm{D}(\mathbf{x}_k)) \, \lambda(\mathbf{x}_k|\mathbf{Z}_{k-1}) +$$
$$\sum_{\mathbf{z}_{k,i} \in \mathbf{Z}_k} \frac{\mathrm{P}_\mathrm{D}(\mathbf{x}_k) \, p(\mathbf{z}_{k,i}|\mathbf{x}_k) \, \lambda(\mathbf{x}_k|\mathbf{Z}_{k-1})}{\lambda(\mathbf{Z}_k^\mathrm{clt}) + \int \mathrm{P}_\mathrm{D}(\tilde{\mathbf{x}}_k) p(\mathbf{z}_{k,i}|\tilde{\mathbf{x}}_k) \lambda(\tilde{\mathbf{x}}_k|\mathbf{Z}_{k-1}) d\tilde{\mathbf{x}}_k} \tag{4.10}$$

where $\lambda(\mathbf{Z}_k^{\mathrm{clt}})$ is the clutter INF and $\mathrm{P_D}(\mathbf{x}_k)$ is the probability that a target present at time k is detected at k. The estimate of the number of targets present at time k is given by $\hat{N}_k = \int \lambda(\mathbf{x}_k|\mathbf{Z}_k)d\mathbf{x}_k$.

Nonlinear and non-Gaussian target dynamic models can be incorporated in tracking multiple targets by implementing the PHD filter using the PF. At each time step, the PF-PHD approximates the posterior INF by a weighted set of particles, and at the end of every recursion, the multiple target states can be estimated using standard clustering techniques such as k-means. The number of targets can be estimated by summing the particle weights. In particular, the PF-PHD assumes that the posterior INF is approximated using N_{k-1} particles $\mathbf{x}_{k-1}^{(n)}$ and normalized weights $w_{k-1}^{(n)}$, $n = 1, \ldots, N_{k-1}$ as

$$\lambda(\mathbf{x}_{k-1}|\mathbf{Z}_{k-1}) \approx \sum_{n=1}^{N_{k-1}} w_{k-1}^{(n)}\delta(\mathbf{x}_{k-1} - \mathbf{x}_{k-1}^{(n)}).$$

The predicted INF $\lambda(\mathbf{x}_k|\mathbf{Z}_{k-1})$ in (4.9) is approximated as

$$\lambda(\mathbf{x}_k|\mathbf{Z}_{k-1}) \approx \sum_{n=1}^{N_{k-1}+B_k} w_{k|k-1}^{(n)}\delta(\mathbf{x}_k - \mathbf{x}_k^{(n)}),$$

where M_k is the number of particles required to represent the new target RFS at time k. The particles are obtained using two important sampling densities

$$\mathbf{x}_k^{(n)} \sim \begin{cases} q_k(\cdot|\mathbf{x}_{k-1}^{(n)}, \mathbf{Z}_k), & n = 1, \ldots, N_{k-1} \\[2ex] p_k(\cdot|\mathbf{Z}_k), & n = N_{k-1} + 1, \ldots, N_{k-1} + B_k, \end{cases}$$

where we select $q_k(\cdot|\mathbf{x}_{k-1}^{(n)}, \mathbf{Z}_k) = p_k(\cdot|\mathbf{x}_{k-1}^{(n)})$. The weights are

$$w_k^{(n)} = \begin{cases} \dfrac{\phi_{k|k-1}(\mathbf{x}_k^{(n)})\, w_{k-1}^{(n)}}{q_k(\mathbf{x}_k^{(n)}|\mathbf{x}_{k-1}^{(n)}, \mathbf{Z}_k)}, & n = 1, \ldots, N_{k-1}, \\[3ex] \dfrac{\lambda^{\mathrm{new}}(\mathbf{x}_k^{(n)}|\mathbf{Z}_k)}{B_k\, p_k(\mathbf{x}_k^{(n)}|\mathbf{Z}_k)}, & n = N_{k-1} + 1, \ldots, N_{k-1} + B_k, \end{cases}$$

where

$$\phi_{k|k-1}(\mathbf{x}_k^{(n)}) = \mathrm{P}_{k|k-1}^{\mathrm{rem}}(\mathbf{x}_{k-1}^{(n)})\, p(\mathbf{x}_k^{(n)}|\mathbf{x}_{k-1}^{(n)}) + \lambda^{\mathrm{sp}}(\mathbf{x}_k^{(n)}|\mathbf{Z}_{k-1}).$$

The posterior INF at time k is approximated as

$$\lambda(\mathbf{x}_k|\mathbf{Z}_k) \approx \sum_{n=1}^{N_{k-1}+B_k} w_k^{(n)}\delta(\mathbf{x}_k - \mathbf{x}_k^{(n)}),$$

where

$$w_k^{(n)} = \left[1 - \mathrm{P_D}(\mathbf{x}_k^{(n)}) + \sum_{\mathbf{z}_{k,i}\in\mathbf{Z}_k} \frac{\mathrm{P_D}(\mathbf{x}_k^{(n)})p(\mathbf{z}_{k,i}|\mathbf{x}_k^{(n)})}{\lambda^{\mathrm{clt}}(\mathbf{z}_{k,i}) + \Phi_k(\mathbf{z}_{k,i})}\right] w_{k|k-1}^{(n)},$$

and

$$\Phi_k(\mathbf{z}_{k,i}) = \sum_{n=1}^{N_{k-1}+B_k} \mathrm{P_D}(\mathbf{x}_k^{(n)})\, p(\mathbf{z}_{k,i}|\mathbf{x}_k^{(n)})w_{k|k-1}^{(n)}.$$

For maneuvering target tracking, the interactive multiple model (IMM) approach is incorporated to allow for multiple dynamic state models in (4.1) with $\mathbf{F}$ varying to allow for constant velocity, $\mathbf{F}_{\mathrm{CV}}$, and constant turning $\mathbf{F}_{\mathrm{CT}}$ [3]. At each time step, the PF-PHD with IMM assumes that the state model can switch according to the transitional probability matrix $\prod = \{\pi_{ij}\}$. In particular, if $\varpi_{k-1}^{(n)} = i$ is the state model number index of the nth particle at time $k-1$, then it transitions to the number index j with probability π_{ij} at time k.

4.2.2 Multipath-to-Measurement Association

In urban environments, each target can generate multiple measurements, as discussed in the previous section. When tracking a single target, LOS and multipath measurements can be separated based on the time of arrival and strength of the return signal. However, when tracking multiple targets, and the number of targets varies dynamically, then it is difficult to associate a received measurement with a different

signal path. We propose to use multipath-to-measurement association in order to deal with this association problem. The MMA is based on computing the likelihood probabilities from all possible paths and then selecting as the path the one with the maximum likelihood at each tracking iteration. If we assume that at time step k the nth particle $\mathbf{x}_k^{(n)}$ is associated with $\mathcal{D}_k^{(n)}$ possible paths, then the path likelihood probability (PLP) between the nth particle $\mathbf{x}_k^{(n)}$ and the ith measurement $\mathbf{z}_{k,i}$ is

$$p^{(\text{MMA})}(\mathbf{z}_{k,i}|\mathbf{x}_k^{(n)}) = \arg \max_{j=1,2,\ldots \mathcal{D}_k^{(n)}} p(\mathbf{z}_{j,k}^{(n)}|\mathbf{z}_{k,i}),$$

where the jth path $p(\mathbf{z}_{j,k}^{(n)}|\mathbf{z}_{k,i})$ is assumed Gaussian with mean $\mathbf{z}_{k,i}$ and covariance Σ_j, and $\mathbf{z}_{j,k}^{(n)}$ is the predicted measurement from the jth path of the nth particle. Note that, integrating MMA with the PF-PHD does not require association between the path measurements originating from the same target; this would be computationally intensive and very difficult for an increased number of targets. For the MMA, we only need to select the likelihood probability from the most likely path and use it as a substitute for the likelihood probability; this probability is large when the measurement is associated to the correct target and small when the measurement is associated to a different target.

4.2.3 Adaptive k-means Clustering Algorithm

As the PF-PHD-MMA uses the path likelihood probability, it cannot directly estimate the correct number of targets as it also gives information on virtual targets (from multipath measurements). We thus adapt the k-means clustering algorithm to estimate the number of actual targets and their corresponding states. Applying the k-means algorithm at time step k clusters the particles into L_k groups $\mathbf{X}_{k,l}$ with corresponding nearest mean vector $\hat{\mathbf{x}}_{k,l}$, $l = 1, \ldots, \hat{L}_k$. Then, the algorithm calculates the maximum average distance between subgroup particles and their corresponding

mean as $\arg\max_{l=1,\dots,\hat{L}_k} E[\|\hat{\mathbf{x}}_{k,l} - \mathbf{x}_k^{(n)}\|]$ for $\mathbf{x}_k^{(n)} \in \mathbf{X}_{k,l}$, where $E[\cdot]$ denotes statistical expectation. The distance is compared to a pre-set threshold. If the distance exceeds the threshold, the number of clusters increases by one; if the distance does not exceed the threshold, then the number of clusters is the estimated number of targets and the mean vectors are the estimated target states.

The overall PF-PHD-MMA algorithm for tracking multiple targets in urban environments is summarized in Table 4.

4.3   Simulation

We demonstrate the performance of the proposed PF-PDF-MMA algorithm by simulating the tracking of multiple targets in the test urban environment in Figure 4.3. The scene has three buildings, an airborne radar located at

$(x_R, y_R, z_R) = (-5, 660, -5, 660, 1, 400)$ m (approximately 8 km southeast of the scene), and ground vehicles are moving in 2-D around Building 1. All the possible measurements regions are listed in Table 3. The state vector for the maneuvering targets is given by (4.1), with angular turning rate $\omega = 2$ radians/s and $\Delta t = 1$ s. We use the OSPA metric to demonstrate the performance of the algorithm with metric order parameter $p = 1$ and cutoff distance between targets $c = 25$; this metric provides both a cardinality error (number of targets estimation error) and a state estimation mean-squared error (MSE) [51, 79].

Simulation example of two targets: Same Direction   In the first simulation example, we consider two (fixed number) ground-moving vehicles, whose trajectories and starting points are shown in Figure 4.4, from the test urban environment in Figure 4.3. The process noise intensity is assumed $q = 0.01$, and the probability of target survival is 1. When implementing the PF-PHD, we assign each target 2,000 particles,

---

Step 0. At time step $k = 0$ (initialize)

Draw particles $\mathbf{x}_0^{(n)}$ from Gaussian distribution, set weights $w_0^{(n)} = 1/N_0$, and assign $\varpi_0^{(n)} = 1$, $n = 1, \ldots, N_0$

For time step $k \geq 1$

Step 1. (Predict)

Transition model using Π: $\varpi_{k-1}^{(n)}$ to $\varpi_k^{(n)}$, $n = 1, \ldots N_{k-1}$

For $n = 1, \ldots, N_{k-1}$

$$\mathbf{x}_k^{(n)} \sim q(\cdot | \mathbf{x}_{k-1}^{(n)}, \varpi_k^{(n)}, \mathbf{Z}_k)$$
$$w_{k|k-1}^{(n)} = \phi_k(\mathbf{x}_k^{(n)}) \, w_{k-1}^{(n)} / q(\mathbf{x}_k^{(n)} | \mathbf{x}_{k-1}^{(n)}, \mathbf{Z}_k)$$

For $n = N_{k-1} + 1, \ldots, N_{k-1} + B_k$

$$\mathbf{x}_k^{(n)} \sim p(\cdot | \mathbf{Z}_k)$$
$$w_{k|k-1}^{(n)} = \lambda^{\text{new}}(\mathbf{x}_x) / (B_k \, p(\mathbf{x}_k^{(n)} | \mathbf{Z}_k))$$

Total number of particles $N_p = N_{k-1} + B_k$

Step 2. (update)

For $\mathbf{z}_{k,i} \in \mathbf{Z}_k$

$$p(\mathbf{z}_{k,i} | \mathbf{x}_k^{(n)}) = p^{(\text{MMA})}(\mathbf{z}_{k,i} | \mathbf{x}_k^{(n)}), \, n = 1, \ldots, N_p$$
$$\Phi_k(\mathbf{z}_{k,i}) = \sum_{n=1}^{N_p} P_D(\mathbf{x}_k^{(n)}) p(\mathbf{z}_{k,i} | \mathbf{x}_k^{(n)}) w_{k|k-1}^{(n)}$$

For $n = 1, \ldots, N_p$, update weight

$$w_k^{(n)} = w_{k|k-1}^{(n)} \left[1 - P_D(\mathbf{x}_k^{(n)}) + \right.$$
$$\left. \sum_{\mathbf{z}_{k,i} \in \mathbf{Z}_k} \frac{P_D(\mathbf{x}_k^{(n)}) p(\mathbf{z}_{k,i} | \mathbf{x}_k^{(n)}) w_{k|k-1}^{(n)}}{\lambda^{\text{clt}}(\mathbf{z}_{k,i}) + \Phi_k(\mathbf{z}_{k,i})} \right]$$

Step 3. (resample) $\{\mathbf{x}_k^{(n)}, w_k^{(n)}\}_{n=1}^{N_k} \longmapsto \{\mathbf{x}_k^{(n)}, w_k^{(n)}\}_{n=1}^{N_p}$

Step 4. Adaptive k-means to $\mathbf{x}_k^{(n)}$ to obtain $\hat{\mathbf{x}}_{k,l}$ and $\hat{L}_k$

Table 4: PF-PHD-MMA for Urban Environment.

and we assume that there is no target spawning and no new targets enter the FOV. The clutter RFS is assumed to be Poisson with density 1.67×10^{-4} (corresponding to 5 false alarms per unit validation gate volume). The clutter is assumed to be uniformly distributed between -50 m to 150 m in the y-direction and -100 m to 50 m in the x-direction. At the end of each iteration, the target states are estimated using the adaptive k-means clustering algorithm. The actual and estimated trajectories for this example are shown in Figure 4.5. The cardinality error is shown in Figure 4.6 and the overall OSPA metric after 100 Monte Carlo simulations is shown in Figure 4.7. As it can be seen, the algorithm tracks the number of targets as well as the target state even when there are no LOS measurements. The cardinality error is large at a few time steps, since when the targets move in opposite directions, their measurements are very similar to each other. Also, the performance decreases when the targets move into the shadowing region.

Simulation example of a time-varying number of targets: Three Targets
In this example, we consider tracking a time-varying number of targets. Initially, there are 2 targets moving clockwise along the same direction; at $k = 5$, a new target enters the FOV and moves along the same direction, a target leaves the FOV at $k = 12$ and all the targets leave the FOV at $k = 15$. The remaining simulations parameters remain the same as in the two-target example. The simulation results for the true and estimated trajectories and the cardinality error are shown in Figures 4.9 and 4.10, respectively. The OSPA metric after 100 Monte Carlo runs is shown in Figure 4.11. As it can be seen, the proposed algorithm can track a time-varying number of targets in the urban environment. In addition, the algorithm can track the number of targets well except when the targets move into the shadowing region. Note that, when there is a change in the number of targets, the OSPA error increases, as expected.
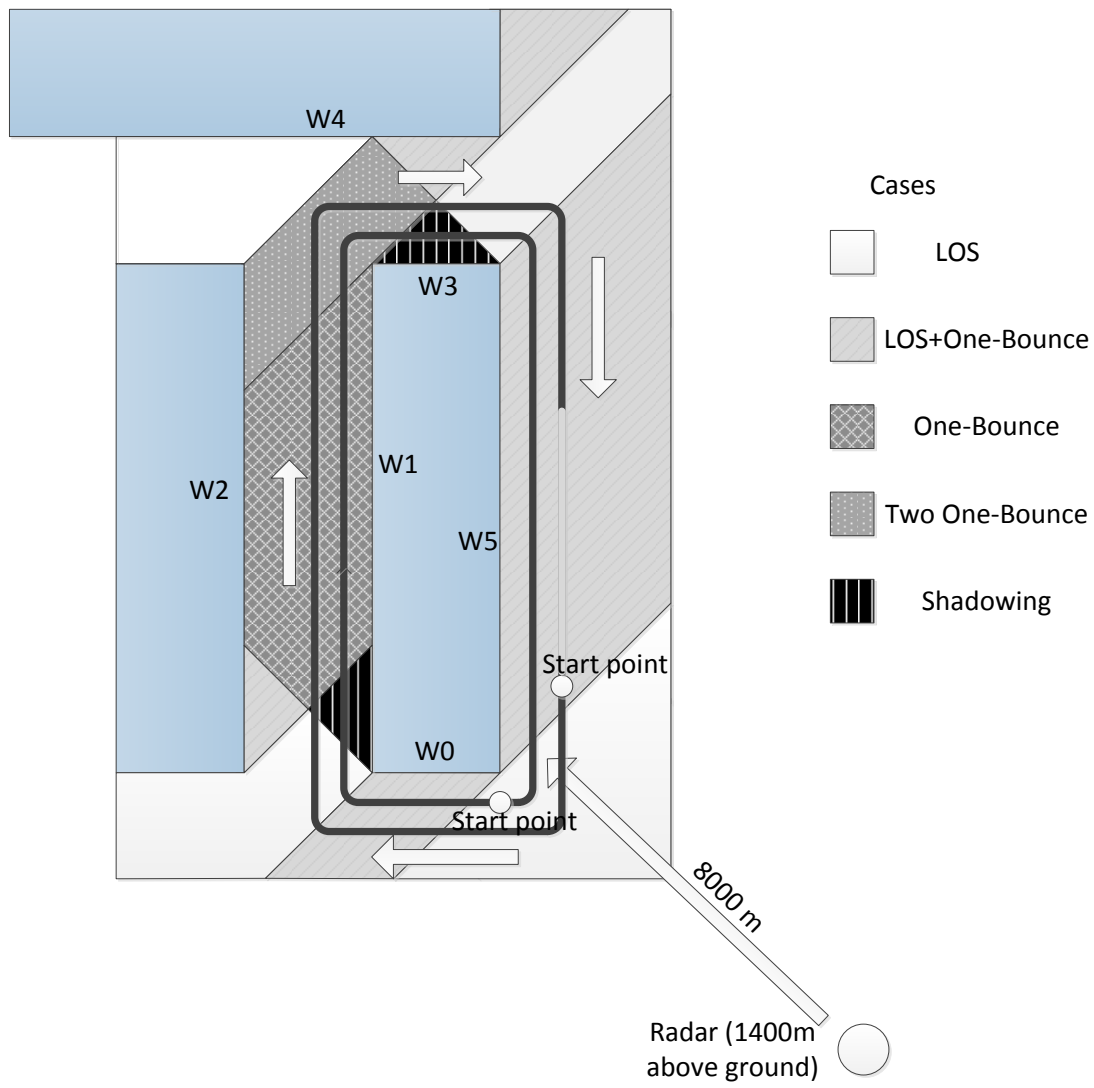
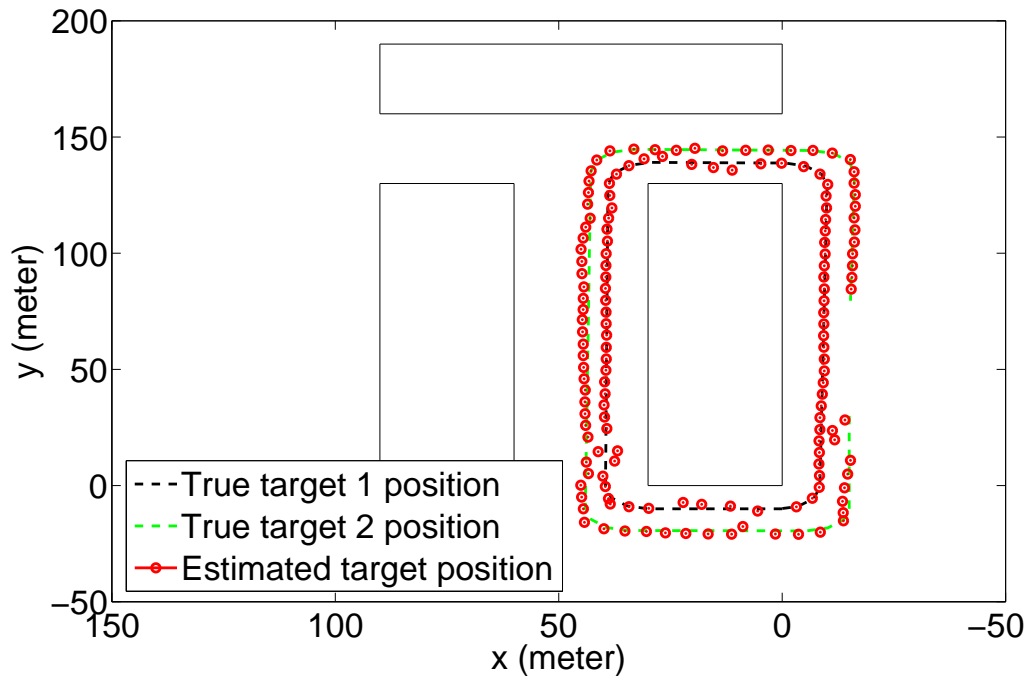**Figure 4.4:** Two Targets Moving in The Same Directions.

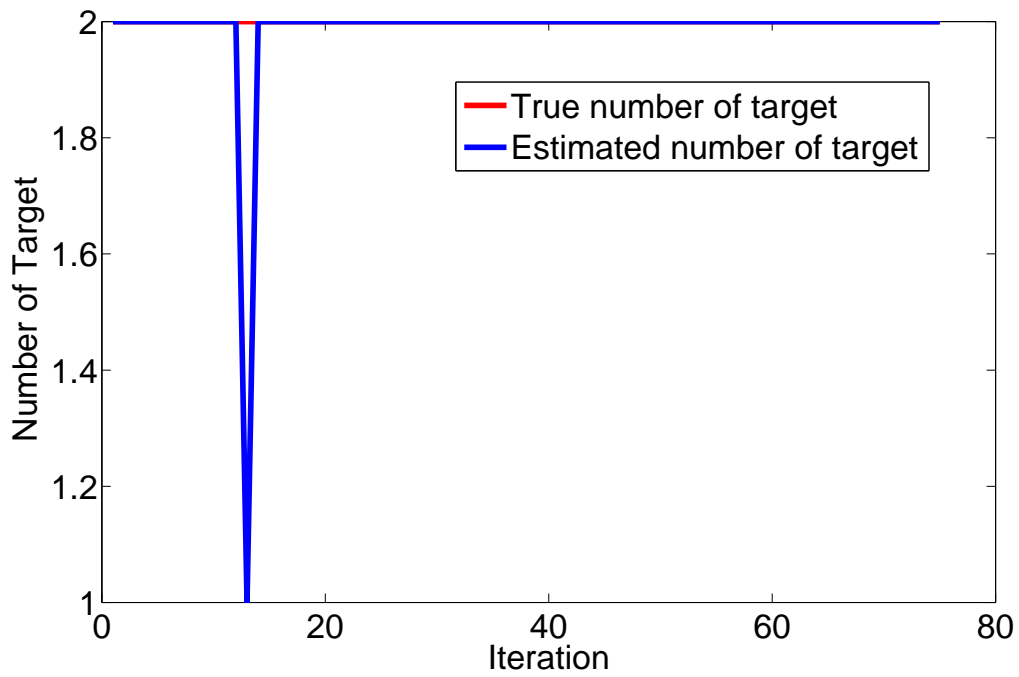**Figure 4.5:** Two Targets Moving in The Same Directions: 2-D True and Estimated Trajectories.

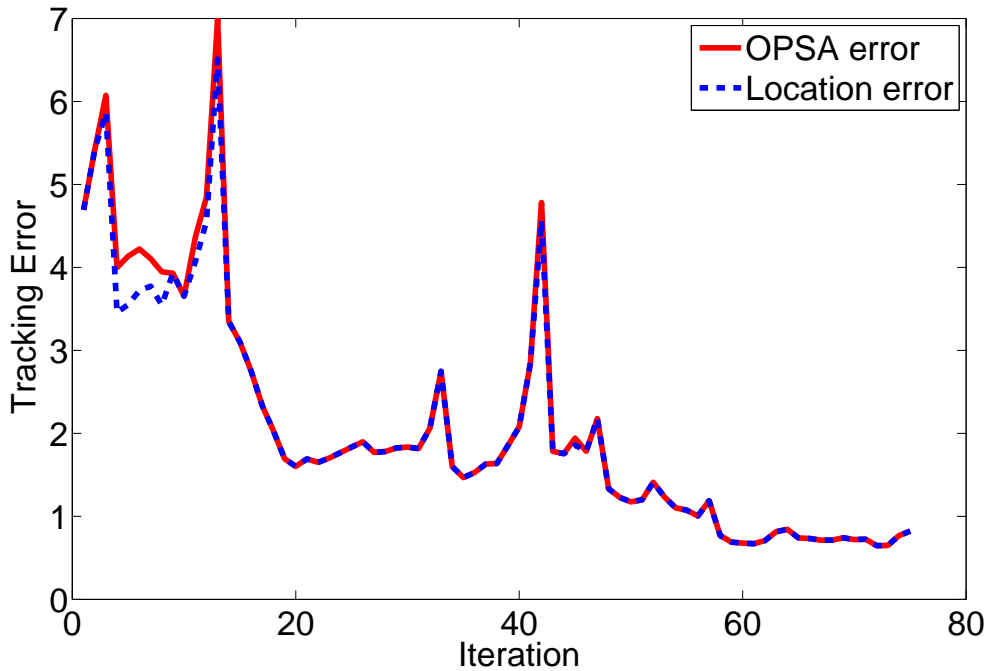**Figure 4.6:** Two Targets Moving in The Same Directions: Cardinality.

Figure 4.7: Two Targets Moving in The Same Directions: OSPA.

Simulation example of a time-varying number of targets: Four Targets In this example, we consider tracking a time-varying number of targets. Initially, there are 3 targets moving clockwise along the same direction; at $k=5$, a new target enters the FOV and moves along the same direction, a target leaves the FOV at $k=12$ and all the targets leave the FOV at $k=15$. The remaining simulations parameters remain the same as in the two-target example. The simulation results for the true and estimated trajectories and the cardinality error are shown in Figures 4.13 and 4.14, respectively. The OSPA metric after 100 Monte Carlo runs is shown in Figure 4.15. As it can be seen, the proposed algorithm can track a time-varying number of targets in the urban environment. In addition, the algorithm can track the number of targets well except when the targets move into the shadowing region. Note that, when there is a change in the number of targets, the OSPA error increases, as expected.

48

Figure 4.8: Time-Varying Number of Targets Moving in The Same Direction (Max 3).

Figure 4.9: Time-Varying Number of Targets Moving in The Same Direction (Max 3): 2-D True and Estimated Trajectories.

Figure 4.10: Time-Varying Number of Targets Moving in The Same Direction (Max 3): Cardinality.

Figure 4.11: Time-Varying Number of Targets Moving in The Same Direction (Max 3): OSPA.

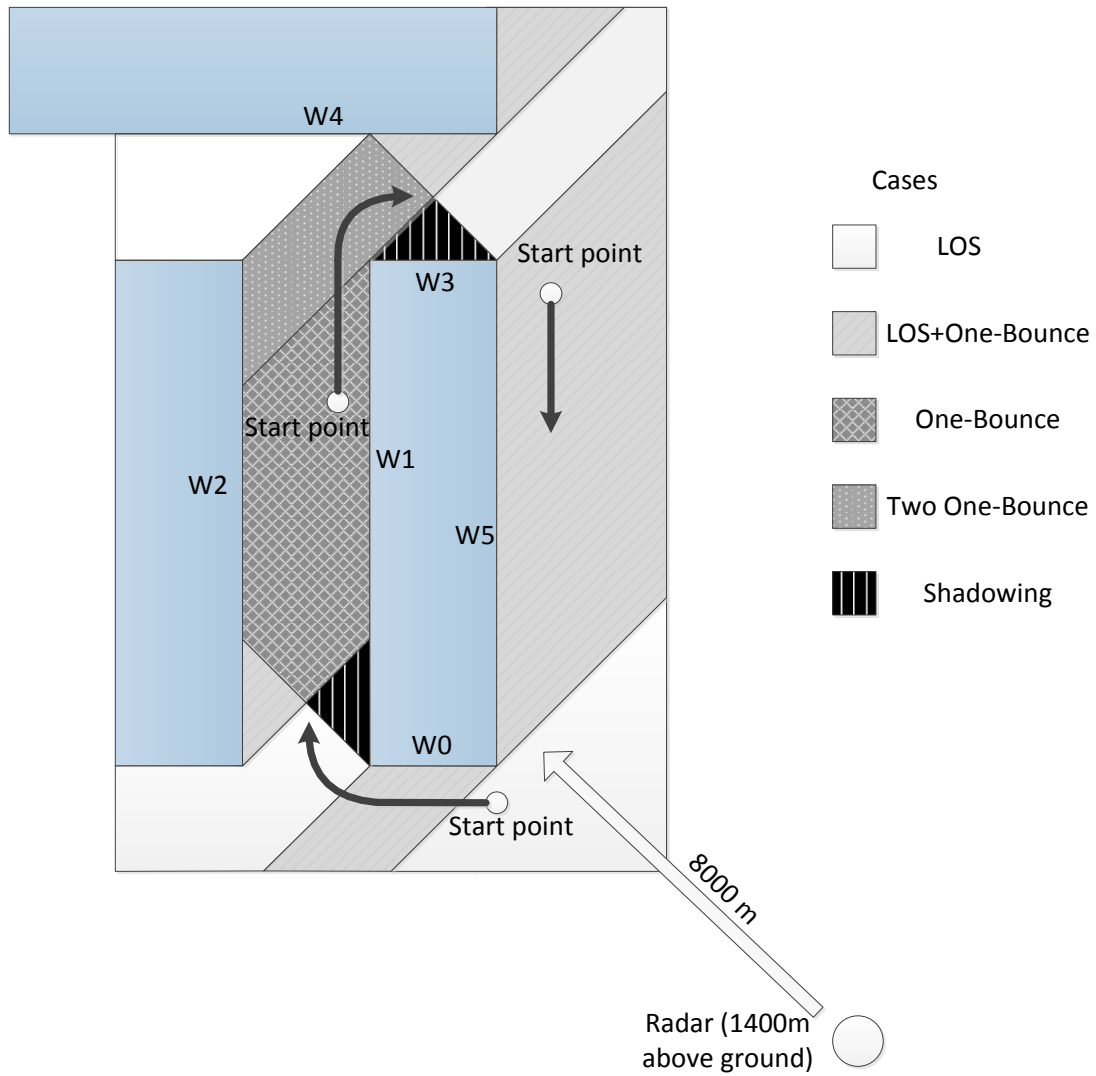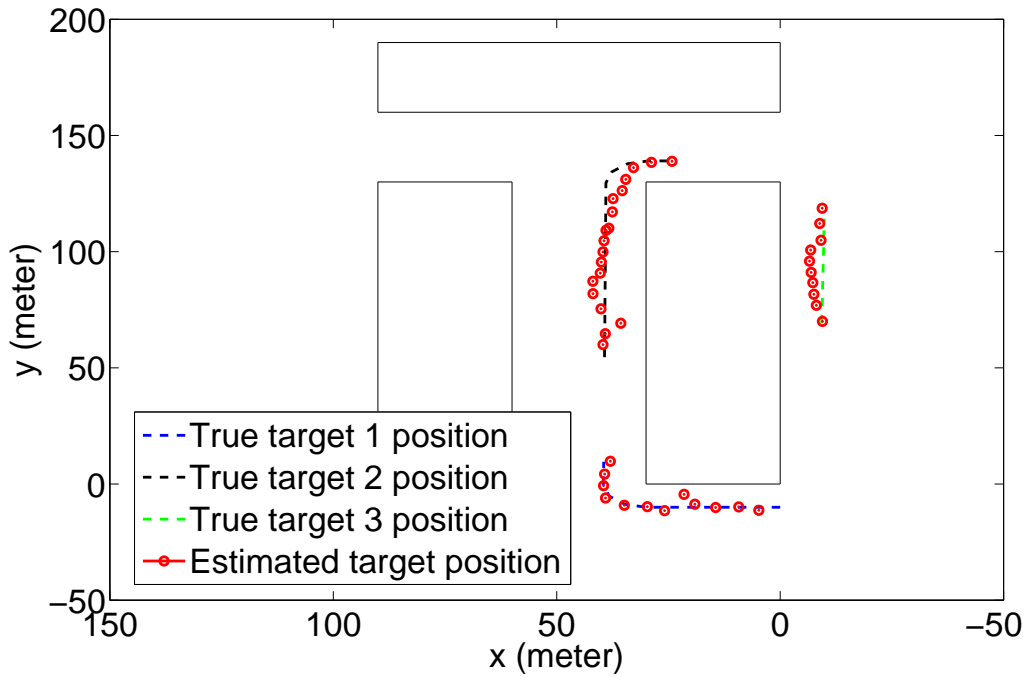**Figure 4.12:** Time-Varying Number of Targets Moving in The Same Direction (Max 4).

Figure 4.13: Time-Varying Number of Targets Moving in The Same Direction (Max 4): 2-D True and Estimated Trajectories.
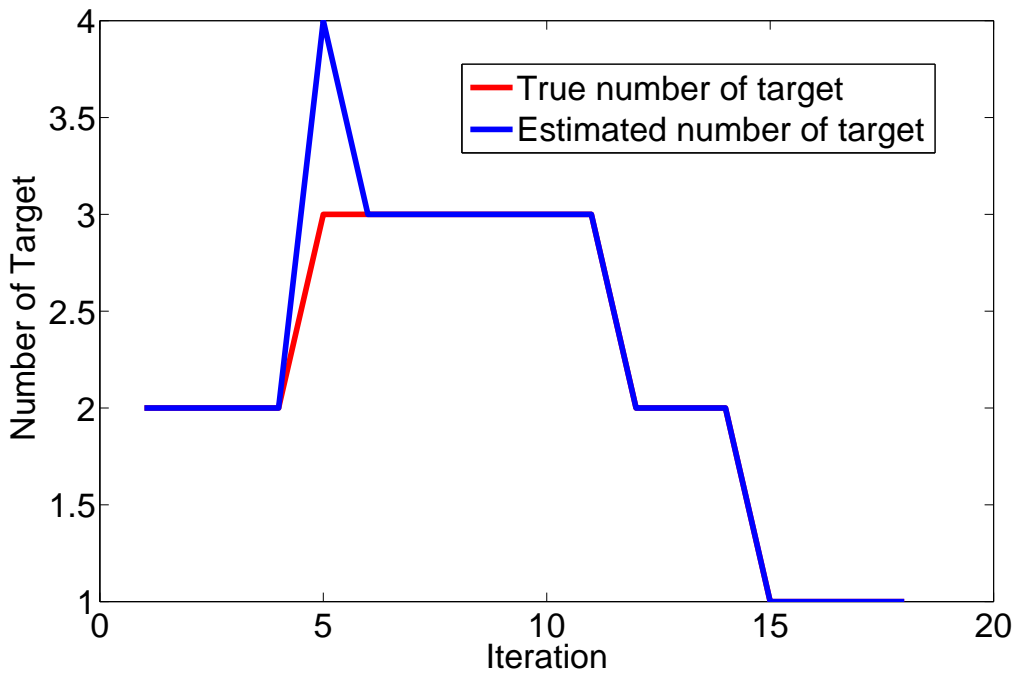

Figure 4.14: Time-Varying Number of Targets Moving in The Same Direction (Max 4): Cardinality.
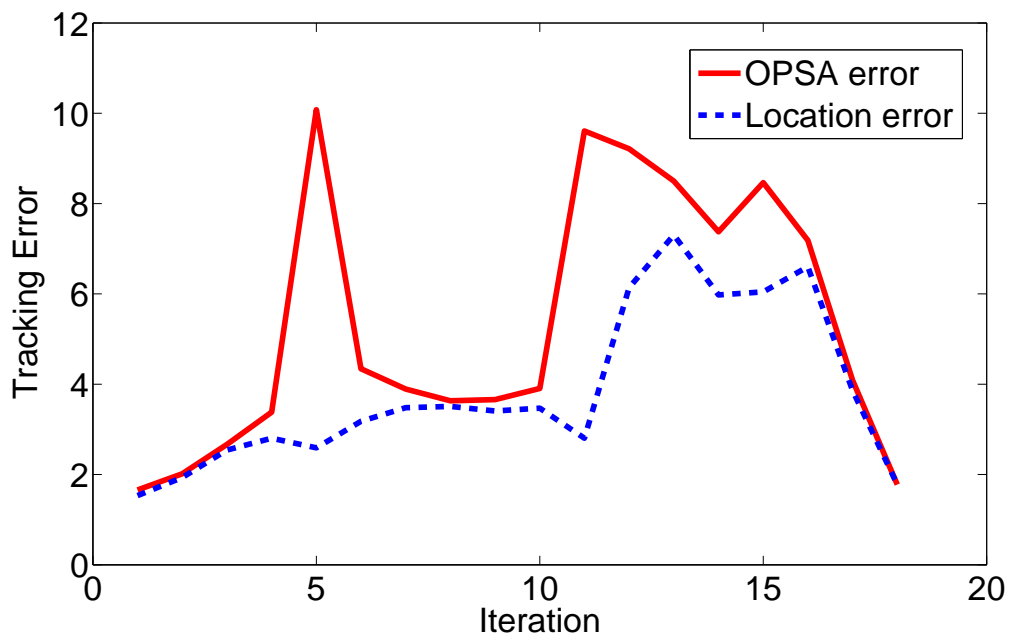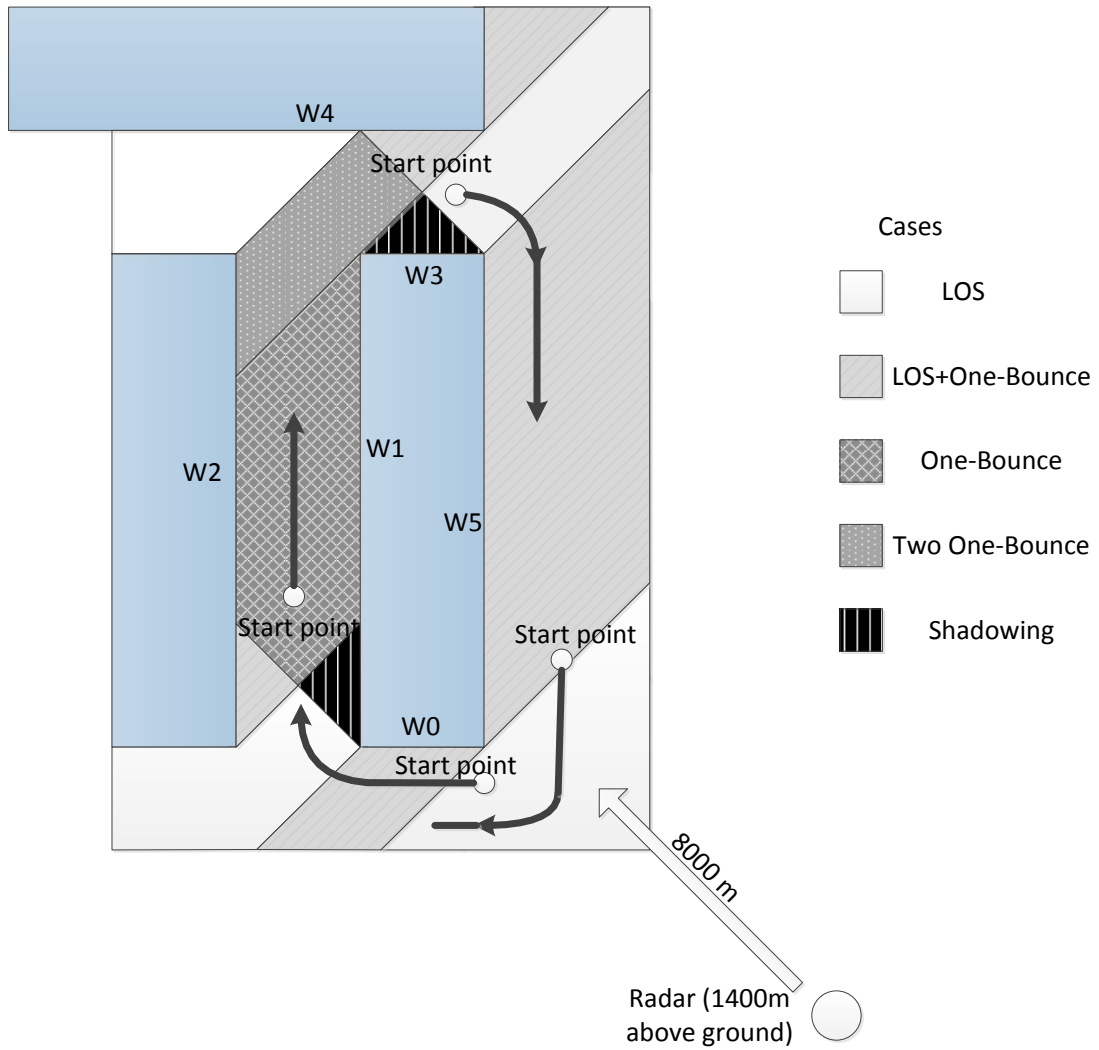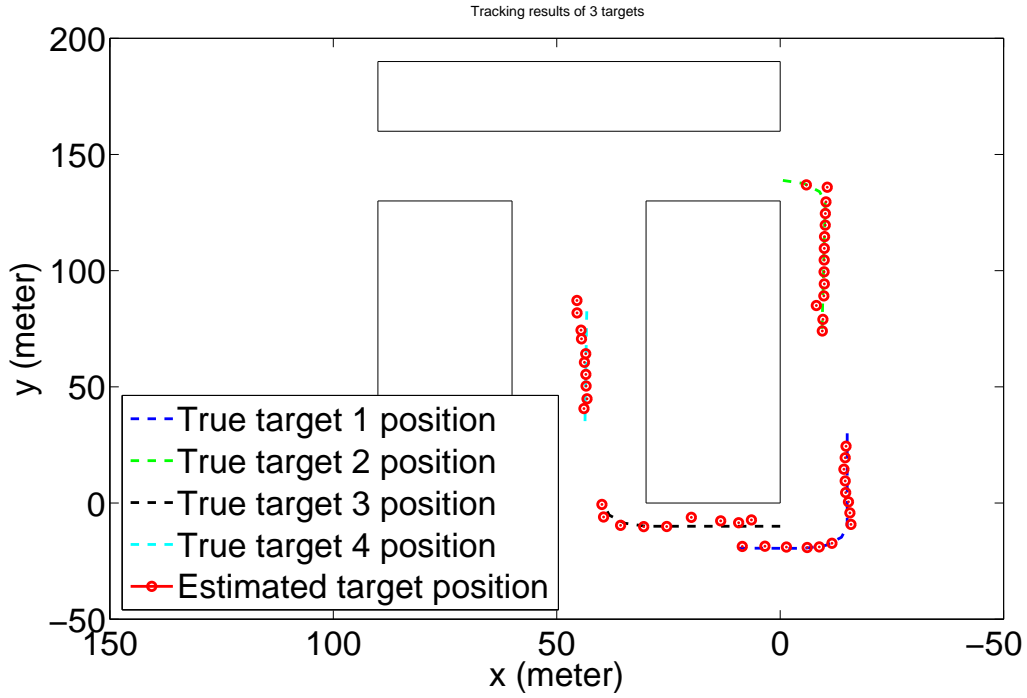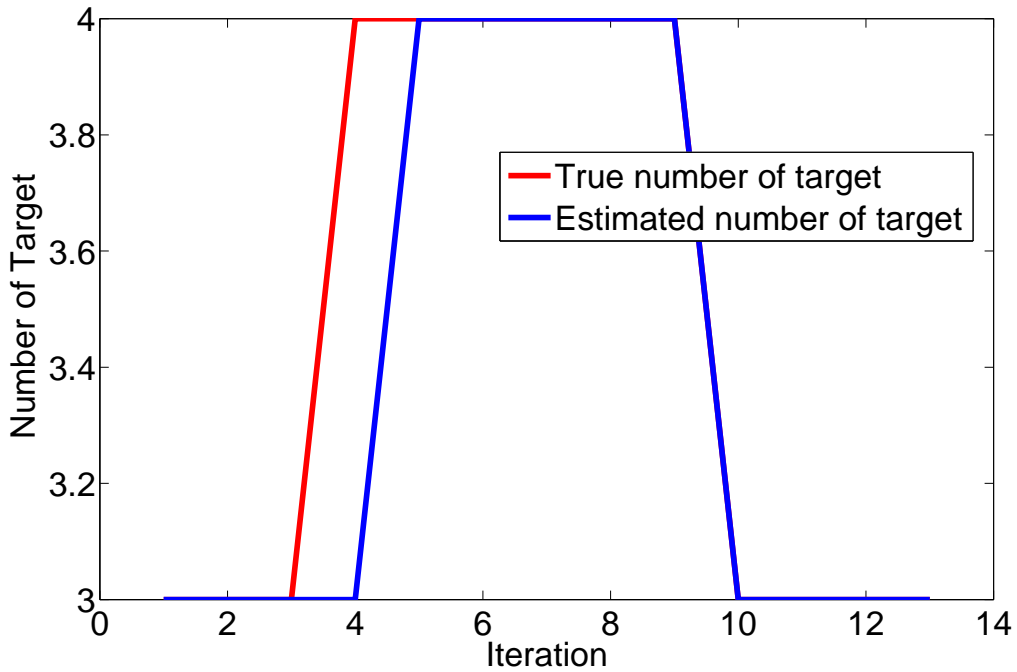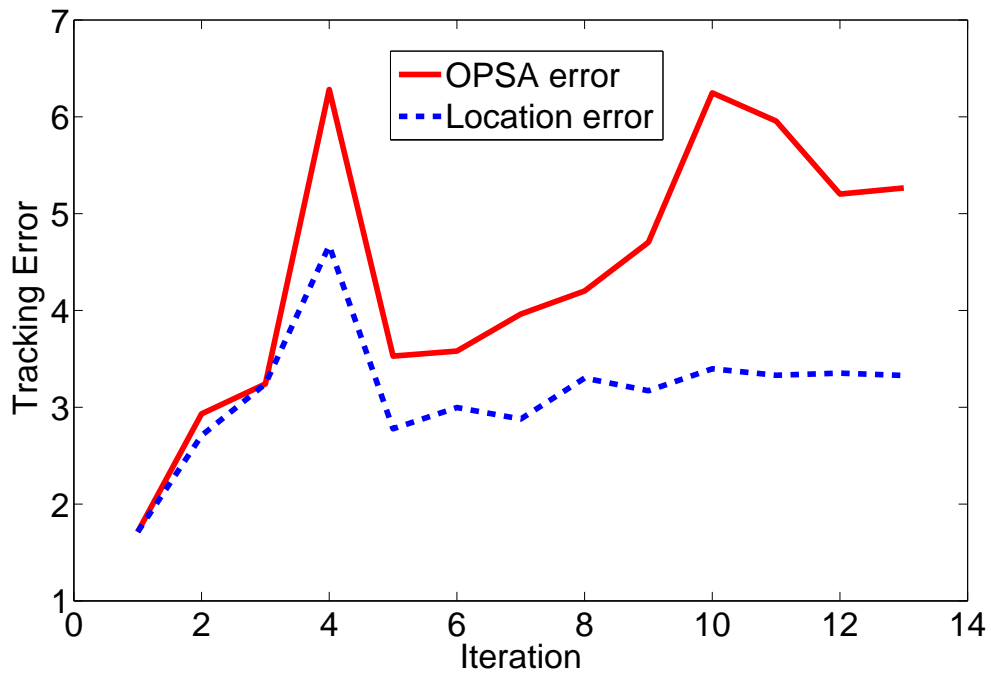
Figure 4.15: Time-Varying Number of Targets Moving in The Same Direction (Max 4): OSPA.

Chapter 5

UNDERWATER ACOUSTIC CHANNEL ESTIMATION

The underwater acoustic channel is highly time-varying, which makes the channel estimation a challenge process. When communicating using carrier frequencies in the medium-to-high frequency range, the Doppler scaling distortions caused by the wideband underwater acoustic channel make the estimation process even harder. Previously considered wideband underwater acoustic (UWA) channel estimation algorithms assume that the channel Doppler scale spread and time delay spread are known or they assume very large spreads. However, the UWA channel support in real applications is unknown and needs to be estimated. By assuming very large spreads, the estimation methods become more computationally complex and result in larger estimation errors. In this chapter, we first discuss two known wideband UWA channel estimation algorithms, the direct least-square (DLS) algorithm and the matching pursuit decomposition (MPD) algorithm and then we propose a new algorithm that is based on adaptive learning clustering methods.

5.1   Wideband UWA Channel Modeling

Most UWA signals are considered to have wideband properties due to the movement of scatterers in the channel causing Doppler scaling signal transformations. In many cases, the wideband Doppler scaling effect can be approximated by frequency shifts. However, this narrowband approximation only holds when underwater scatterers move slowly and when the transmitted signal bandwidth is much smaller than its central frequency. As wideband underwater acoustic signals with spectral components in the 300 to 20,000 Hz frequency range have bandwidths that are comparable

to their central frequencies, they are characterized by time delay and Doppler scale changes. The wideband linear time-varying channel model represents the channel output in terms of continuous time delay and Doppler scale change transformations on the transmitted signal, weighted by the wideband spreading function (WSF) coefficients as discussed in Section 3.2. Specifically, the noiseless received signal $y(t)$ can be represented as [47, 48]

$$y(t) = \int_0^{T_d} \int_{A_0}^{A_1} \chi(\tau, a) \sqrt{a} x(a(t - \tau)) da d\tau, \tag{5.1}$$

where τ and a are the continuous time delay and Doppler scale parameters, respectively, and $x(t)$ is the transmitted signal. The WSF, $\chi(\tau, a)$, represents the random phase change and attenuation of underwater scatterers corresponding to different values of τ and a. Due to path loss or velocity limit restrictions of realistic underwater acoustic channels, we assume that the WSF support regions are $\tau \in [0, T_d]$ and $a \in [A_0, A_1]$, where T_d is the channel's time delay spread, and the range of possible scaling values is given by $[A_0, A_1]$.

The discrete formulation of a wideband channel is obtained by geometrically sampling the scaling parameters using the Mellin transform [48] and by uniformly sampling the time delay parameters. The discrete time scale representation is given by

$$y(t) = \sum_{m=M_0}^{M_1} \sum_{n=0}^{N(m)} \chi_{n,m} \, a_d^{m/2} \, x\left(a_d^m t - \frac{n}{W}\right). \tag{5.2}$$

Here, $a_0 = \exp(1/\beta_0)$, β_0 is the Mellin support of $x(t)$, $A_d = A_1 - A_0$, $M_0 = \lfloor \ln A_0 / \ln a_0 \rfloor$, $M_1 = \lceil \ln A_1 / \ln a_0 \rceil$, $N(m) = \lceil a_0^m W T_d \rceil$ for integer m, and $\chi_{n,m}$ are the WSF coefficients. We assume that $T \gg T_d$ to ensure that there is no intersymbol interference, where T is the signal duration. Assuming independence between the scatterers contributing to the nth time delay and the mth scale path, then Equation (5.2) decom-

poses the overall channel into a total of

$$M = \sum_{m=M_0}^{M_1} (N(m) + 1)$$

independent, flat-fading channels. This results in a potential joint multipath-scale diversity of order M [48].

The block diagram for the wideband UWA channel can be seen in Figure 5.1.
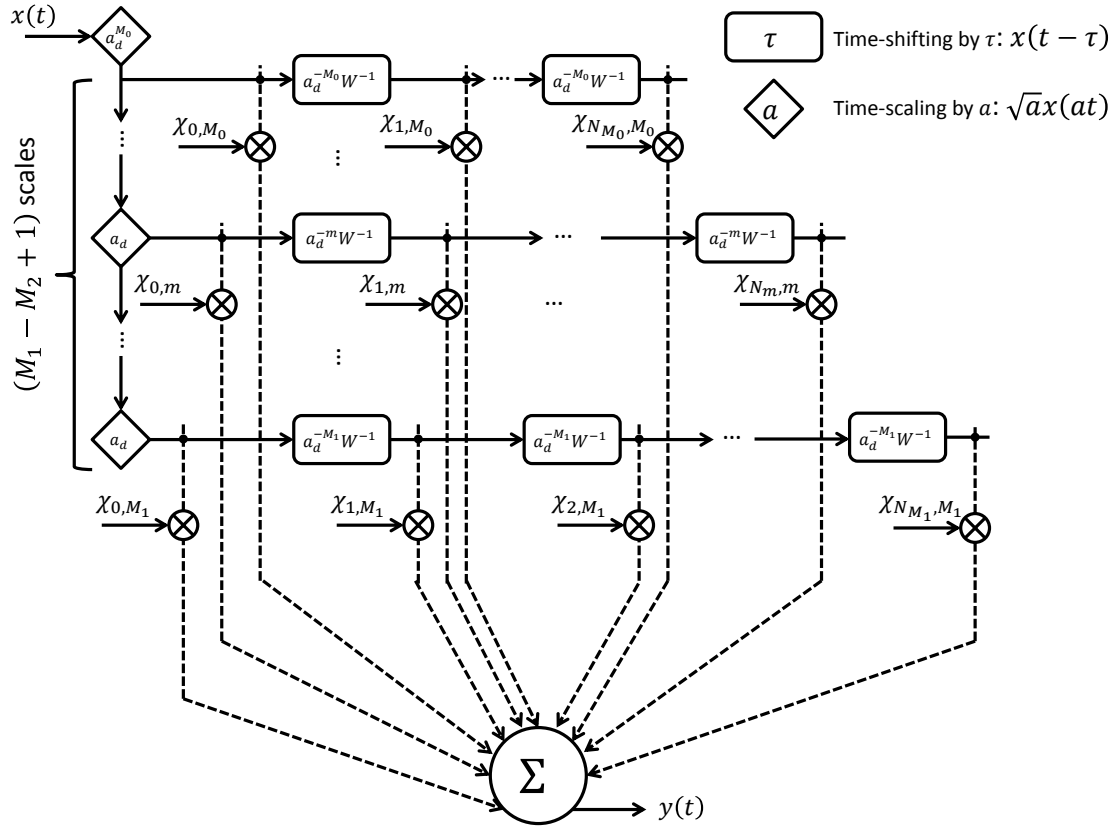

Figure 5.1: Block Diagram for Wideband UWA Channel Model.

5.2 Existing Methods of Wideband UWA Channel Estimation

In order to estimate the WSF coefficients in (5.2), two methods were considered in [47]. The first method is direct least-square (DLS) algorithm and the second method uses the matching pursuit decomposition (MPD) time-frequency based algorithm.

The DLS algorithm first forms a data matrix that contains the time-shifted and Doppler scaled versions of the transmitted signal, then it uses the pseudo inverse of the matrix to obtain the estimated WSF coefficients [47]. In [47], it is assumed that the channel support is known in order to form the data matrix. The MPD algorithm is used as an alternative to the DLS method and works best when the UWA channel is sparse, and when the channel support is assumed unknown. The MPD method forms a large dictionary that contains all possible time-shifted and Doppler scaled components of the transmitted signal. It then iteratively correlates the received signal with dictionary components in order to extract the time-scale paths of the channel. The weight factors of the MPD expansion provide estimates for the WSF coefficients. Our objective is to propose a new channel estimation algorithm that integrates the DLS and MPD algorithms with adaptive learning clustering methods in order to estimate both the UWA channel support as well as the WSF coefficients.

5.2.1   Direct Least-Square Estimation

DLS with Known Channel Support   Using the discrete time-scale channel representation in (5.2), we can estimate the WSF coefficients $\chi_{n,m}$ using a least-squares estimation approach. Specifically, when the received signal $y(t)$ is obtained, it is first sampled using sampling period T_s to form L samples of the $L \times 1$ received signal vector $\mathbf{y}$. In [47], it is assumed that the UWA channel support in term of M_0 and M_1 in (5.2) is known. Assuming that the transmit signal is also sampled using T_s to obtain the samples $x[\ell] = x(\ell T_s)$, $\ell = 0, \ldots, L - 1$, then we denote the time-shifted and scaled version of the ℓth sample by $\xi_{n,m,\ell} = a_d^{m/2} x(a_d^m k T_s - n/W)$. Using $\xi n, m, \ell$, we first define the $L \times 1$ data column vector $\boldsymbol{\phi}_[n, m] = [\xi_{n,m,0} \xi_{n,m,1} \cdots \xi_{n,m,L-1}]^T$ and then use the data vector to form the data matrix

$$\mathbf{D} = [\boldsymbol{\phi}_{0,M_0} \, \boldsymbol{\phi}_{1,M_0} \cdots \boldsymbol{\phi}_{N(M_0),M_0} \, \boldsymbol{\phi}_{0,M_0+1} \cdots \boldsymbol{\phi}_{N(M_0+1),M_0+1} \cdots \boldsymbol{\phi}_{0,M_1} \cdots \boldsymbol{\phi}_{N(M_1),M_1}]^T.$$

The data matrix is an $L \times M$ matrix, where L is the number of data samples and $M = sum_{m=M_0}^{M_1} N(m) + 1$. Furthermore, we concatenate the WSF coefficients $\chi_{n,m}$ to form the $M \times 1$ WSF coefficient vector

$$\boldsymbol{\Phi} = \begin{bmatrix} \chi_{0,M_0} \chi_{1,M_0} \cdots \chi_{N(M_0),M_0} \chi_{0,M_0+1} \cdots \chi_{N(M_0+1),M_0+1} \cdots \chi_{0,M_1} \cdots \chi_{N(M_1),M_1} \end{bmatrix}^T.$$

Then the matrix form of (5.2) can be written as

$$\mathbf{y} = \mathbf{D}\boldsymbol{\Phi}.$$

Using the least-squares method to obtain an estimate of $\boldsymbol{\Phi}$ results in

$$\hat{\boldsymbol{\Phi}} = (\mathbf{D}^T\mathbf{D})^{-1}\mathbf{D}^T\mathbf{y}.$$

DLS with Unknown Channel Support   We extend the DLS algorithm for channels with unknown support. When the channel support information M_0 and M_1 in (5.2) is unknown, the data matrix is created such that $m \in [M_{min}, M_{max}]$, where M_{min} and M_{max} are selected so as to guarantee $[M_0, M_1] \subseteq [M_{min}, M_{max}]$. For this case, the data matrix $\mathbf{D}$ can be written as

$$\mathbf{D} = \begin{bmatrix} \phi_{0,M_{min}} \cdots \phi_{N(M_{min}),M_{min}} \cdots \phi_{0,M_{max}} \cdots \phi_{N(M_{max}),M_{max}} \end{bmatrix}^T.$$

Accordingly, we concatenate the WSF coefficients $\chi_{n,m}$ to form the WSF coefficient vector

$$\boldsymbol{\Phi} = \begin{bmatrix} \chi_{0,M_{min}} \cdots \chi_{N_{M_{min}},M_{min}} \cdots \chi_{0,M_{max}} \cdots \chi_{N_{M_{max}},M_{max}} \end{bmatrix}^T.$$

The corresponding least-squares solution is then given by (5.3), using the newly defined $\mathbf{D}$ and $\boldsymbol{\Phi}$.

Note that, in this case, the dimension of the estimated WSF coefficients vector is far greater than the correct dimension, and a thresholding process can be applied to filter out the WSF coefficients with negligible weights.

5.2.2 MPD Estimation Wideband Channel

The WSF coefficients can also be estimated using he MPD time-frequency based method. The MPD first constructs a dictionary of time-scaled versions of the transmitted signal, assuming that the channel support is known and then it iteratively expands the received signal into a linear weighted combination of dictionary selected signals. Originally, the MPD was proposed to expand any finite energy signal into a linear combination of time-shifted and frequency-shifted Gaussian functions [80]. In [81], the MPD is used with dictionaries consisting of different signal transformations in the time-frequency plane, provides that the transformations are complete. When applying the MPD to the WSF coefficient estimation problem, the dictionary signals need to match the wideband signal transformations of time shifts and Doppler scale changes so that the MPD weights result in the estimated WSF coefficients.

Equation (5.2) can be rewritten as

$$y(t) = \sum_{u=0}^{L-1} \alpha_u g_u(t) + y_L^{\text{res}}(t),$$

where $g_u(t)$ is the selected dictionary signal at the uth iteration, and α_u is the corresponding weight coefficient. After L MPD iterations, the residue signal is denoted as y_L^{res}. The dictionary signals $g_{(n,m)}(t)$ are designed to match the time-shifted and Doppler scaled version of the transmitted signal $x(t)$, and are thus given by

$$g_{(n,m)}(t) = a_d^{m/2} x(a_d^m t - \frac{n}{W}).$$

At the initial stage of the MPD method, $y_0^{\text{res}}(t)$ is set to be the received signal $y(t)$. Then at the uth iteration, MPD computes the projection of the residue $y_u^{\text{res}}(t)$ onto every dictionary signal $g_{(n,m)}(t)$, and $g_u(t)$ is selected such that the magnitude of the projection is maximized. Its corresponding MPD coefficient is given by

$$\alpha_u = < y_u^{\text{res}}(t), g_u(t) > = \int_{t \in T_d} y_u^{\text{res}}(t) g_u^*(t) dt.$$

The residue for the $(u + 1)$th iteration can be calculated from the previous iteration
as

$$y_{u+1}^{\text{res}}(t) = y_u^{\text{res}}(t) - \alpha_u g_u(t).$$

The MPD decomposed signal consists of M selected time-scaled signals if the channel
support is known, then the dictionary is designed to be very large in order to ensure
that it includes the actual time-scale paths.

Note that, as the MPD is an iterative method, if M is large and most coefficients
are non-zero, then it is very computationally intensive. For this reason, the MPD
method is best suited to estimating sparse wideband channels with known support.

5.3   Channel Estimation Using Clustering Methods

The aforementioned DLS and MPD algorithms have shown promising performance
in [47], however they either assume a known channel support or they use either a
large data matrix or a large dictionary. In this section, we propose a new channel
estimation algorithm, which can estimate both the channel support as well as the
WSF coefficients.

5.3.1   UWA Channel Feature Extraction

In (5.2), the channel is modeled as a double summation of time-delay and Dopple
scale values, and it can be re-written as

$$y(t) = \sum_{m=M_0}^{M_1} \sum_{n=0}^{N(m)} \psi_{n,m}(t), \tag{5.3}$$

where $\psi_{n,m}(t) = \chi_{n,m} \, a_d^{m/2} \, x\left(a_d^m \, t - \frac{n}{W}\right)$ is a time shifted and Doppler scaled version
of the transmitted signal weighted by the corresponding WSF coefficient $\chi_{n,m}$. We
define $\psi_{n,m}(t)$ as the n, mth signal path for any combination of m and n within the

channel support. It can be seen from (5.3), the noiseless received signal $y(t)$ is a combination of M signal paths, and each signal path is uniquely characterized by the parameters $(m, n, \chi_{n,m})$, where m is the Doppler scale, n is the time shift, and $\chi_{n,m}$ is the corresponding WSF coefficient. Following the MPD concept, the UWA channel estimation can also be viewed as a feature extraction process. Specifically, we can consider that, the DLS and MPD channel estimation algorithms are extracting channel features from the received signal. Examples of extracted channel features can be seen in Figure 5.2 to 5.4

Figure 5.2: Estimated Channel Features Using Direct Least Square Algorithm with Known Channel Support

In Figure 5.2, the channel features are extracted using DLS algorithm with known channel support, and the noise is assumed to be additive white Gaussian noise (AWGN) with 20 dB signal-to-noise ratio (SNR). In Figure 5.3, the channel features are extracted using DLS algorithm with unknown channel support, thus a large data matrix is created. In Figure 5.4, the channel features are extracted using the MPD algorithm with a large dictionary. As it can be seen, when the channel support is unknown, the feature extraction performance for both the DLS and MPD methods
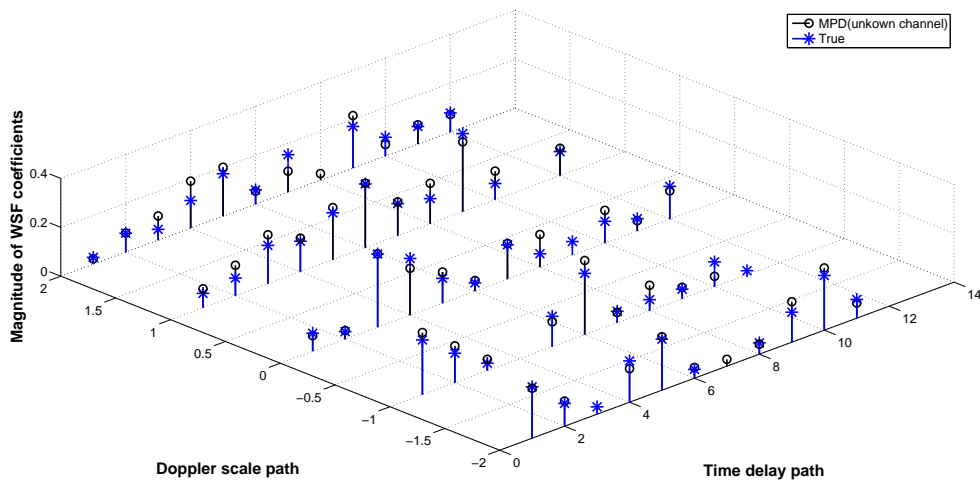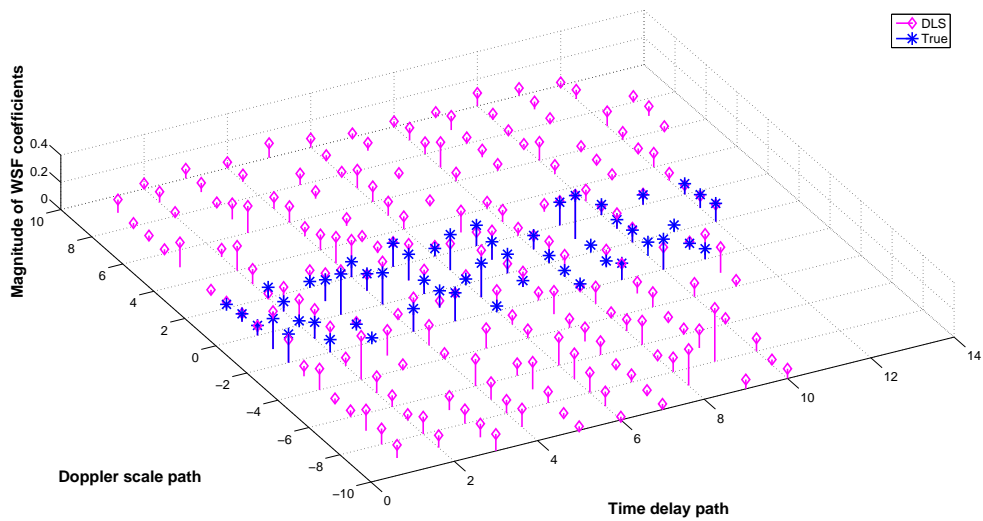
Figure 5.3: Estimated Channel Features Using Direct Least Square Algorithm with Unknown Channel Support
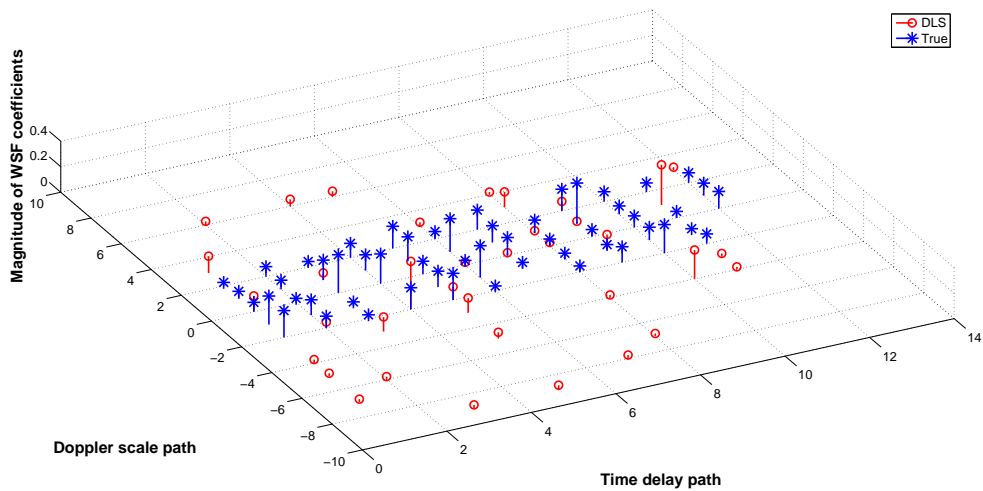

Figure 5.4: Estimated Channel Features Using MPD Algorithm with Unknown Channel Support

decreases. When the channel support is known, the DLS can successfully extract the channel features. However, when the channel support is unknown, the DLS results in the worse performance than the MPD.

5.3.2   UWA Channel Features Clustering

In order to improve the Doppler scale path estimation performance, and thus generate the data matrix in the DLS method more accurately, we propose to use the Dirichlet process Gaussian mixture model (DP-GMM) clustering algorithm [82–85]. Note that DP-GMM clustering has been used in many applications including structure health monitoring and disease classification [82–85], and it wa shown to successfully cluster data without knowledge of the total number of clusters.

Assume that a single UWA channel feature can be denoted as $\mathbf{x} = [m \, n \, \chi_{n,m}]^T$, then a mixture model is described by the probability density function (pdf)

$$p(\mathbf{x}|\boldsymbol{\theta}_1, \ldots, \boldsymbol{\theta}_B) = \sum_{b=1}^{B} w_b \, p(\mathbf{x}; \boldsymbol{\theta}_b) \,, \tag{5.4}$$

where $w_1, \ldots, w_B$ are the weights of individual mixture component, $\boldsymbol{\theta}_b$ is the parameter space representing the PDF $p(\mathbf{x}; \boldsymbol{\theta}_b)$, and B is the total number of mixture components [86]. We aim to estimate the parameters B, w_b, and $\boldsymbol{\theta}_b$, $b = 1, \ldots, B$ that best fit the extracted channel features.

The DP-GMM starts with an infinite number of mixture components and weighting factors [87], and it adaptively estimates the cluster model parameters without requiring any training [88]. Also, the $p(\mathbf{x}; \boldsymbol{\theta}_b)$ is assumed to be a Gaussian PDF with mean and covariance $\boldsymbol{\theta}_b = [\boldsymbol{\mu}_m \boldsymbol{\Sigma}_m]^T$. Therefore, the mixture model in (5.4) can be re-written as a summation of Gaussian distributions given by:

$$p(\mathbf{x}|\mathbf{w}, \boldsymbol{\mu}, \boldsymbol{\Sigma}) = \sum_{b=1}^{B} w_b \, \mathcal{N}(\mathbf{x}; \boldsymbol{\mu}_m, \boldsymbol{\Sigma}_m) \,, \tag{5.5}$$

The notation $N(\mathbf{x}; \boldsymbol{\mu}, \boldsymbol{\Sigma})$ denotes the Gaussian pdf of $\mathbf{x}$ with mean vector $\boldsymbol{\mu}$ and covariance matrix $\boldsymbol{\Sigma}$.

In a Bayesian sense, a prior PDF must be selected in order to determine the nonparametric statistics related to a dataset. The Dirichlet process (DP) G is a prior that is fully characterized by a base distribution, G_0, and an innovation parameter α [86]. The innovation parameter characterizes how likely a new data point is to be placed within an existing cluster or in a new cluster. Consider the distribution [89]:

$$G \sim \mathrm{DP}(\alpha, G_0), \tag{5.6}$$

$$\boldsymbol{\theta}_j | G \sim G \quad j = 1, \ldots, J, \tag{5.7}$$

that is drawn from a DP with innovation parameter α and base distribution G_0 with $\{\boldsymbol{\theta}_1, \ldots, \boldsymbol{\theta}_J\}$. Then, G_0 is the expected value of G and α characterizes how close G is to G_0. In particular, G is discrete and has the following representation [90]:

$$\boldsymbol{\theta}_b \sim G_0 \quad b = 1, \ldots, \infty,$$

$$w_b = v_b \prod_{i=1}^{b-1} (1 - v_k), \quad b = 1, \ldots, \infty,$$

where

$$v_k \sim \mathrm{Beta}\,(1, \alpha), \quad k = 1, \ldots, \infty,$$

$$G(\boldsymbol{\theta}) = \sum_{b=1}^{\infty} w_b\, \delta(\theta - \theta_b). \tag{5.8}$$

and $\delta(\cdot)$ is the Kronecker delta function.

In [90], the DP process is viewed as a stick-breaking process, in which case, a unit length stick may be broken such that the size of each successive break is representative of $w_b = \mathrm{Pr}(\boldsymbol{\theta} = \boldsymbol{\theta}_b)$, where $\mathrm{Pr}(\cdot)$ denotes probability.

For each $\boldsymbol{\theta}_j$, it is possible to integrate out G, this is described by the Pólya urn relation [88, 91–94]:

$$p(\boldsymbol{\theta}_j|\boldsymbol{\Theta}^{(-j)}, \alpha, G_0) = \frac{1}{\alpha + J - 1} \sum_{\substack{j'=1 \\ j' \neq j}}^{J} \delta(\boldsymbol{\theta}_j - \boldsymbol{\theta}_b) + \frac{\alpha}{\alpha + J - 1} G_0(\boldsymbol{\theta}_j), \tag{5.9}$$

where $\boldsymbol{\Theta}^{(-j)}$ are the parameters except for $\boldsymbol{\theta}_j$, and $N_b^{(-j)}$ is the number of variables in $\boldsymbol{\Theta}^{(-j)}$ that are equal to $\boldsymbol{\theta}_b$. Equation (5.9) can also be rewritten as:

$$p(\boldsymbol{\theta}_j|\boldsymbol{\Theta}^{(-j)}, \alpha, G_0) = \frac{1}{\alpha + J - 1} \sum_{b=1}^{B} N_b^{(-j)} \delta(\boldsymbol{\theta}_j - \boldsymbol{\theta}_b) + \frac{\alpha}{\alpha + J - 1} G_0(\boldsymbol{\theta}_j). \tag{5.10}$$

When we need to cluster a new data point, the probability of choosing an existing cluster is $\Pr(\boldsymbol{\theta}_b = \boldsymbol{\theta}_j) = N_b^{(-j)}/(\alpha + J - 1)$, and the probability of creating a new cluster is $\Pr(\boldsymbol{\theta}_b \neq \boldsymbol{\theta}_j) = \alpha/(\alpha + J - 1)$. This then leads to the DP-GMM representation as described in Equation (5.5) whose corresponding stick-breaking process representation is given as:

$$\boldsymbol{\theta}_b \sim G_0, \quad b = 1, \ldots, \infty, \tag{5.11}$$

$$v_k \sim \text{Beta}(1, \alpha), \quad k = 1, \ldots, \infty, \tag{5.12}$$

$$w_b = v_b \prod_{k=1}^{b-1} (1 - v_k), \quad b = 1, \ldots, \infty, \tag{5.13}$$

$$c_j|\mathbf{w} \sim \text{Categorical}(\mathbf{w}), \quad j = 1, \ldots, J, \tag{5.14}$$

$$\mathbf{x}_j|c_j \sim p(x_j|\boldsymbol{\theta}_{c_j}), j = 1, \ldots, J. \tag{5.15}$$

The variable c_j indicates which of the B possible clusters includes $\mathbf{x}_j$ and categorical refers to the assignment to one of the B possible clusters.

Although the DP-GMM does not require knowledge of the maximum number of clusters, we provide as an upper limit the maximum possible scale spread given by $(M_{max} - M_{min})$. Furthermore, the blocked Gibbs sampler algorithm is used to simplify the calculation, which iteratively estimates posterior distribution parameters [95]. Considering the mixture model given in Equation (5.4) and using the notation in Equation (5.11)-(5.15), the ith iteration of blocked Gibbs sampler can be written as [95, 96]:

$$\boldsymbol{\theta}_b^{(i)} \sim p(\boldsymbol{\theta}_b | \mathbf{c}^{(i-1)}, \mathbf{x}_j), \quad b = 1, \ldots, B, \tag{5.16}$$

$$c_j^{(i)} \sim p(c_j | \boldsymbol{\Theta}^{(i)}, \mathbf{w}^{(i-1)}, \mathbf{x}_j), \quad j = 1, \ldots, J, \tag{5.17}$$

$$w_b^{(i)} \sim p(w_b | \mathbf{c}^{(i)}), \quad b = 1, \ldots, B. \tag{5.18}$$

According to the properties of conjugate prior [96]:

$$p(\boldsymbol{\theta}_b | \mathbf{c}, \mathbf{x}_j) \propto G_0(\boldsymbol{\theta}_b) \prod_{j:c_j=b} p(\mathbf{x}_j | \boldsymbol{\theta}), \quad b = 1, \ldots, B, \tag{5.19}$$

$$p(c_j | \boldsymbol{\Theta}, \mathbf{w}, \mathbf{x}_j) = \sum_{b=1}^{B} \left(w_b \, p(\mathbf{x}_j | \boldsymbol{\theta}_b) \right) \delta(c_j - b), \quad j = 1, \ldots, J, \tag{5.20}$$

$$p(w_b | \mathbf{c}) = v_b \prod_{k=1}^{b-1} (1 - v_k), \quad b = 1, \ldots, B, \tag{5.21}$$

where v_b is also defined as:

$$v_b \sim \text{Beta} \left(1 + N_b^*, \alpha + \sum_{b'=b+1}^{B} N_{m'}^* \right), \tag{5.22}$$

and $j : c_j = b$ denotes the indices in $\mathbf{c}$ such that $c_n = b$, and N_b^* is the number of elements in $\mathbf{c}$ that are equal to b.

The likelihood distribution is Gaussian and the prior distribution, G_0 is Normal-Wishart. The Normal-Wishart PDF is used because this is the multidimensional generalization for the DP-GMM. Thus, the relationship between the prior and posterior distributions may be described by:

$$G_0(\boldsymbol{\theta}) \triangleq \mathcal{NW}(\boldsymbol{\mu}, \boldsymbol{\Sigma}^{-1}; \boldsymbol{\mu}_{\mathcal{N}}, \tau_{\mathcal{N}}, \xi_{\mathcal{W}}, \iota_{\mathcal{W}}), \tag{5.23}$$

$$p(\boldsymbol{\theta}|\mathbf{c}, \mathbf{X}) \triangleq \mathcal{NW}(\boldsymbol{\mu}, \boldsymbol{\Sigma}^{-1}; \tilde{\boldsymbol{\mu}}_{\mathcal{N}}, \tilde{\tau}_{\mathcal{N}}, \tilde{\xi}_{\mathcal{W}}, \tilde{\iota}_{\mathcal{W}}). \tag{5.24}$$

where $\mathcal{NW}(\cdot)$ denotes a Normal-Wishart pdf.

The hyperparameters $\boldsymbol{\mu}_{\mathcal{N}}, \tau_{\mathcal{N}}, \xi_{\mathcal{W}}, \iota_{\mathcal{W}}, \tilde{\boldsymbol{\mu}}_{\mathcal{N}}, \tilde{\tau}_{\mathcal{N}}, \tilde{\xi}_{\mathcal{W}}, \tilde{\iota}_{\mathcal{W}}$ are described by:

$$\tilde{\boldsymbol{\mu}}_{\mathcal{N}} = \frac{\tau_{\mathcal{N}} \boldsymbol{\mu}_{\mathcal{N}} + J \boldsymbol{\mu}_x}{\tau_{\mathcal{N}} + J}, \tag{5.25}$$

$$\tilde{\tau}_{\mathcal{N}} = \tau_{\mathcal{N}} + J, \tag{5.26}$$

$$\tilde{\iota}_{\mathcal{W}} = \iota_{\mathcal{W}} + \boldsymbol{\Sigma}_x + \frac{\tau_{\mathcal{N}} J}{\tau_{\mathcal{N}} + J}(\boldsymbol{\mu}_{\mathcal{N}} - \boldsymbol{\mu}_x)(\boldsymbol{\mu}_{\mathcal{N}} - \boldsymbol{\mu}_x)^T, \tag{5.27}$$

$$\tilde{\xi}_{\mathcal{W}} = \xi_{\mathcal{W}} + J, \tag{5.28}$$

and $\boldsymbol{\mu}_x$ and $\boldsymbol{\Sigma}_x$ are the mean and covariance of $\mathbf{X}$, and $\boldsymbol{\mu}_{\mathcal{N}}, \tilde{\tau}_{\mathcal{N}}, \tilde{\iota}_{\mathcal{W}}$, and $\tilde{\xi}_{\mathcal{W}}$ are user specified with the restrictions:

$$\tilde{\tau}_{\mathcal{N}} > 0, \tag{5.29}$$

$$\tilde{\xi}_{\mathcal{W}} > D - 1, \tag{5.30}$$

where D is the number of dimensions in $\mathbf{x}$.

We consider P channel features,

$$\mathbf{X} = \{\mathbf{x}_1, \mathbf{x}_2, \ldots, \mathbf{x}_P\}, \tag{5.31}$$

$[\{\mathbf{x}^{(l)}\}_{l=1}^{L}] = \text{RESAMPLE}[\{\mathbf{x}^{(p)}, w_p\}_{p=1}^{P}]$
Initialize the cumulate density function (CDF): $c_1 = 0$
FOR $p = 2 : P$
Construct CDF: $c_p = c_{p-1} + w_p$
END FOR
Let index u_1 be uniformly distributed between 0 and $1/L$
FOR $l = 1 : L$
Define: $u_l = u_1 + L^{-1}(l - 1)$
WHILE $u_l > c_p$
$p > p + 1$
END WHILE
CREATING TINY NOISE: $n \sim \mathcal{N}(0, \epsilon)$, ϵ is very small
Assign 2-D feature: $\mathbf{x}^{(l)} = \mathbf{x}^{(p)} + n$
END FOR

Table 1: Feature Resampling Algorithm

where the pth element $\mathbf{x}_p$ is represented by $[m_p\, n_p\, \chi_p]^T$.

As the WSF coefficients χ_p could be significantly non-Gaussian, the clustering is implemented only with respect to the Doppler scale (m_p) and time delay (n_p). In order to make use of the information from χ_p, a feature resampling process is implemented before the DP-GMM algorithm. In the new proposed approach, after the 3-D channel features are extracted, the WSF coefficients are used as the weights and the corresponding Doppler scale and time delay pairs are used as the new 2-D features. Then we can represent the 3-D channel features as 2-D features as $\mathbf{X} = \{\mathbf{x}^{(p)}, w_p\}_{p=1}^{P}$, where $\mathbf{x}^{(p)} = (m_p, n_p)$ and their corresponding weight $w_p = \chi_p$. The steps for computing the feature resampling process are provided in Table 1

Note that, L is the total number of 2-D features after resampling.

The DP-GMM algorithm is then used to cluster the resampled 2-D channel feature set. Assuming that the new features are given by $\mathbf{X}' = \{\mathbf{x}^{(l)}\}_{l=1}^{L}$, and the pdf of $\mathbf{X}'$

is given by

$$p(\mathbf{X}'|\mathbf{w}, \boldsymbol{\mu}, \boldsymbol{\Sigma}) = \sum_{b=1}^{B} w_b \, \mathcal{N}(\mathbf{X}'; \boldsymbol{\mu}_m, \boldsymbol{\Sigma}_m) \,, \tag{5.32}$$

where B is the estimated total number of clusters, w_b, and $\boldsymbol{\mu}_b$ and $\boldsymbol{\Sigma}_b$ are the weight, mean and covariance for the bth Gaussian pdf, respectively. When given a set of 2-D channel features, the DP-GMM outputs a total number of B estimated Doppler paths with values $\{m_b\}_{b=1}^{B}$, where m_b is extracted from $\boldsymbol{\mu}_b = [m_b, \, n_b]^T$.

5.3.3 Adaptive Estimation Algorithm

The new channel estimation algorithm is a combination of the aforementioned feature extraction process and feature clustering process. At the initialization stage, the initial 3-D channel features are extracted using the MPD method. As it can be seen from Figure 5.2-5.4, when the channel support is unknown, the MPD has a higher estimation performance than DLS. After the 3-D features have been extracted, the resampling process from Table 1 is used to obtain the 2-D channel feature set. The 2-D channel features are used as input to the DP-GMM algorithm to provide an initial estimate of the Doppler scale spread. The estimated initial channel spread is used to create the data matrix, and then the DLS approach is used to estimate the channel features/coefficients for use as refined channel features. These channel features are resampled and the DP-GMM algorithm is implemented again on the refined channel features to estimate the Doppler scale spread. Again, the refined channel support is used to generate a new data matrix, which is used by the DLS approach to estimate the channel features/coefficients. Finally, a thresholding process is implemented to eliminate any time-scale paths with very small WSF coefficients.

We show one real simulation example to demonstrate the comparison between DP-GMM clustering results using the initial channel features estimated by the MPD

and the refined channel features estimated by the DLS. Figure 5.5 shows the clustered Doppler paths by using the initial channel features estimated by the MPD algorithm. The x-coordinate is normalized time-shift in second and y-coordinate is normalized Doppler scale value. The black crossing points are the estimated channel features after resampling, and the red stars are the Gaussian centers. The true Doppler scale index paths are $m = [-2, -1, \ldots, 2]$, and the estimated Doppler scale index paths are $\tilde{m} = [-9, -6, -5, \ldots, 4, 6, 9]$.

Figure 5.6 shows the clustered Doppler path by using the refined channel features that were estimated by the DLS algorithm. The x-coordinate is normalized time-shift and y-coordinate is normalized Doppler scale. The black crossing points are the estimated channel features after resampling, and the red stars are the Gaussian centers. The estimated refined Doppler scale index paths are $\tilde{m} = [-3, -2, \ldots, 3]$. It can be seen that, due to the large initial channel feature extraction error, the initial Doppler scale index path estimation is poor, and by implementing the DP-GMM algorithm again on the refined channel features, the channel Doppler scale index path estimation improved.

The overall pseudo code of the new proposed algorithm can be see in Table 2

5.4   Simulation Results

In this section, we provide numerical simulations and results for wideband channel estimation. We show our simulation results for both wideband channel support and WSF coefficients estimation.

5.4.1   Threshholding Percentage

The UWA channel is firstly assumed to be fixed and the estimation performance is compared between DLS algorithm, MPD algorithm and adaptive clustering esti-
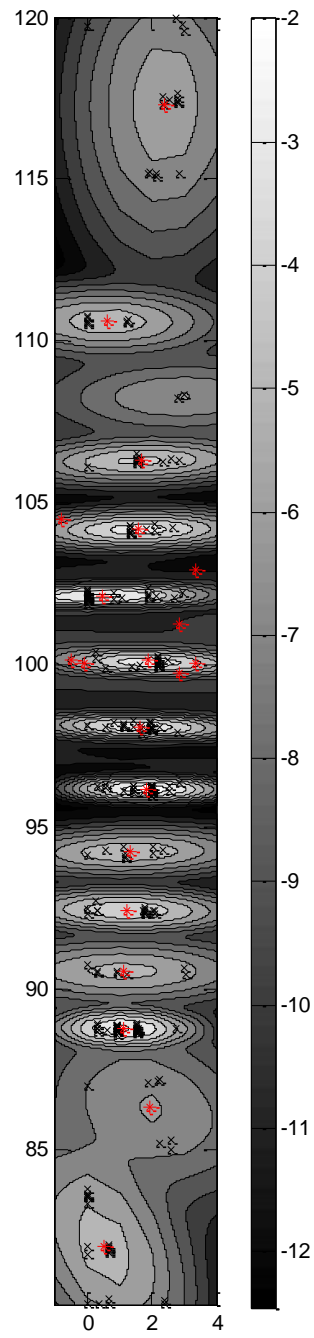
Figure 5.5: Doppler Path Information Estimated by Using DP-GMM from The Initial Channel Features.
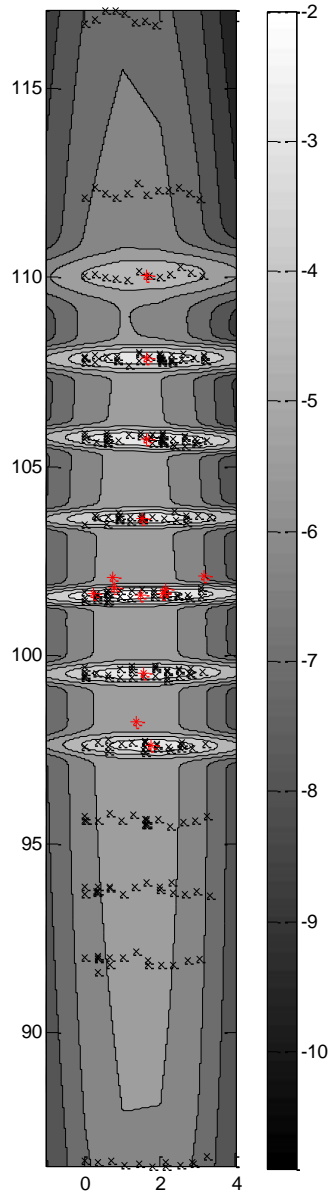
Figure 5.6: Doppler Path Information Estimated by Using DP-GMM from The Refined Channel Features.

Adaptive Channel Estimation Algorithm
Input: Received signal $y(t)$, transmitted signal $x(t)$, M_{min}, M_{max}
Output: Doppler path estimation $\{\tilde{M}_0, \tilde{M}_1\}$, WSF coefficients $\tilde{\chi}_{n,m}$

Initial stage: channel feature extraction using MPD

$$[\{m_p,\, n_p,\, \chi_p\}_{p=1}^{P}] = \mathrm{MPD}\,[\,y(t), x(t), M_{min}, M_{max}\,]$$

Resampling stage:

      Assign particle states and weights: $\{\mathbf{x}^{(p)}, w_p\}_{p=1}^{P} = \{m_p,\, n_p,\, \chi_p\}_{p=1}^{P}$

      Resample process: $[\{\mathbf{x}^{(l)}\}_{l=1}^{L}] = \mathrm{RESAMPLE}\,[\{\mathbf{x}^{(p)}, w_p\}_{p=1}^{P}]$

DP-GMM clustering stage:

      Obtain $[\{w_b, \boldsymbol{\mu}_b, \boldsymbol{\Sigma}_b\}_{b=1}^{B}]$ from $[\{\mathbf{x}^{(l)}\}_{l=1}^{L}]$

Initial channel support estimation:

      Extract $\{m_b\}_{b=1}^{B}$ from $\{\boldsymbol{\mu}_b\}_{b=1}^{B}$

Refine stage: channel feature extraction using direct least square

      Obtain $[\{m_p,\, n_p,\, \chi_p\}_{p=1}^{P'}]$ using DLS algorithm from $[y(t), x(t), \{m_b\}_{b=1}^{B}]$

Resampling stage:

      Assign particle states and weights: $\{\mathbf{x}^{(p)}, w_p\}_{p=1}^{P'} = \{m_p,\, n_p,\, \chi_p\}_{p=1}^{P'}$

      Resample process: $[\{\mathbf{x}^{(l)}\}_{l=1}^{L}] = \mathrm{RESAMPLE}\,[\{\mathbf{x}^{(p)}, w_p\}_{p=1}^{P'}]$

DP-GMM clustering stage:

      Obtain $[\{w_b, \boldsymbol{\mu}_b, \boldsymbol{\Sigma}_b\}_{b=1}^{B'}]$ from $[\{\mathbf{x}^{(l)}\}_{l=1}^{L}]$

      Extract $\{m_{b'}\}_{b'=1}^{B'}$ from $\{\boldsymbol{\mu}_{b'}\}_{b'=1}^{B'}$

Fianl channel estimation stage:

      Obtain $[\{m_p,\, n_p,\, \chi_p\}_{p=1}^{\hat{P}}]$ using DLS approach from $[y(t), s(t), \{m_{b'}\}_{b'=1}^{B'}]$

Thresholding stage:

      $\mathrm{Thr} = \max_{p=1,\ldots,\hat{P}} |\chi_p|/100$

For $p = 1 : \hat{P}$:

      If $\chi_p < \mathrm{Thr}$:

            Remove $\{m_p,\, n_p,\, \chi_p\}$ from channel feature set $\hat{\mathbf{X}} = [\{m_p,\, n_p,\, \chi_p\}_{p=1}^{\hat{P}}]$

      End If

End For

Final estimated channel Doppler support: $\hat{M}_0 = \min_{m_p \in \hat{\mathbf{X}}} m_p$, and $\hat{M}_1 = \max_{m_p \in \hat{\mathbf{X}}} m_p$

Table 2: Adaptive Channel Estimation Algorithm

mation (ACE) algorithm. We consider two cases. In Case 1, the channel the WSF coefficients are all uniform. In Case 2, the WSF coefficients are drawn from a Gaussian distribution.

Case 1

Figure 5.7 shows the UWA wideband channel true coefficients. It can be seen that the true Doppler support of the channel is $m = [-2, -1, \ldots, 2]$, and all the coefficients have the same magnitude. The SNR is fixed to 20 dB.
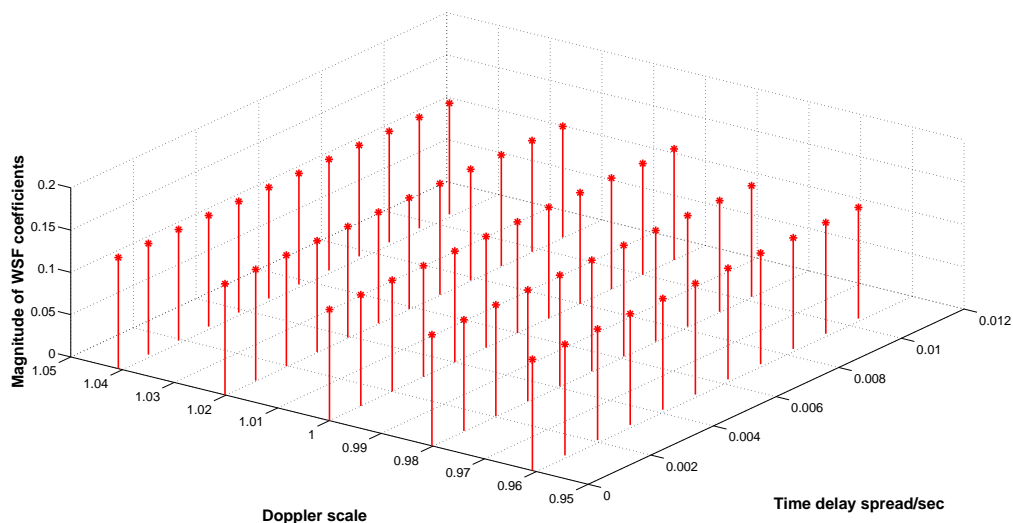

Figure 5.7: True WSF Coefficients for Fixed Channel Scenario Simulation: Case 1.

Figure 5.8 and Figure 5.9 present the simulation results using 1% and 10% thresholding. Note that, 1% thresholding means that the threshold is chosen to be 1% of the maximum value of the estimated WSF coefficients, the WSF coefficients whose values are less than the the threshold are discard.

The Doppler scale estimations are compared between all three algorithms, the purple diamond represents the average estimation result for the DLS algorithm, the red square represents the average estimation result for the MPD algorithm, the green
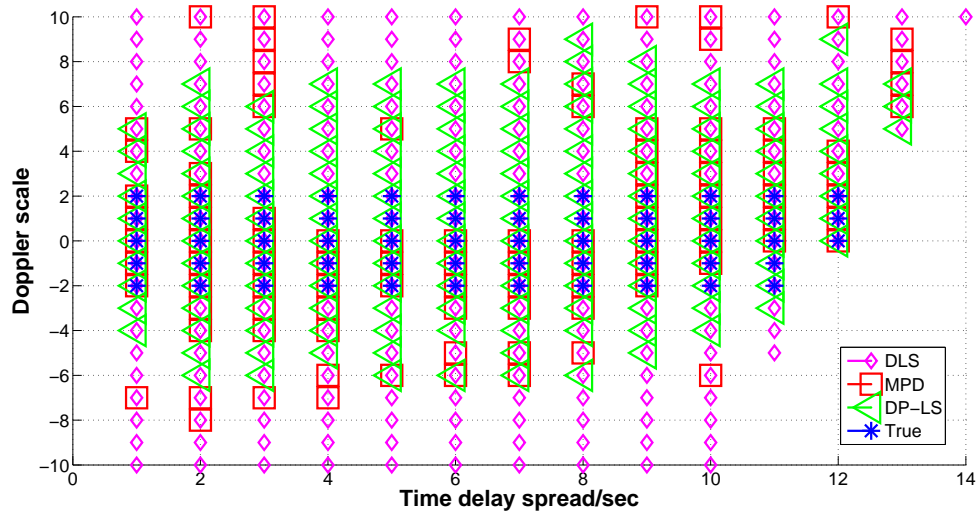
Figure 5.8: Estimated Channel Support with 1% Thresholding Process: Case 1.
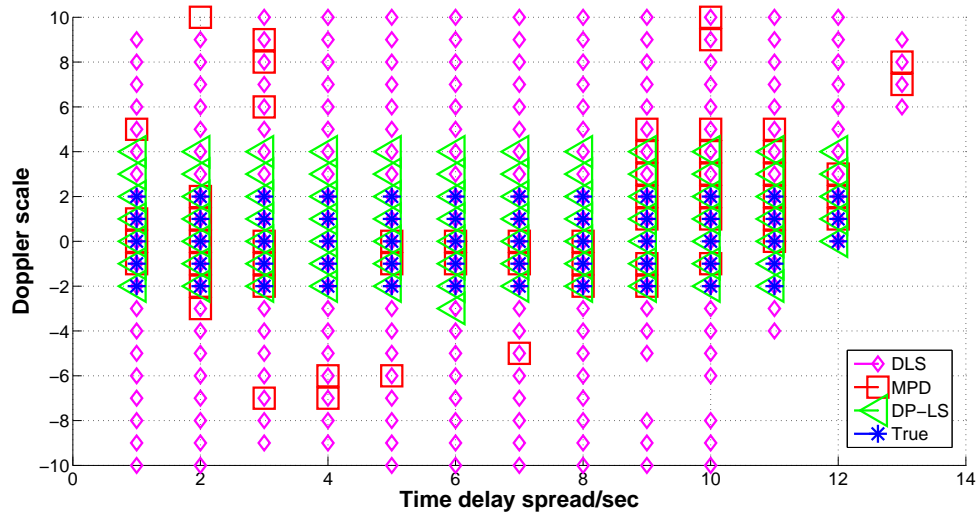

Figure 5.9: Estimated Channel Support with 10% Thresholding Process: Case 1.

triangular represents the average estimation result for the ACE algorithm, and the blue star represents the true channel coefficients. It can be seen that the ACE algorithm outperforms the other two algorithms. It can also be seen that as the threshold value increases, the number of false alarms decreases.

Case 2

Figure 5.10 shows the UWA wideband channel true coefficients. It can be seen that the true Doppler support of the channel is $m = [-2, -1, \ldots, 2]$, and the magnitude of the WSF had a Gaussian distribution. The SNR for this case is also selected to be 20 dB. Figure 5.11 and Figure 5.12 present the simulation results using 1% and 10%
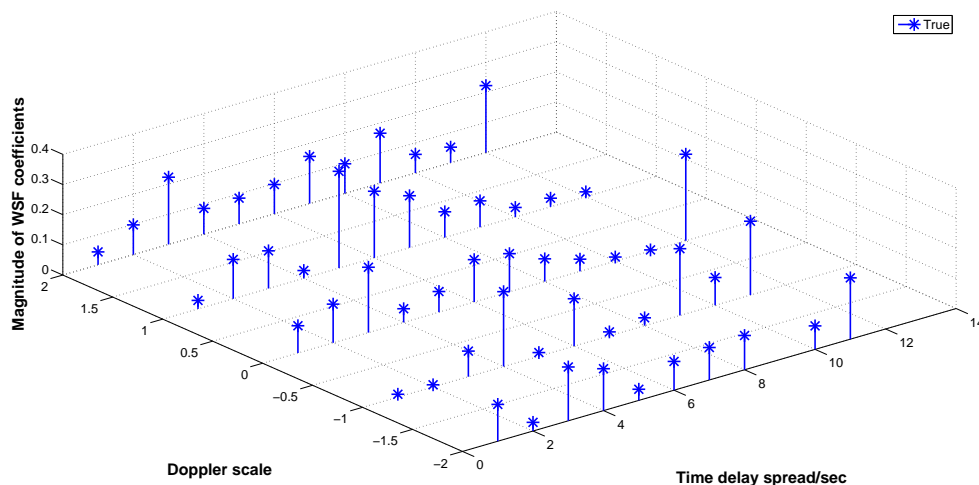

Figure 5.10: True WSF Coefficients for Fixed Channel Scenario Simulation: Case 2.

thresholding process.

5.4.2   Root Mean-Squared Error

The estimation root mean-squared error (RMSE) of 100 Monte Carlo iterations with 1% thresholding for both Case 1 and Case 2 are presented in this section.
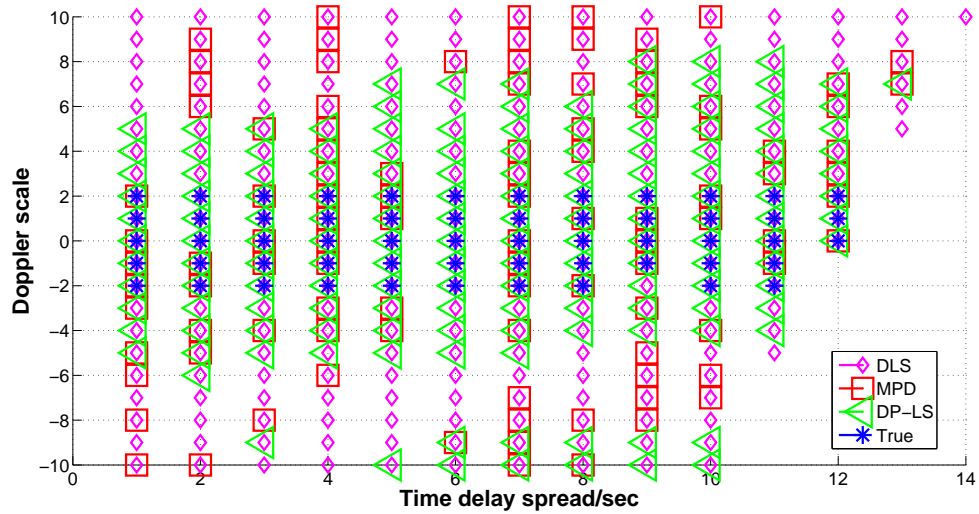
Figure 5.11: Estimated Channel Support with 1% Thresholding Process: Case 2.
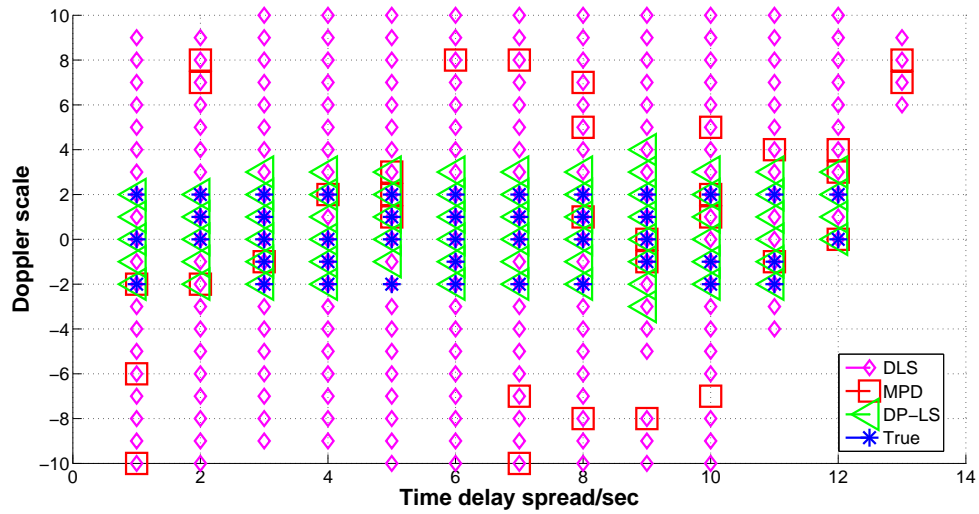

Figure 5.12: Estimated Channel Support with 10% Thresholding Process: Case 2.

RMSE: CASE 1

The RMSE simulation results for Case 1 are shown in Figure 5.13-5.17, where all the three channel estimation methods are compared when the actual Doppler path are $m = [-2, -1, \ldots, 2]$.
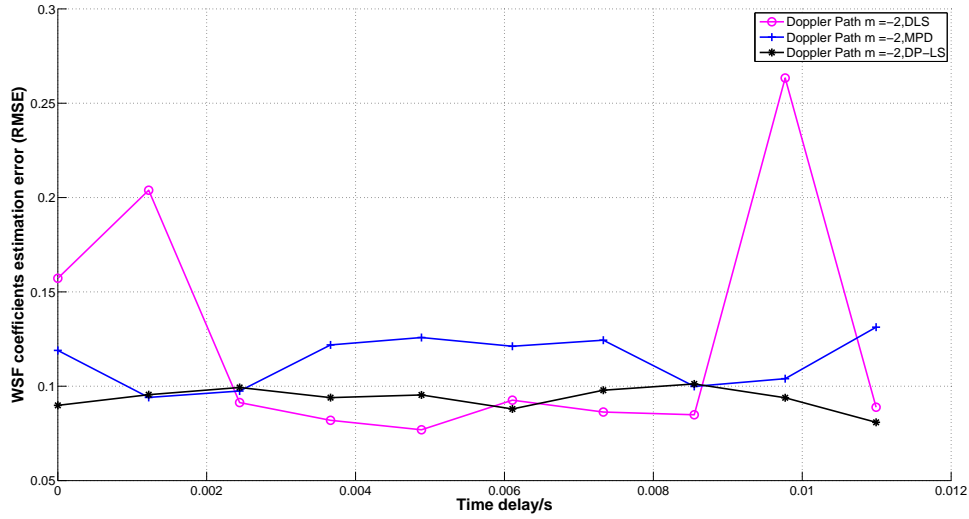

Figure 5.13: RMSE Estimation Error for Path $m = -2$ Using DLS, MPD and ACE Algorithms.

It can be seen that the DLS algorithm and ACE show better performance than the MPD algorithm. Although the DLS and the ACE algorithms both show good RMSE results, the DLS has a worse UWA channel support estimation, thus the ACE has the best overall performance for both channel support estimation and WSF coefficients estimation.

RMSE: CASE 2

The RMSE simulation results for Case 2 are shown in Figure 5.18-5.22, where all the three channel estimation methods are compared when the actual Doppler path are $m = [-2, -1, \ldots, 2]$.
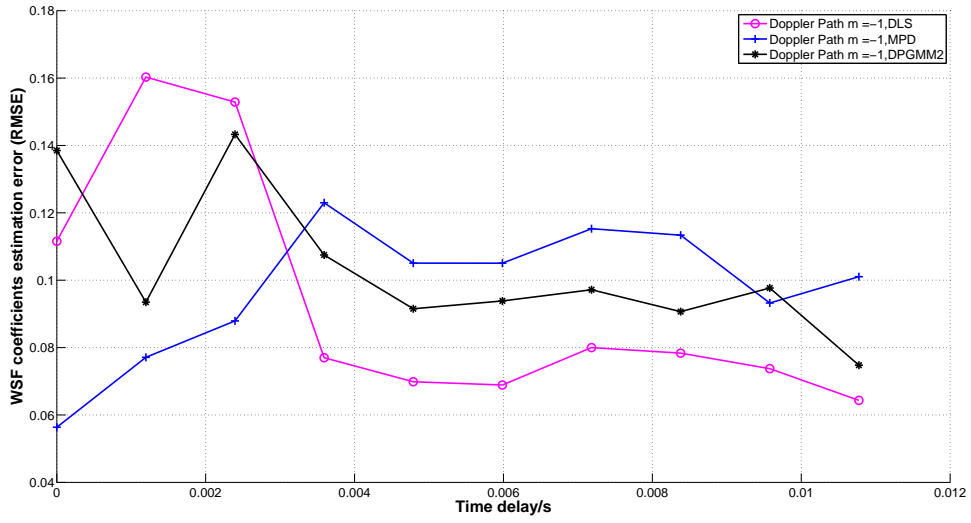
79

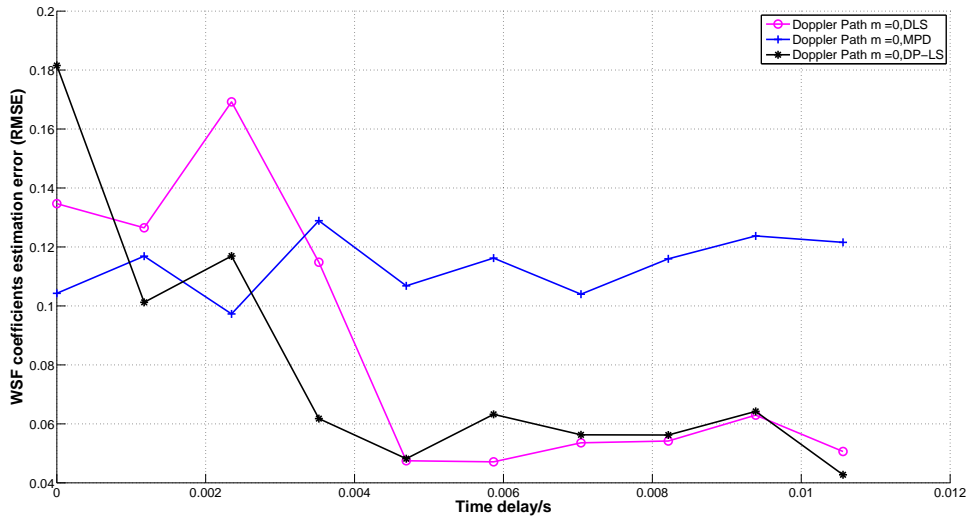**Figure 5.14:** RMSE Estimation Error for Path $m = -1$ Using DLS, MPD and ACE Algorithms.

Figure 5.15: RMSE Estimation Error for Path $m = 0$ Using DLS, MPD and ACE Algorithms.

Figure 5.16: RMSE Estimation Error for Path $m = 1$ Using DLS, MPD and ACE Algorithms.

Figure 5.17: RMSE Estimation Error for Path $m = 2$ Using DLS, MPD and ACE Algorithms.

81

Figure 5.18: RMSE Estimation Error for Path $m = -2$ Using DLS, MPD and ACE Algorithms.

Figure 5.19: RMSE Estimation Error for Path $m = -1$ Using DLS, MPD and ACE Algorithms.

Figure 5.20: RMSE Estimation Error for Path $m = 0$ Using DLS, MPD and ACE Algorithms.
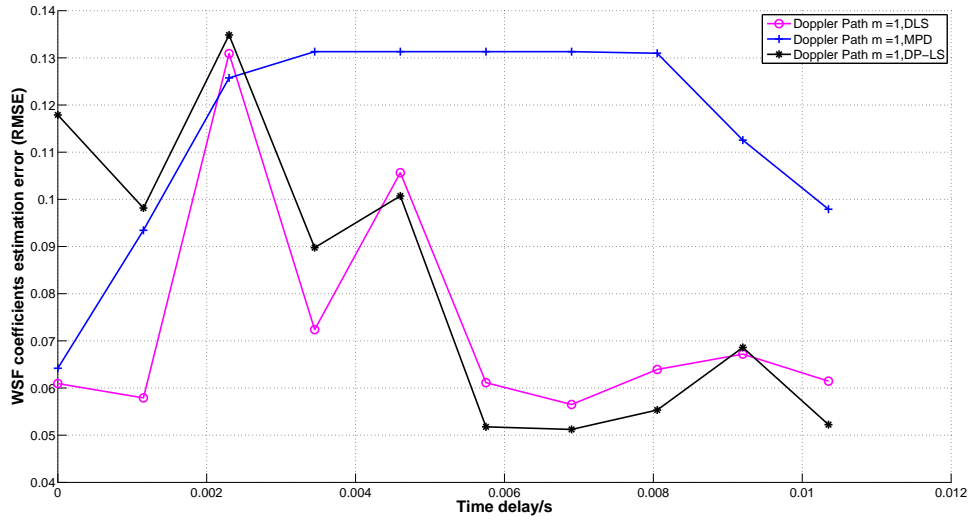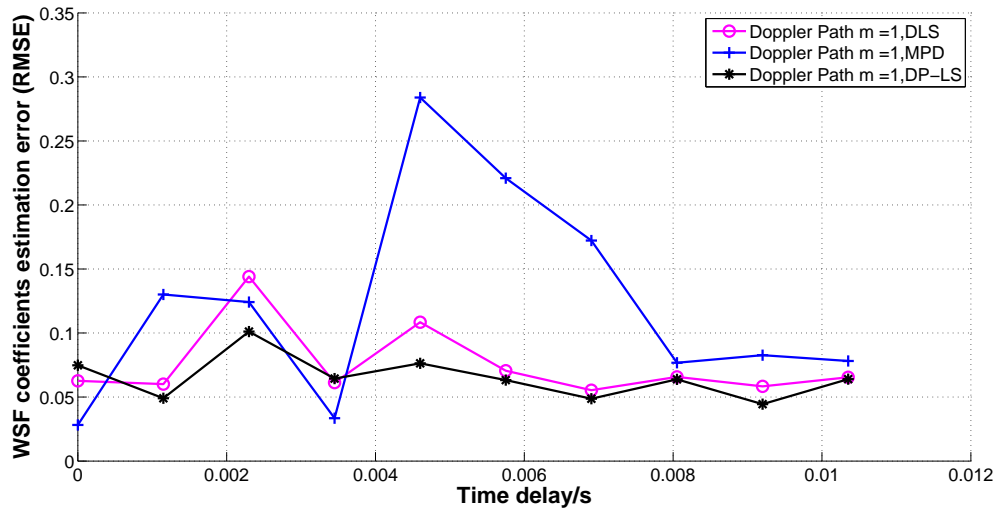

Figure 5.21: RMSE Estimation Error for Path $m = 1$ Using DLS, MPD and ACE Algorithms.
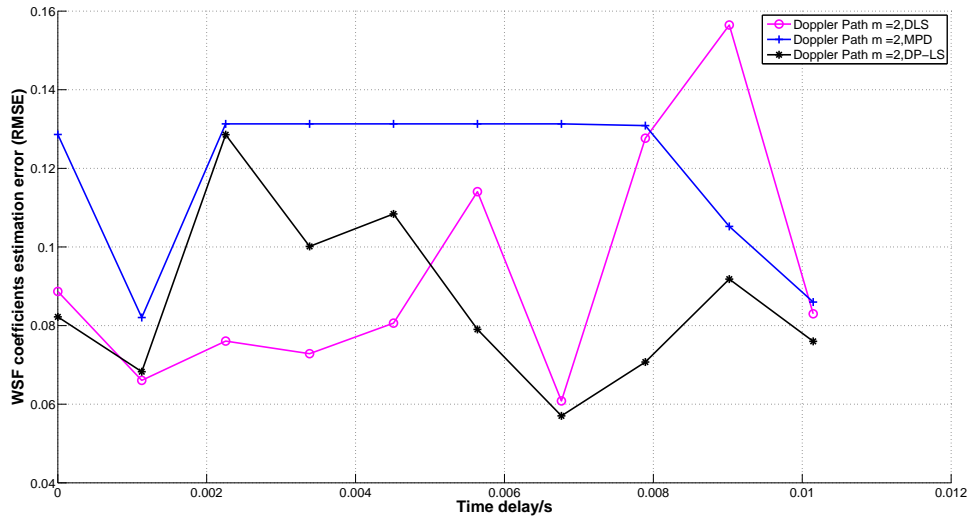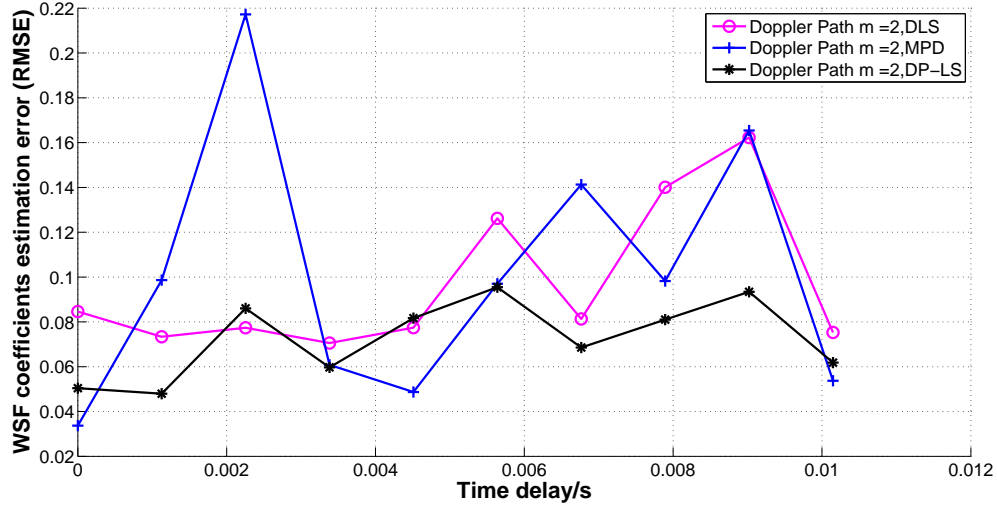
Figure 5.22: RMSE Estimation Error for Path $m = 2$ Using DLS, MPD and ACE Algorithms.
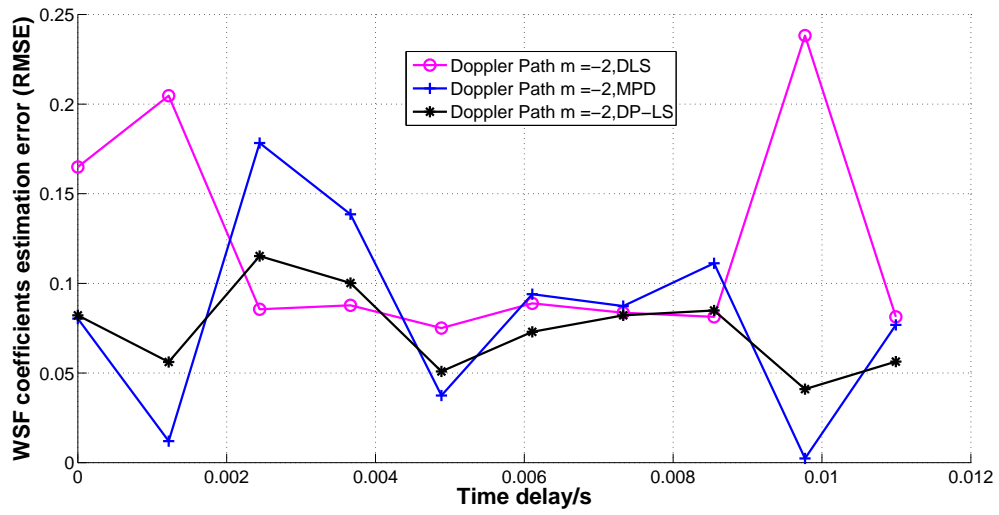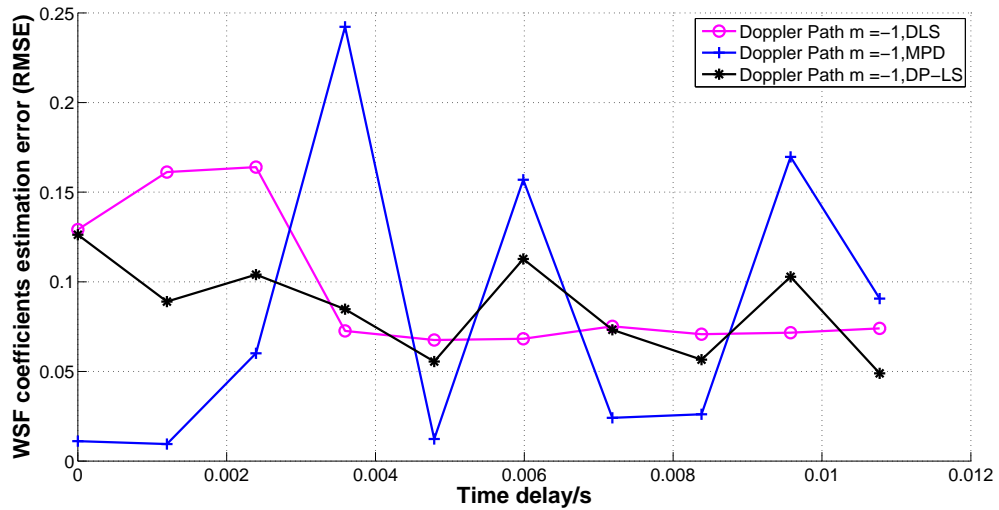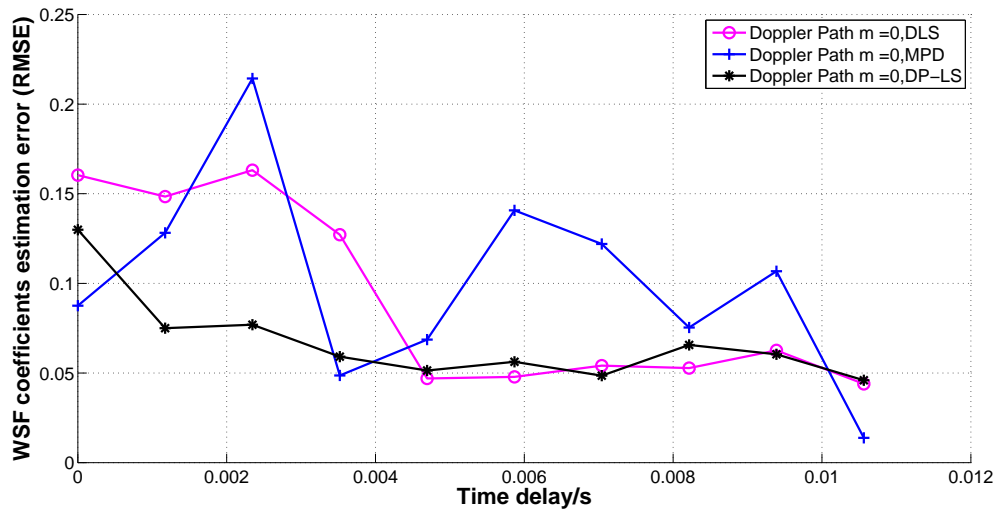
It can be seen that the similar results are noted as Case 1.

5.4.3 Estimation Accuracy

The estimation accuracy results are compared between all three algorithms. Three performance metrics are selected to evaluate the estimation accuracy including: true positive rate (TPR), false discovery rate (FDR), and precision or positive predictive value (PPV).

The three aforementioned metrics are defined as

$$\text{TPR} = \frac{\text{correct detections}}{\text{correct detections} + \text{missed detections}},$$

$$\text{FDR} = \frac{\text{false alarms}}{\text{correct detections} + \text{false alarms}},$$

$$\text{PPV} = \frac{\text{correct detections}}{\text{correct detections} + \text{false alarms}},$$

	TPR	FDR	PPV
DLS	1	0.76	0.24
MPD	1	0.67	0.33
ACE	0.87	0.38	0.62

Table 3: Table Doppler Path Estimation Performance

Estimation Accuracy: Case 1

Figure 5.23 to Figure 5.25 show a histogram plot of the Doppler scale index path estimation results. Note that, the x-coordinate is the value of m, and the y-coordinate is the frequency of path selection averaged over 100 Monte Carlo runs.
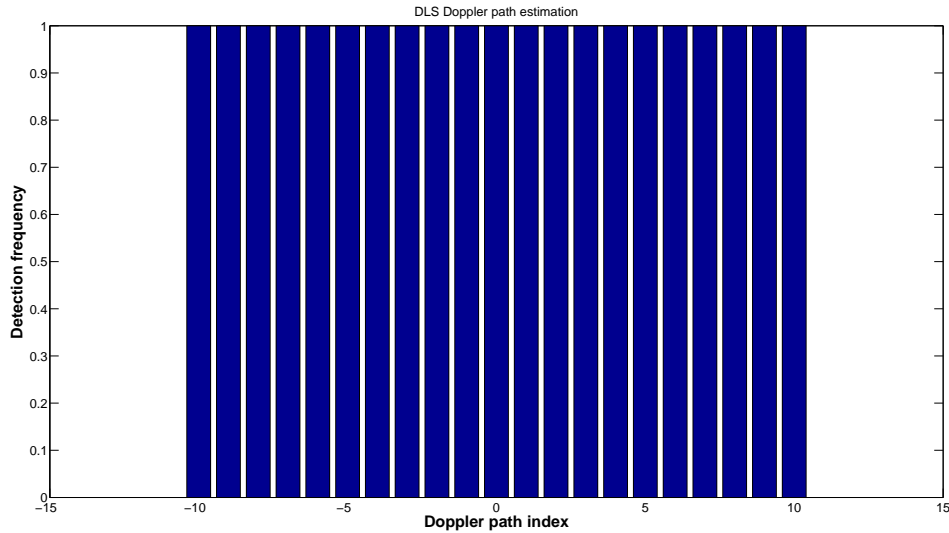
Figure 5.23: Estimation Accuracy of UWA Doppler Scale Index Path Using DLS Algorithm.

The Doppler path estimation performance for the DLS, MPD and ACE algorithms is listed in Table 3. These results show that the best overall performance is shown by the new ACE method.

The estimation accuracy performance for the WSF coefficients is shown in Figure 5.26-5.28. The x-coordinate is the value of m, and the y-coordinate is the frequency

Figure 5.24: Estimation Accuracy of UWA Doppler Scale Index Path Using MPD Algorithm.
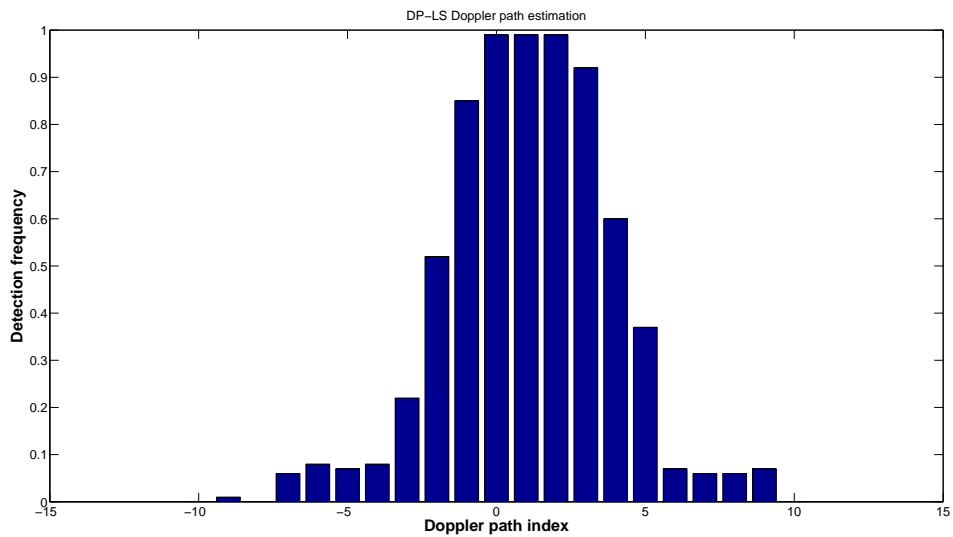
Figure 5.25: Estimation Accuracy of UWA Doppler Scale Index Path Using ACE Algorithm.

of WSF coefficients selection averaged over 100 Monte Carlo runs.

Figure 5.26: Estimation Accuracy of WSF Coefficients by Using DLS Algorithm.
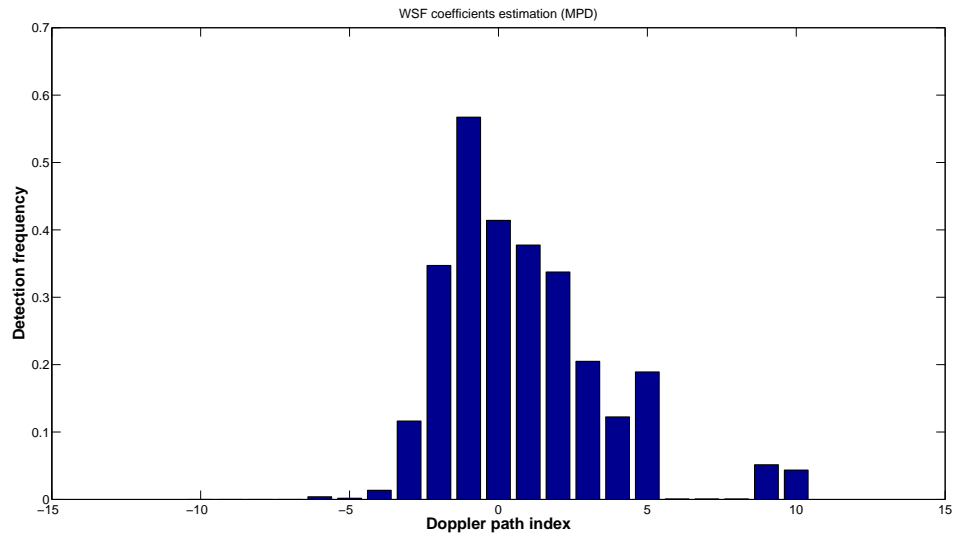
Figure 5.27: Estimation Accuracy of WSF Coefficients by Using MPD Algorithm.

And the performance of direct least square, MPD and DP-LS of WSF coefficients estimation is listed in Table 4. It can be observed that, the ACE method has the best overall performance.
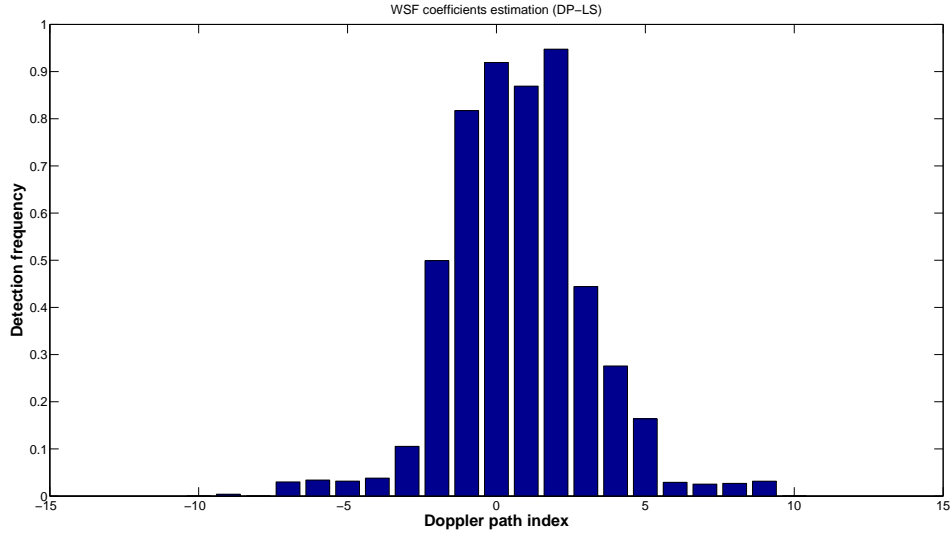
Figure 5.28: Estimation Accuracy of WSF Coefficients by Using ACE Algorithm.

	TPR	FDR	PPV
DLS	0.88	0.63	0.37
MPD	0.41	0.28	0.72
ACE	0.82	0.24	0.76

Table 4: Table WSF Coefficients Estimation Performance

Estimation Accuracy: Case 2

Figure 5.29 to Figure 5.31 shows the bar plot of Doppler scale index path estimation results. And the performance of the DLS, MPD and ACE algorithms is listed in Table 5. Similar results can be seen as Case 1, the ACE has the best overall performance.

The estimation accuracy performance for WSF coefficients are shown in Figure

	TPR	FDR	PPV
DLS	1	0.76	0.24
MPD	0.99	0.73	0.27
ACE	0.88	0.36	0.64

Table 5: Table Doppler Path Estimation Performance: Case 2
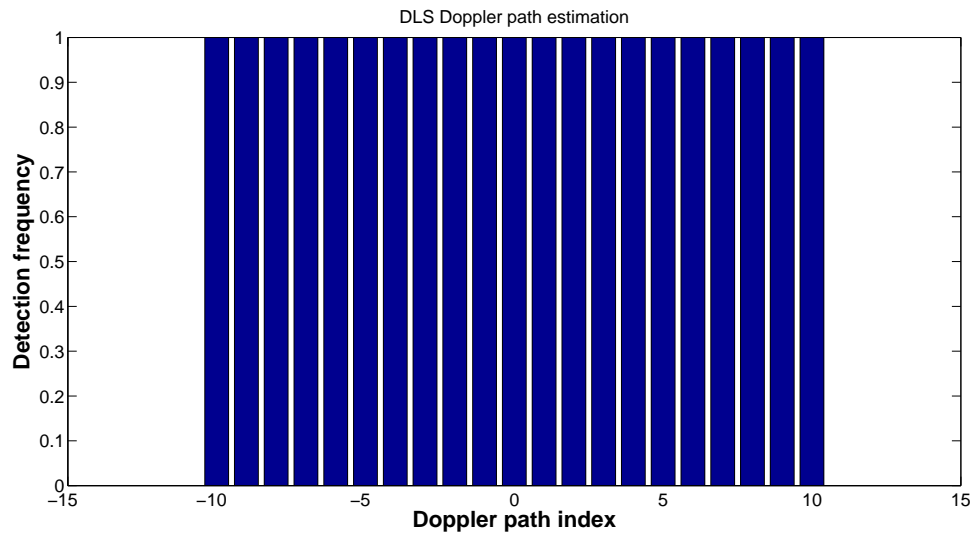
Figure 5.29: Estimation Accuracy of UWA Doppler Scale Index Path Using DLS Algorithm: Case 2.
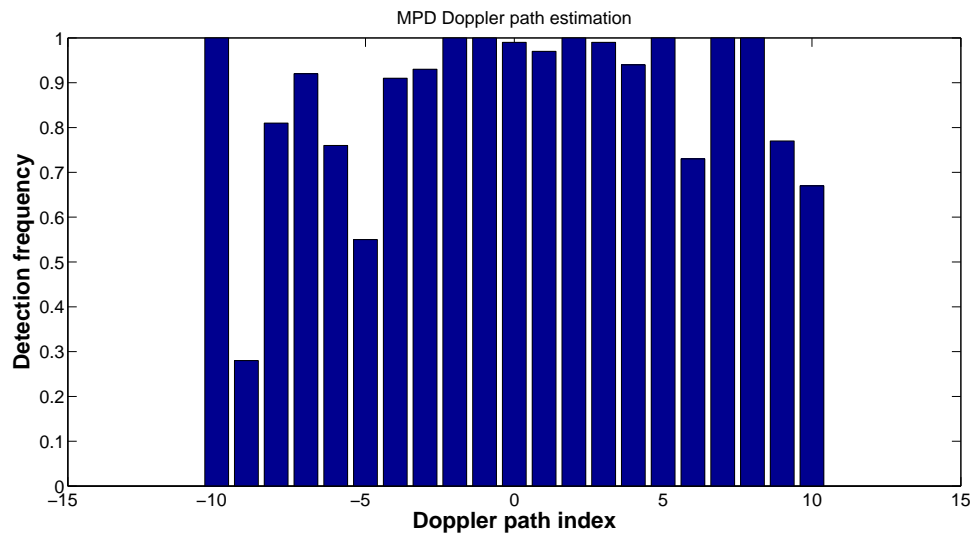
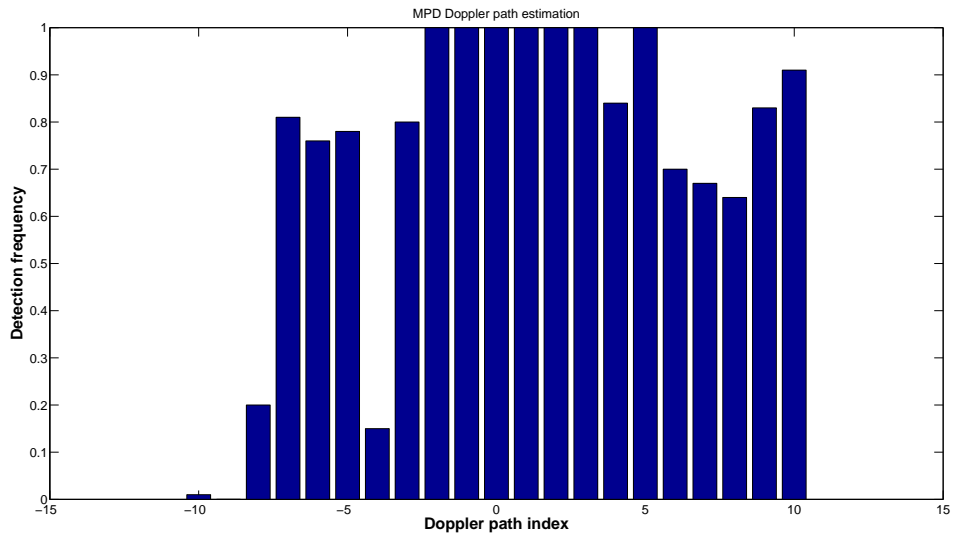**Figure 5.30:** Estimation Accuracy of UWA Doppler Scale Index Path Using MPD Algorithm: Case 2.

89
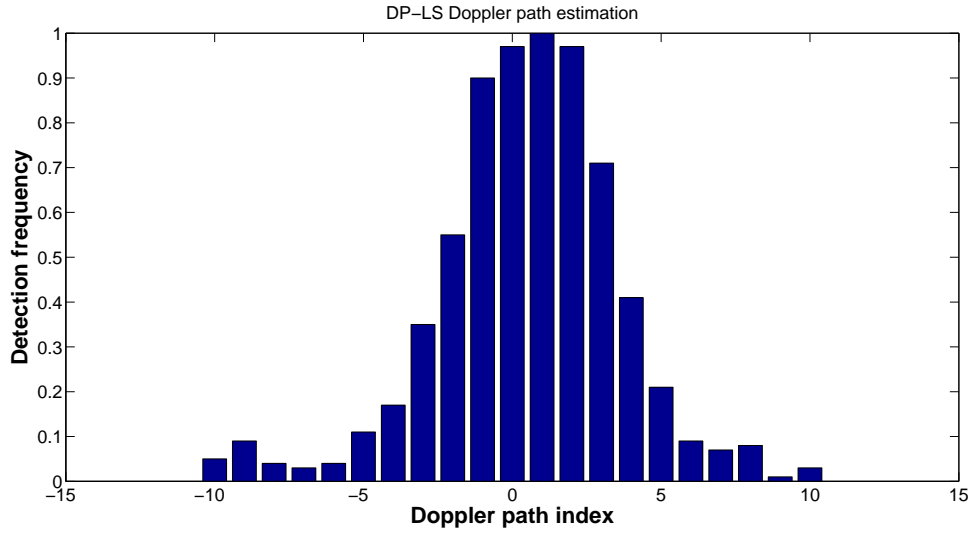
Figure 5.31: Estimation Accuracy of UWA Doppler Scale Index Path Using ACE Algorithm: Case 2.

5.32 to Figure 5.34. The performance of DLS, MPD and ACE algorithms is listed in Table 6, and ACE has the best overall performance.
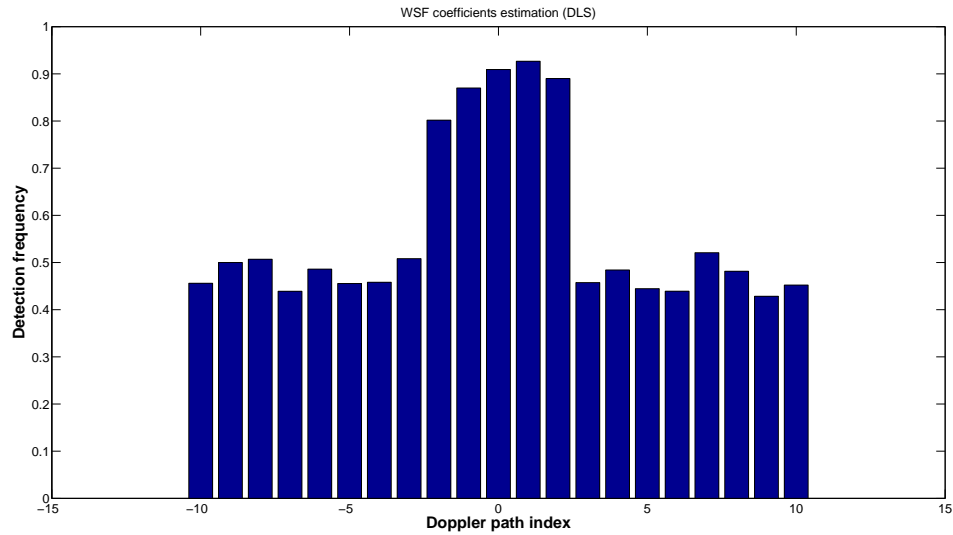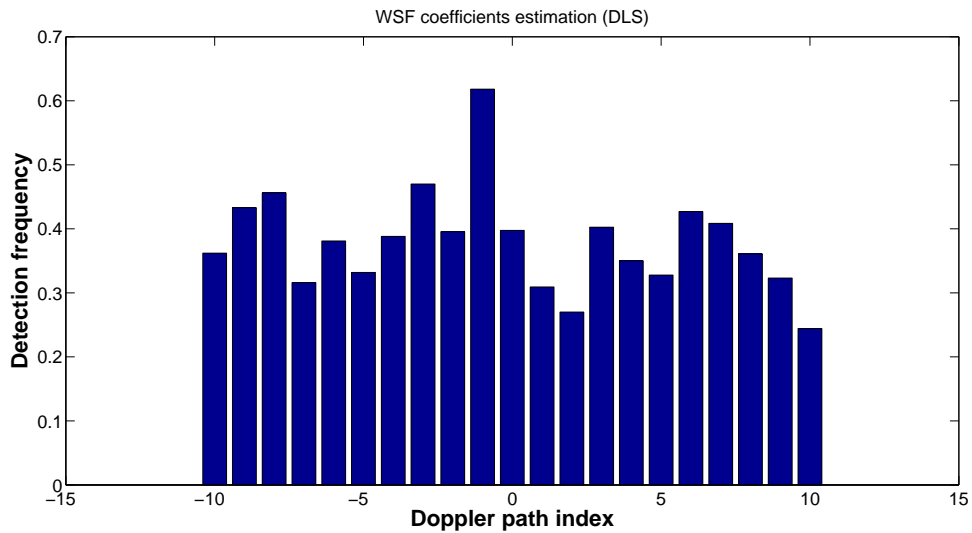

Figure 5.32: Estimation Accuracy of WSF Coefficients Using DLS Algorithm: Case 2.
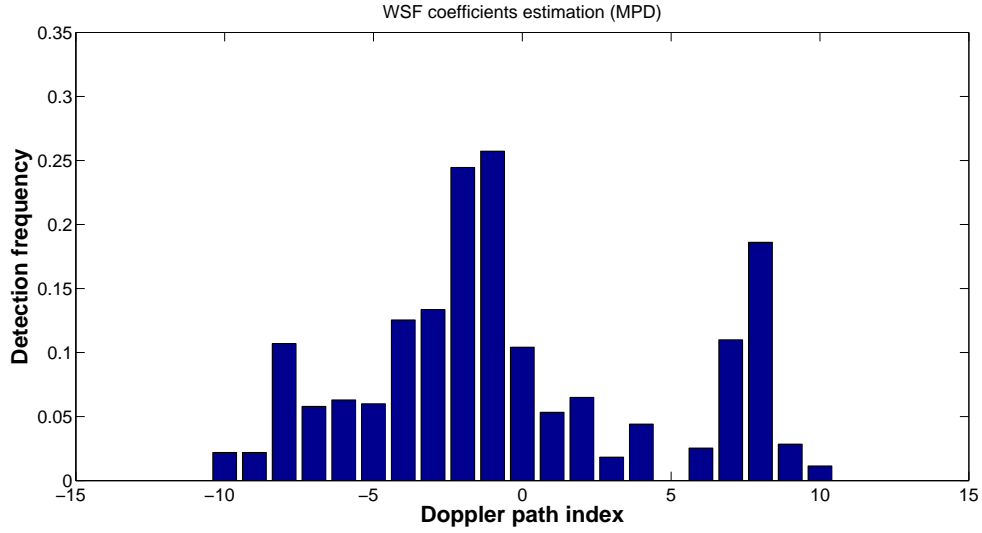
Figure 5.33: Estimation Accuracy of WSF Coefficients Using MPD Algorithm: Case 2.
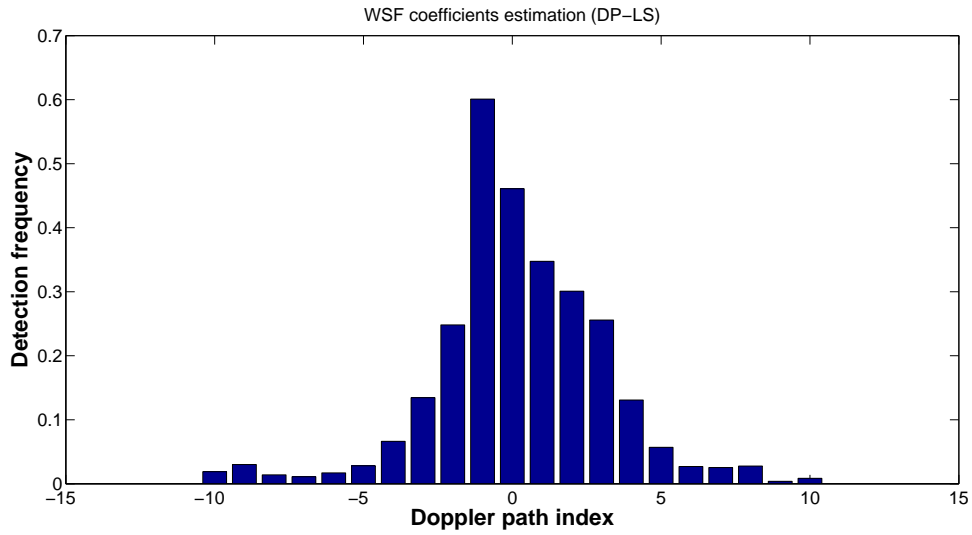
Figure 5.34: Estimation Accuracy of WSF Coefficients Using ACE Algorithm: Case 2.

	TPR	FDR	PPV
DLS	0.45	0.77	0.23
MPD	0.14	0.59	0.41
DPLS	0.42	0.35	0.65

Table 6: Table WSF Coefficients Estimation Performance: Case 2

Chapter 6

MULTI-USER UNDERWATER ACOUSTIC COMMUNICATION SYSTEM
DESIGN

In this chapter, we first propose a single user communication signaling scheme
that is matched to the underwater acoustic environment using hyperbolic frequency-
modulated (HFM) signals. This is achieved using scale diversity by designing the
HFM signal frequency modulation (FM) assigned for each transmitted symbols. HFM
signals are inherently Doppler scale invariant and have been used in other applications
such as sonar [97]. We combine the HFM signaling scheme with CDMA for a multi-
user UWA communication system to improve multi-user detection performance. In
addition, we extend our results and propose a new multi-user UWA communication
scheme using HFM signals. By appropriately constraining the signal's FM rate, we
minimize multiple access interference (MAI) at the transmission side. We also take
into consideration that HFM signals are scale-invariant and thus potentially suitable
for wideband channel transmission.

6.1   UWA Communications Using HFM Signaling Scheme

Multi-user underwater communication is challenging for many reasons including,
limited bandwidth, interference between each user, and wideband channel distortions.
Depending on the communication range, the available bandwidth varies, and in gen-
eral, the available bandwidth decreases ass when the communicating range increases.
In order to successfully decode the transmitted information bits, the transmitted sig-
nals need to be designed properly. As signals from users could be synchronously
transmitted or can overlap in time during transmission, there is interference between

each user. Traditional multiple access methods attempt to assign each user a distinct communication channel or time slot to avoid the interference (frequency-division multiple access and time-division multiple access). To increase the bandwidth efficiency as well as the transmit bit rate, algorithms such as code-division multiple access and orthogonal frequency division multiplex have been used. Although the user signals overlap for these algorithms, their interference can be minimized or significantly reduced by the signaling scheme design. For the wideband UWA channel, the distortions include time delay and Doppler scale, and most multiple access methods are proposed to overcome the time delay issue. In this section, we propose to use hyperbolic frequency-modulated (HFM) signal based signaling schemes to achieve multi-user UWA communications.

6.1.1 Nonlinear Frequency-Modulated Signaling Scheme

Time-varying signals, unlike sinusoids, have frequency content that changes with time. The model for a nonlinear frequency-modulated (NFM) signal can be written as

$$s_g(t) = A e^{j2\pi(c\xi(\frac{t+t_c}{t_r}))}, \quad t \in [0, T]$$

where $\xi(\cdot)$ is the phase response of the NFM signal, t_c determines the carrier frequency, A is the amplitude, and $c\nu(t) = c\frac{d}{dt}\xi(\frac{t+t_c}{t_r})$ is its instantaneous frequency, where c is the FM rate and $t_r > 0$ is a positive reference time.

Table 1 provides examples of NFM signals and Table 2 provides their corresponding phase functions and instantaneous frequency (IF) functions.

Type Index	Signal Type
Type 1	Linear Frequency-Modulated (LFM) Signal
Type 2	Hyperbolic Frequency-Modulated (HFM) Signal
Type 3	Logarithmic Frequency-Modulated Signal
Type 4	Power Frequency-Modulated Signal

Table 1: Examples of NFM Signals

NFM Signal Type	Phase Function $\xi(\cdot)$	IF $c\nu(t)$
Type 1	$\xi(t) = (t + t_c)^2$	$c\nu(t) = 2ct$
Type 2	$\xi(t) = \ln(t + t_c)$	$c\nu(t) = c/(t + t_c)$
Type 3	$\xi(t) = (t + t_c)\ln(t + t_c) - (t + t_c)$	$c\nu(t) = c\ln(t + t_c)$
Type 4	$\xi(t) = (t + t_c)^{\kappa/(\kappa-1)}$	$c\nu(t) = c\frac{\kappa}{\kappa-1}(t + t_c)^{1/(\kappa-1)}$

Table 2: Examples of NFM Signals with Corresponding Phase Function and IF

6.1.2   HFM Design for Scale Diversity

We specifically design a single-user communications signaling scheme using HFM signals. We select HFM signals because they are well-matched to the wideband UWA channel as they are invariant to Doppler scale changes. The HFM signal with FM rate c_i is defined as

$$s_i(t) = e^{j2\pi c_i \ln((t+t_c)/t_r)}, \quad t \in [0, T] \tag{6.1}$$

where T is the signal duration. We select the FM rate c_i of the HFM signal as an UWA communication signal to represent the ith symbol, $i = 0, 1$.

We want to use the HFM signal to design a signaling scheme to match the underwater acoustic environment in a manner similar to sinusoids matching the wireless environment. Specifically, when a sinusoid $x(t) = e^{j2\pi f_0 t}$ is time shifted, $x(t - \tau) = e^{j2\pi f_0(t-\tau)} = e^{-j2\pi f_0 \tau} x(t)$, the exponent is separable and the time shift does not change the magnitude of the signal. Considering the HFM signal as a dual signal and the scaling transformation, when the HFM signal $s(t) = e^{j2\pi c \ln(t/t_r)}$ is scaled by

94

a factor a, $s(at) = e^{j2\pi c \ln(at/t_r)} = e^{j2\pi c \ln(a)} s(t)$, the exponent is also separable. Note, however, that for the joint UWA channel multipath and scaling transformations on the HFM signal, $e^{j2\pi c \ln((at-\tau)/t_r)}$, the exponent is not separable. The separability is necessary for the signal to be invariant to both aforementioned distortions.

Although perfect separability is not possible, we want to derive constraints on the FM rates of the HFM signal in order to minimize the correlation between any two HFM signals transmitted over an UWA channel. Specifically, consider the correlation function between two time-shifted and Doppler scaled HFM signals with different FM rates

$$\Phi_{i,l,(n,m),(p,q)} = \int_T \mathsf{s}_{i,(n,m)}(t)\, \mathsf{s}^*_{l,(p,q)}(t)\, dt\,, \quad i,l = 0,1\,, \tag{6.2}$$

where

$$\mathsf{s}_{i,(n,m)}(t) = e^{j2\pi c_i \ln(a_m t - \tau_n + t_c)}$$

is the time-shifted and Doppler scaled version of the transmitted signal in (6.1) with $t_r = 1$ s, $a_m = a_d^m$ and $\tau_n = n/W$ in (5.2) for the ith symbol, and

$$\mathsf{s}_{l,(p,q)}(t) = e^{j2\pi c_l \ln(a_q t - \tau_p + t_c)}$$

is the time-shifted and Doppler scaled version of the transmitted signal in (6.1) with $t_r = 1$ s, $a_q = a_d^q$ and $\tau_p = p/W$ in (5.2) for the lth symbol. The signal product in (6.2) can be calculated as:

$$\mathsf{s}_{i,(n,m)}(t)\, \mathsf{s}^*_{l,(p,q)}(t) = A\, B(t)\, C(t), \tag{6.3}$$

where

$$A = \exp\left(j2\pi \ln \frac{(a_m)^{c_i}}{(a_q)^{c_l}}\right), \tag{6.4}$$

$$B(t) = \exp\left(j2\pi \ln \left(\frac{t - \tau_n/a_m + t_c/a_m}{t - \tau_p/a_q + t_c/a_q}\right)^{c_i}\right), \tag{6.5}$$

$$C(t) = \exp\left(j2\pi \ln (t - \tau_p/a_q + t_c/a_q)^{c_i - c_l}\right). \tag{6.6}$$

95

Note that (6.4) is not a function of time. Equation (6.5) can be re-written as

$$B(t) = \exp\left(j2\pi c_i \ln\left(1 + \frac{((\tau_p - t_c)/a_q - (\tau_n - t_c)/a_m)}{t - \tau_p/a_q + t_c/a_q}\right)\right). \tag{6.7}$$

We assume that the two time-shifts are the same, $\tau_n = \tau_p$, and usually in practice the Doppler scale coefficient is very close to 1, in which case, $1/a_m - 1/a_q \approx 0$. Then, we can approximate

$$\ln\left(1 + \frac{(\tau_p - t_c)\left(\dfrac{1}{a_q} - \dfrac{1}{a_m}\right)}{t - \dfrac{\tau_p}{a_q} + \dfrac{t_c}{a_q}}\right) \approx \frac{(\tau_p - t_c)\left(\dfrac{1}{a_q} - \dfrac{1}{a_m}\right)}{t - \dfrac{\tau_p}{a_q} + \dfrac{t_c}{a_q}}$$

and thus re-write (6.7) as

$$B(t) \approx \exp\left(j2\pi c_i \frac{(\tau_p - t_c)\left(\dfrac{1}{a_q} - \dfrac{1}{a_m}\right)}{t - \dfrac{\tau_p}{a_q} + \dfrac{t_c}{a_q}}\right) \approx 1. \tag{6.8}$$

This was obtained using the Taylor series expansion of the logarithmic phase function in (6.7). Note that the Taylor series, for any function $f(x)$, expanded at $x = x_0$ can be written as

$$f(x) = f(x_0) + \frac{f'(x_0)}{1!}(x - x_0) + \frac{f''(x_0)}{2!}(x - x_0)^2 \dots$$
$$= \sum_{n=0}^{\infty} \frac{f^{(n)}(x_0)}{n!}(x - x_0)^n$$

where $f'(x)$ and $f''(x)$ are the first and second derivatives of $f(x)$ with respect to x. If the function is $f(x) = \ln(1 + x)$, the Taylor expansion at $x = \Delta x$ is

$$\ln(1 + x) = \ln(1 + \Delta x) + \frac{1}{1 + \Delta x}(x - \Delta x) + \dots$$

When $\Delta x \approx 0$, we have

$$\ln(1 + x) \approx x.$$

96

The resulting correlation in Equation (6.2), after substituting Equations (6.4), (6.8) and (6.6) into (6.3), becomes

$$\Phi_{i,l,(n,m),(p,q)} \approx \int_{\tau_p/a_q}^{T+\tau_p/a_q} \exp\left(j2\pi \ln \frac{(a_m)^{c_i}}{(a_q)^{c_l}}\right) \exp\left(j2\pi \ln \left(t - \frac{\tau_p}{a_q} + \frac{t_c}{a_q}\right)^{c_i - c_l}\right) dt.$$

If we let $\zeta = \ln\left(t - \frac{\tau_p}{a_q} + \frac{t_c}{a_q}\right)$, then (6.2) can be approximated to

$$\Phi_{i,l,(n,m),(p,q)} \approx e^{j2\pi \ln (a_m^{c_i}/a_q^{c_l})} \int_{\ln(t_c/a_q)}^{\ln(t_c/a_q+T)} e^{j2\pi(c_i-c_l)\zeta} e^{\zeta} \, d\zeta.$$

Thus, it can be shown that the correlation between any pair of UWA channel propagated HFM signals is mainly a function of scale transformed signals and depends on the difference between the two FM rates. The resulting correlation in (6.2) between the HFM with FM rate c_i and the HFM with FM rate c_l becomes

$$\Phi_{i,l,(n,m),(p,q)} = \exp(j2\pi \ln (a_m^{c_i}/a_q^{c_l}))/(1 + j2\pi\Delta c_{il}) \tag{6.9}$$

$$\left(\left(\frac{t_c}{a_q} + T\right) \exp\left(j2\pi\Delta c_{il} \ln \left(\frac{t_c}{a_q} + T\right)\right) - \frac{t_c}{a_q} \exp(j2\pi\Delta c_{il} \ln \left(\frac{t_c}{a_q}\right)) \right)$$

where $D_{i,l} = c_i - c_l$, $i \neq l$. By plotting the scale correlation in (6.10) in Figure 6.1, it can be seen that as the FM difference Δc_{il} increases, the scale correlation decreases significantly.

Thus, the HFM FM rates c_i and c_l for a single user to transmit symbols i and l, $i \neq l$, over an UWA communications channel, with reduced interference, must satisfy the condition:

$$\text{select } D_{i,l} = |c_i - c_l|, \; i \neq l, \text{ to be large}, \tag{6.10}$$

6.1.3   UWA Communications Using HFM Signaling Scheme

The HFM signaling scheme can be used for single user UWA communications. The received signal $r(t)$ of a wideband UWA communication channel can be written
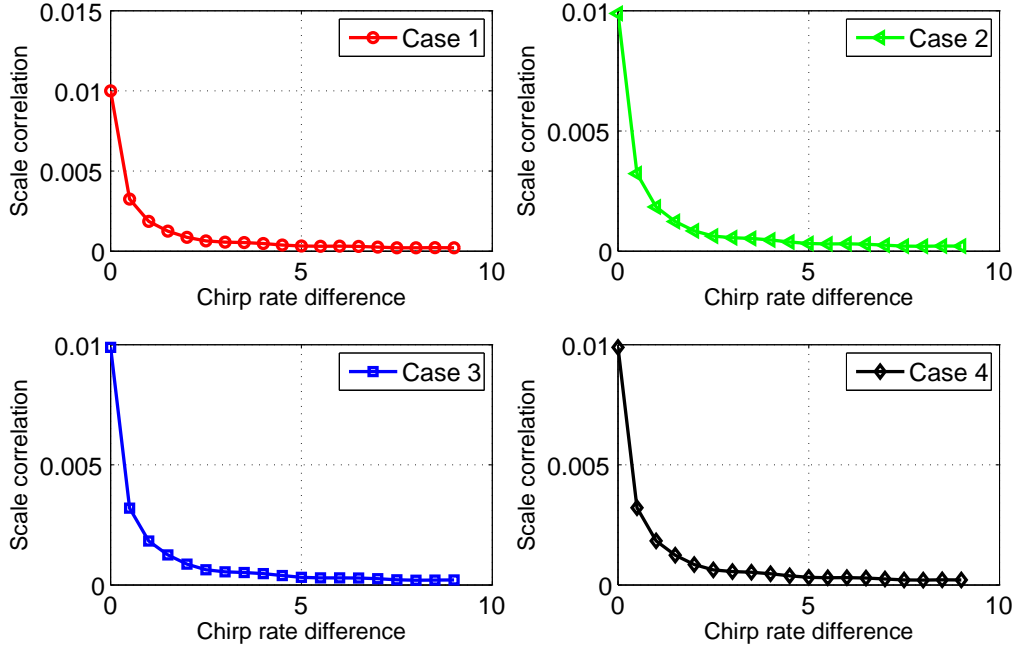
Figure 6.1: Scale Correlation in Equation (6.10) for Increasing Values of The FM Rate Difference $D_{i,l} = c_i - c_l$. Four Different Cases Are Shown as Two Possible Doppler Scaling Paths Are Considered.

as

$$
\begin{aligned}
r(t) &= y_i(t) + w(t) \\
&= \sum_{m=M_0}^{M_1} \sum_{n=0}^{N(m)} \chi_{n,m} a_d^{m/2} \, s_i\left(a_d^m t - \frac{n}{W} \right) + w(t)
\end{aligned}
$$

for symbol $i = 0, 1$, where $w(t)$ is additive white Gaussian noise. The correlated signal is obtain as

$$
\Lambda(y_i) = \int_{-\infty}^{\infty} r(t) \, y_i^*(t) \, dt \,. \tag{6.11}
$$

Since each symbol is transmitted with equal probability, the information bit can be estimated as

$$
\hat{i} = \arg\max_{i=0,1} \ \Lambda(y_i) \,.
$$

Note that we assume that the UWA channel WSF coefficients are estimated *a priori*; methods for estimating the WSF coefficients were presented in Chapter 5.

The block diagram for the single user communication system can be seen in Figure 6.2.
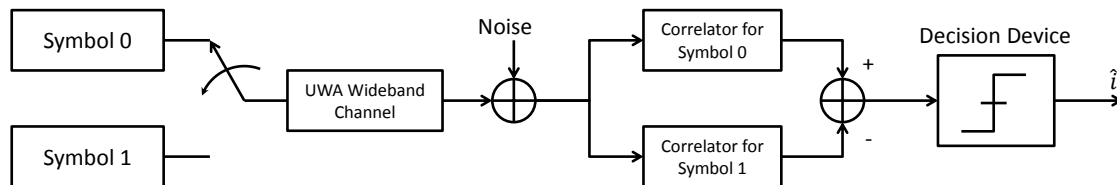
Figure 6.2: Block Diagram for Single User Underwater Communication System.

6.2 HFM Signaling for Multiple Users

6.2.1 HFM with CDMA Multi-User Signaling Scheme

When HFM signaling scheme is combined with CDMA, it can be successfully used for multi-user detection in UWA communication channels. Assuming a K-user communication system, the ith transmitted symbol of the kth user, $k = 1, \ldots, K$, $i = 0, 1$ can be written as

$$s_i^{(k)}(t) = s_i(t) \, \mathrm{PN}^{(k)}(t) \,,$$

where $\mathrm{PN}^{(k)}(t)$ is the pseudorandom noise (PN) code of the kth user.

After transmission over the wideband UWA channel, the observed signal at the receiver can be written as

$$r(t) = \sum_{k=1}^{K} y_i^{(k)}(t) + w(t),$$

where

$$y_i^{(k)}(t) = \sum_{m=M_0}^{M_1} \sum_{n=0}^{N(m)} \chi_{n,m} \, a_d^{m/2} \, s_i^{(k)}(a_d^m t - n/W),$$

99

and $w(t)$ is assumed to be an additive white Gaussian noise. Following (6.11), the correlation between the received signal and the expected signal for the k user, assuming symbol i, is given by

$$\Lambda(y_i^{(k)}) = \int_{-\infty}^{\infty} r(t)\, y_i^{(k)*}(t)\, dt$$

$$= \sum_{m=M_0}^{M_1} \sum_{n=0}^{N(m)} \chi_{n,m}\, a_d^{m/2} \int_{-\infty}^{\infty} r(t)\, s_i^{(k)}\left(a_d^m t - \frac{n}{W}\right)\, \mathrm{PN}^{(k)}\left(a_d^m t - \frac{n}{W}\right)\, dt$$

The information bit of the kth user can be estimated as

$$\hat{i} = \arg\max_{i=0,1}\, \Lambda(y_i^{(k)}).$$

The block diagram for the multi-user communication system using HFM-NAM with CDMA can be seen in Figure 6.3.

Figure 6.3: Block Diagram for Multi-User Underwater Communication System with HFM Combined CDMA.

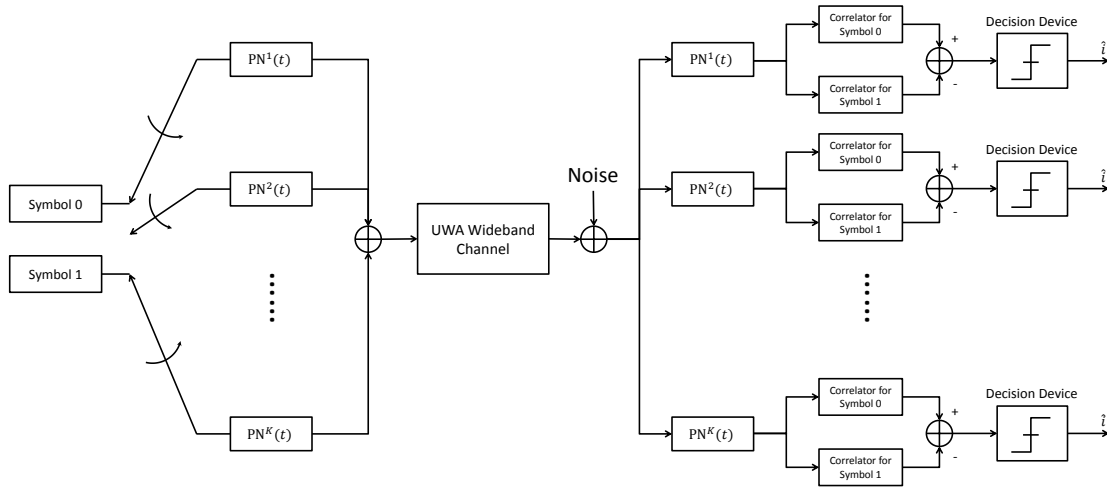### 6.2.2   Orthogonal HFM Design for Multiple-Access Interference Minimization

In order to accommodate multiple users using the HFM signaling scheme, we consider an amplitude-modulated (AM) version of the signal in (6.1), as in [98]. The

amplitude modulation leads to signal orthogonality for infinite duration signals; for finite duration signals, it leads to high correlation when signals match in FM rate. Making use of this property in a communications system with K users, each user is assigned one of K sub-channels by equally dividing the available bandwidth. For a K-user system, the HFM signal for the ith transmitted symbol of the kth user, $k = 1, \ldots, K$, $i = 0, 1$, is

$$s_i^{(k)}(t) = \frac{1}{\sqrt{t + t_c}} \, e^{j 2\pi c_i^k \ln\left((t+t_c)/t_r\right)} . \tag{6.12}$$

We assign an FM rate to each user in such a way as to minimize the cross correlation between the signals of any two users and thus reduce multiple access interference (MAI) among users. In order to determine the FM rates for approximate orthogonal signaling, we consider the signals for the ith symbol of the kth user and the lth symbol of the jth users as

$$s_i^{(k)}(t) = \frac{1}{\sqrt{t + t_c}} \, e^{j 2\pi c_i^k \ln\left((t+t_c)/t_r\right)}$$

$$s_l^{(j)}(t) = \frac{1}{\sqrt{t + t_c}} \, e^{j 2\pi c_l^j \ln\left((t+t_c)/t_r\right)} . \tag{6.13}$$

The correlation between the signals in (6.13), setting $t_r = 1$, can be calculated as [38]

$$q_{i,l}^{k,j} = \int s_i^{(k)}(t) s_l^{*(j)}(t) dt = \int_0^T \frac{1}{t + t_c} e^{j 2\pi (c_i^k - c_l^j) \ln(t+t_c)} dt.$$

The closed form of the correlation magnitude is given by

$$|q_{i,l}^{k,j}| = \eta_T \, \mathrm{sinc}((c_i^k - c_l^j) \, \eta_T)$$

where $\eta_T = \ln(T + t_c) - \ln(t_c)$ and $\mathrm{sinc}(x) = \sin(\pi x)/(\pi x)$. In order to minimize the correlation, we can select the FM rates c_i^k and c_l^j such that $(c_i^k - c_l^j) \, \eta_T$ is any integer. Based on this, we select the FM rate for the kth user, $k = 1, \ldots, K$, $i = 0, 1$, to satisfy the condition

$$c_i^k = \frac{2K + 1 - 2k + i}{\eta_T} = \frac{2K + 1 - 2k + i}{\ln(T + t_c) - \ln(t_c)} \tag{6.14}$$

based on a maximum $B_{\max}T$ time-bandwidth signal constraint. Using the FM rate in (6.12), we ensure that the correlation in (6.14) is zero. A less restrictive condition that still reduces correlation is obtained by selecting the FM rates of the kth and jth users such that

$$(c_i^k - c_l^j)\left[\ln(T + t_c) - \ln(t_c)\right] \gg 1 .\tag{6.15}$$

Using the maximum HFM signal time-bandwidth constraint for all users, the maximum number of possible users is [38]

$$K_{\max} = \left\lceil \left(\frac{1}{2}(B_{\max}\, t_c\, \eta_T - 1)\right)\right\rceil .\tag{6.16}$$

Figure 6.4 demonstrates the relationship between the maximum bandwidth, FM rates for each user, and total number of users.
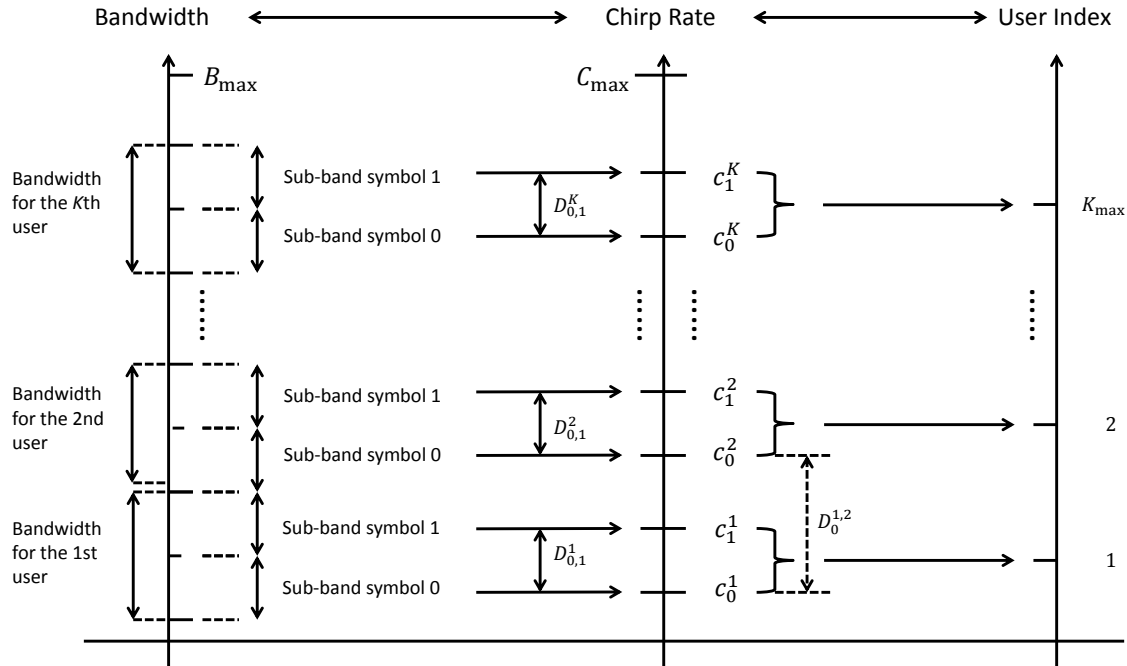

Figure 6.4: Relationship Between Bandwidth, FM Rates, and Users.

6.2.3 Multi-User UWA Communications Using HFM Signaling Scheme

We now consider the combined case of multiple users in an UWA communications channel. In order to use the HFM signaling scheme, we combine the two conditions we derived in Equations (6.10) and (6.14) (or for a less restrictive case, the two conditions in Equations (6.10) and (6.15)). The sub-channel for each user is further divided in two bands so that each user can transmit two binary symbols.

We assume that User k transmits Symbol i and User j transmits Symbol l. Using the symbol FM condition in (6.10) ensures that the following FM rate differences are large: $D_{i,l}^{k} = |c_i^k - c_l^k|$, $i \neq l$ and $D_i^{k,j} = |c_i^k - c_i^j|$. Using (6.15) ensures that $(c_i^k - c_l^j)\eta_T \gg 1$, $i, l = 0, 1$, $k \neq j$. Combining (6.10) and (6.15) then ensures that $D_{i,l}^{k,j}$ is also large for $i \neq l$ and $k \neq j$. Thus, although the FM rate condition in (6.14) is derived using the HFM in (6.12), we combine it with the condition in (6.10) to represent any pair of two FM rates. The transmitted signal model for the combined scheme is

$$s_i^{(k)}(t) = \frac{1}{\sqrt{t + t_c}} \, e^{j2\pi c_i^k \ln ((t + t_c)/t_r)} \quad t \in (0, T]. \tag{6.17}$$

Figure 6.5 demonstrates the relationship between all K users transmitted symbols in the time-frequency plane.

After propagating through the wideband UWA channel, the observed signal of User k transmitting Symbol i at the receiver can be written as

$$r(t) = \sum_{k=1}^{K} y_i^{(k)}(t) + w(t),$$

where

$$y_i^{(k)}(t) = \sum_{m=M_0}^{M_1} \sum_{n=0}^{N(m)} \chi_{n,m} \, a_d^{m/2} \, s_i^{(k)}(a_d^m t - n/W),$$

and $w(t)$ is assumed to be additive white Gaussian noise. The correlation between
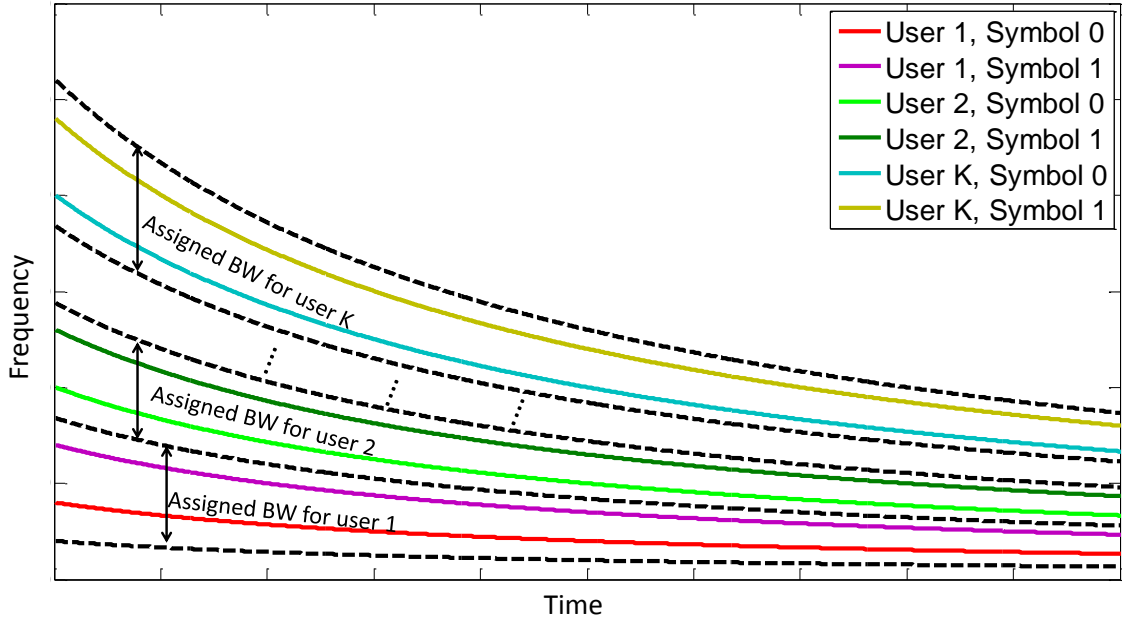
Figure 6.5: Time-Frequency Division for Different Users Using HFM.

the received signal and the expected signal is given by

$$\Lambda(y_i^{(k)}) = \int_{-\infty}^{\infty} r(t)\, y_i^{*(k)}(t)\, dt$$

$$= \sum_{m=M_0}^{M_1} \sum_{n=0}^{N(m)} \chi_{n,m}\, a_d^{m/2} \int_{-\infty}^{\infty} r(t)\, s_i^k\left(a_d^m t - \frac{n}{W}\right)\, dt$$

The information symbol of the kth user can then be estimated using

$$\hat{i} = \arg\max_{i=0,1}\ \Lambda(y_i^{(k)})\,.$$

The block diagram for the multi-user communication system using HFM can be seen in Figure 6.6.

6.3 Simulation Results

In this section, we first provide numerical simulations and results for a single user communication system using the HFM scheme in Section 6.1, where HFM signals with different FM rate are used to represent different symbols. In addition, we
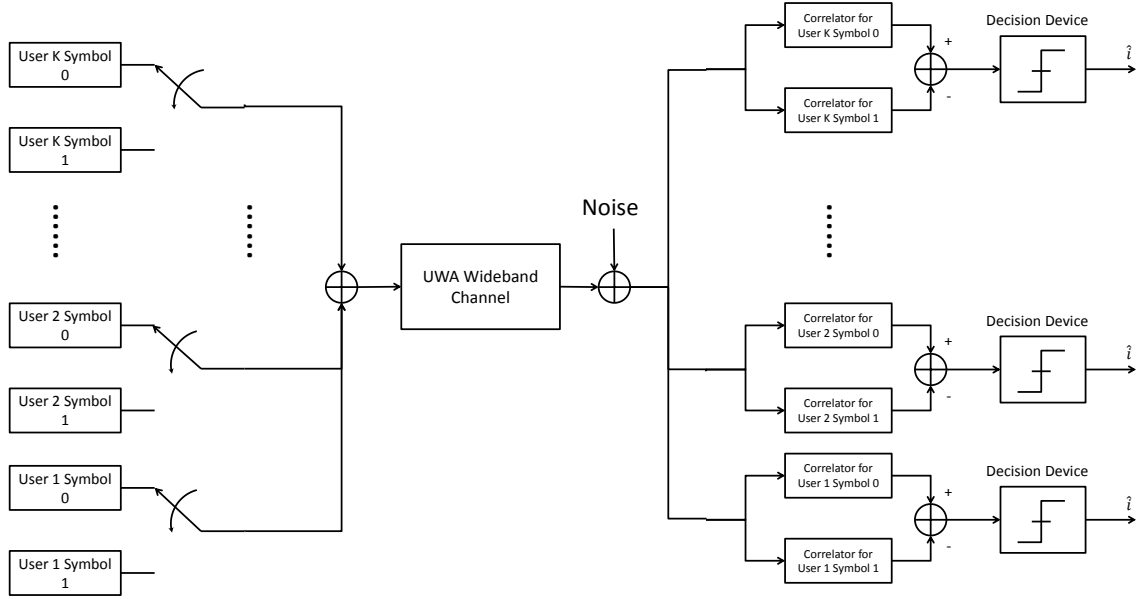
Figure 6.6: Block Diagram for Multi-User Underwater Communication System Using HFM.

combine this HFM signaling scheme with CDMA to achieve multi-user communications. Particularly different users are distinguished by different CDMA PN sequences. Moreover, we provide orthogonal HFM simulation results with minimized multi-user cross-correlation at the transmission side for a multi-user UWA communications system, and the bit error rate (BER) performance is compared to the HFM with CDMA method. At last, the overall multi-user UWA communications system performance is analyzed, after estimating the wideband UWA channel using training sequences, then the estimated channel coefficients are used to decode the transmitted bits.

6.3.1   HFM Signaling Scheme

In order to demonstrate the scale diversity using the HFM signaling scheme in UWA communications, we considered the following simulation example. We considered an HFM signal in Equation (6.1) with duration $T = 0.1$ s and 1.5 kHz maximum bandwidth. We assumed an UWA channel with $T_d = 10$ ms multipath spread, $\beta_d = 90$

Mellin spread resulting in $a_d = 1.011$, and $M_0 = 0$, $M_1 = 1$. Note that we assumed that the channel WSF coefficients were estimated at every iteration [47].

The user is assumed to transmit symbol 0 or 1 with equal probability. The HFM signals representing the two symbols differ by the value of the FM rates. We considered FM rates whose difference in values are given by $D_{0,1} = c_1 - c_0 = 0.1, 0.15, 0.5$. The simulation results of the BER for different signal-to-noise ratio (SNR) values (in dB) are shown in Figure 6.7. As expected from our derivations, scale diversity is achieved, and thus BER is reduced, as the chosen $D_{0,1}$ value is increased from 0.1 to 0.5.
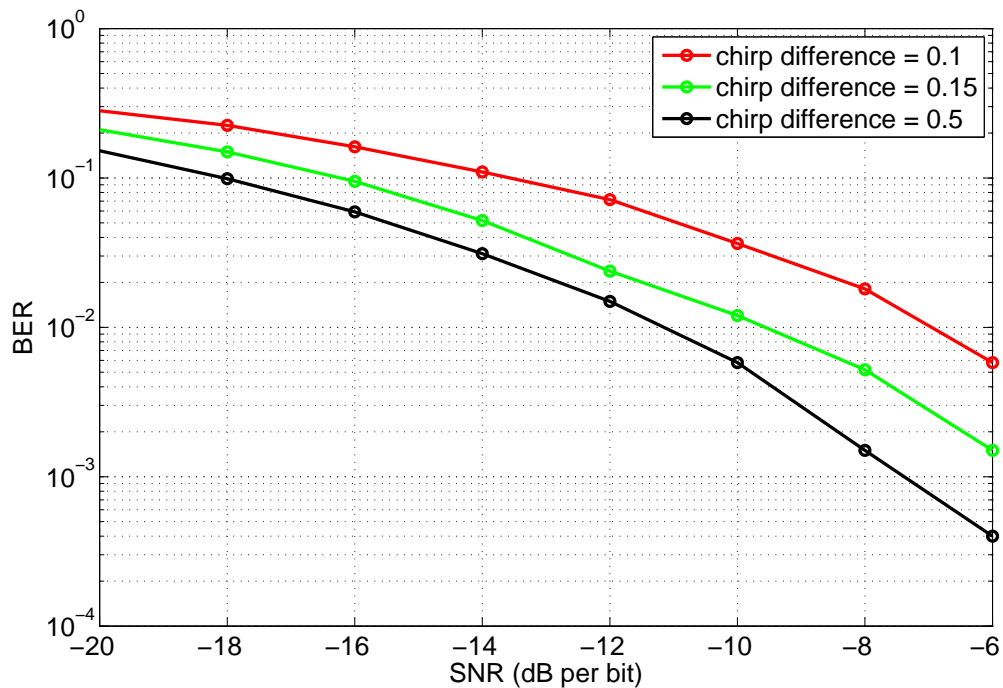
Figure 6.7: BER as A Function of SNR for Varying Chirp Rate Differences for Single User in An UWA Communications Channel.

6.3.2 CDMA with HFM Signaling

We demonstrated the use of HFM signaling for multi-user detection in the following simulation example, where PN sequences are used to distinguish between users. The HFM signals we used in this example have $T = 0.1$ s duration and 0.3 kHz maximum bandwidth. We generated PN sequences of length 7 using the M-sequence generator [99]. We assumed that the UWA communications channel characteristics are the same as in the previous simulation in Section 6.3.1. For each user, we considered the difference in FM rate to vary as $D_{0,1} = c_1 - c_0 = 0.1, 1, 3$. The simulated BERs (in dB) for different SNR values are shown in Figure 6.8. For comparison, we demonstrate the results for the case of $K = 2$ and $K = 4$ users. The scale diversity is better achieved when the difference in FM rate increases; this holds both for the single and multiuser cases.
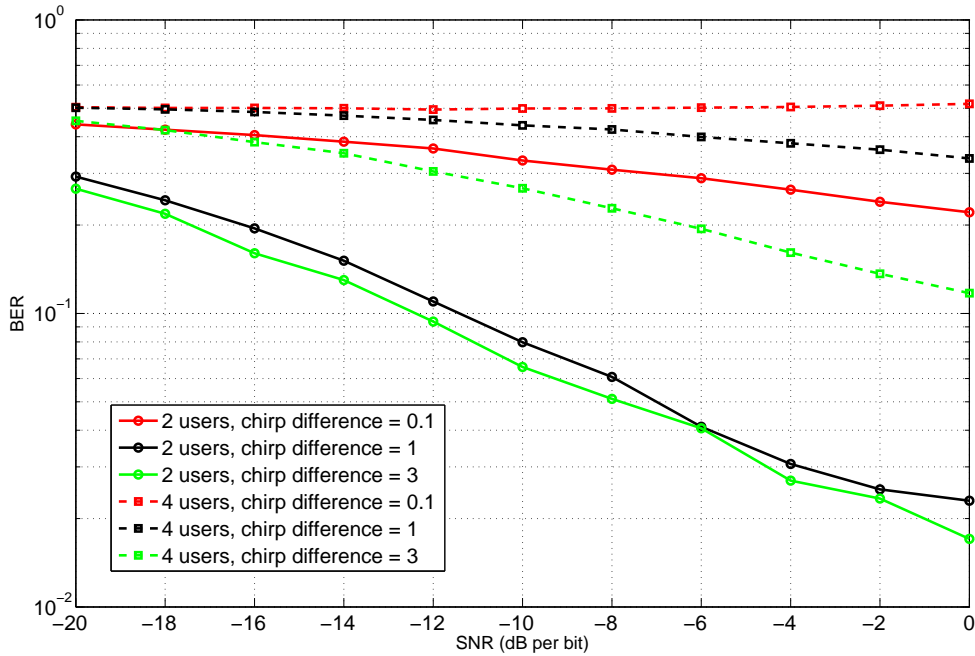
Figure 6.8: CDMA with HFM Signaling in An UWA Communications Channel Using $K = 2$ and $K = 4$ Users.
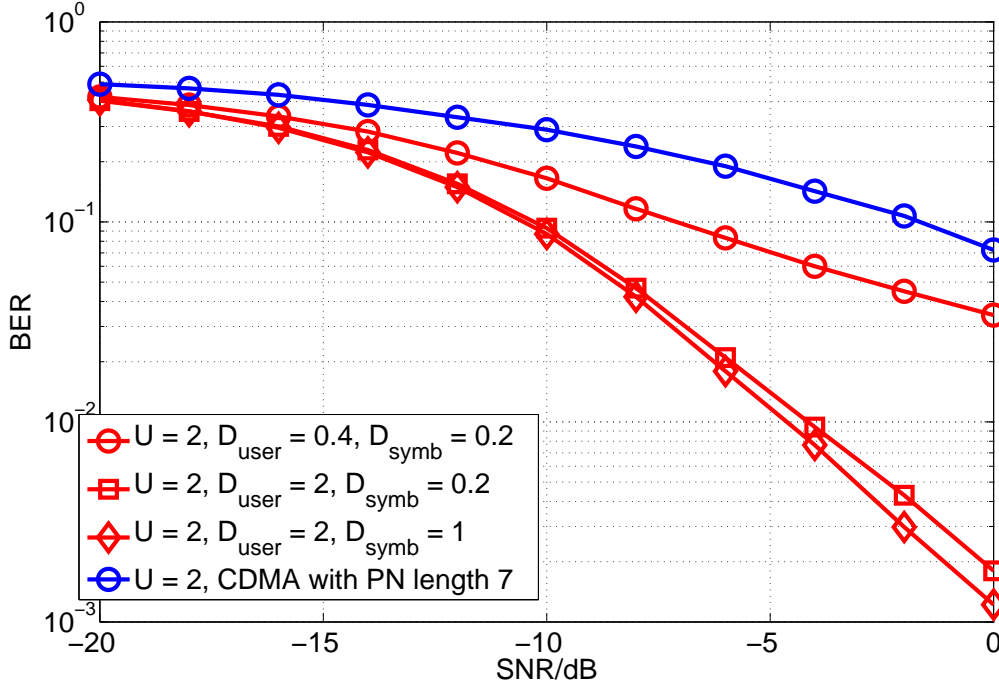
Figure 6.9: Comparison Between HFM with CDMA and New Signaling Scheme for Varying D_{symb} and D_{user} for $K = 2$ Users.

We demonstrate next the improved BER performance of the orthogonal HFM signaling scheme in multi-user UWA communications. We consider all possible HFM signals with duration $T = 0.1$ s and 5 kHz maximum bandwidth. Using the channel model in (5.2), we assume an UWA channel with $T_d = 10$ ms multipath spread, $\beta_d = 90$ Mellin spread resulting in $a_d = 1.011$, and $M_0 = 0$, $M_1 = 1$. Note that we assume that the channel WSF coefficients are estimated at every iteration [47]. All users are assumed to transmit symbol 0 or 1 with equal probability.

Using the HFM signal orthogonality condition in (6.15) to select FM rates for the two users to reduce MAI, we denote by $D_{\text{user}} = D_i^{k,j} = |c_i^k - c_i^j|$ the difference in the FM rates between the two users. Similarly, $D_{\text{symb}} = D_{i,l}^k = |c_i^k - c_l^k|$ denotes the difference in the FM rates between the two symbols of the kth user to reduce the
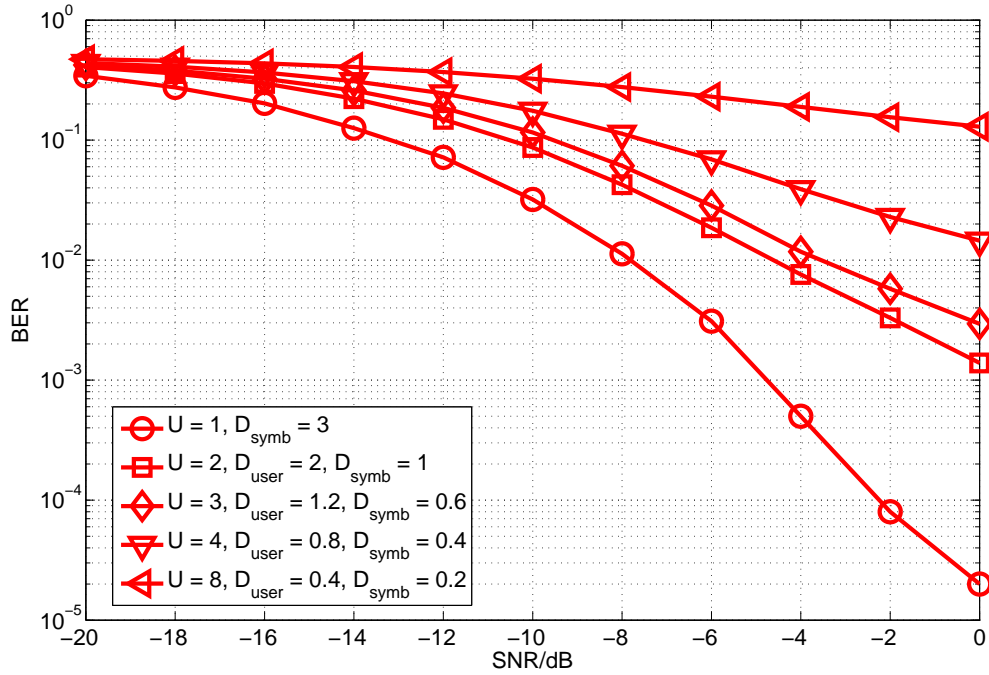
Figure 6.10: Comparison Between New Signaling Scheme for Different Number of Users, Where $K = 1, 2, 3, 4$ Users with The Best D_{symb} and D_{user} Are Chosen.

UWA channel effects (following the condition in (6.10)). Using this notation, for the 2 user case, we use HFM signals with FM rate difference $D_{\mathrm{symb}} = c_k^{(1)} - c_k^{(0)} = 0.25,\ 0.5$ for $k = 1, 2$ and $D_{\mathrm{user}} = c_1^{(i)} - c_2^{(i)} = 0.5,\ 1,\ 2$, for $i = 0, 1$. The BER simulation results for different signal-to-noise ratio (SNR) values (in dB) are shown in Figure 6.9. Also shown superimposed in the figure are the corresponding BER results obtained using the HFM with CDMA scheme discussed in Section 6.2.1 from [100]. The HFM with CDMA simulations used PN sequences of length 7 from the sequence generator [99]. As expected, as proposed HFM method performs better than the HFM with CDMA. This is because two different types of conditions are imposed when selecting the FM rates of the HFM signals. Note that the BER performance increases as the symbol FM rate difference D_{symb} and the user FM rate difference D_{user} increase.

In Figure 6.10, we extend our simulations to $K = 1, 2, 3, 4$ users, demonstrating

simulated BERs for different SNR values. The UWA channel parameters and the HFM signal parameters remain the same as in the first figure. For these cases, for each value of K, we selected D_{symb} and D_{user} to satisfy both conditions (6.10) and (6.15) for the given time-bandwidth product of $T = 0.1$ and 5 kHz maximum bandwidth. It can be observed that the BER performance decreases as the number of users increases.

6.4 Multi-User UWA Communication with Channel Estimation

In this section, the overall multi-user communication system performance is analyzed. It is assumed that the channel is first estimated by using training sequences, and the estimated channel is used to decode the transmitted information bits. The BER performance in terms of SNR and number of users are plotted in Figure 6.11.
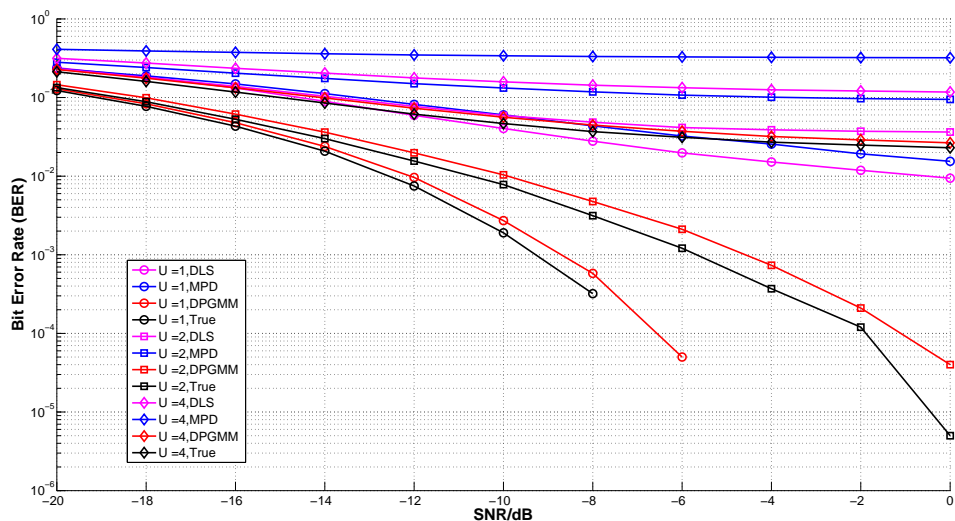
Figure 6.11: Comparison of Multi-User BER Performance of Given True and Estimated WSF Coefficients, Where $K = 1, 2, 4$ Users with The Best D_{symb} and D_{user} Are Chosen, and The Channel Coefficients Are Estimated by Using Direct Least Square, MPD and DP-LS Algorithm.

In Figure 6.11, the black lines represent the BER performance using the true channel coefficients, the red lines represent the BER performance using the WSF coefficients estimated by new proposed adaptive channel estimation algorithm in Sec-

tion 5.3, the blue lines represent the BER performance using the WSF coefficients estimated by MPD algorithm, and the purple lines represent the BER performance using the WSF coefficients estimated by using the direct least-square (DLS) algorithm. As it can be seen from Figure 6.11, the overall performance decreases as the total number of users increases, and for a fixed number of users, the BER performance is highest when the adaptive clustering method is used; in this example, the DLS method performed better than the MPD.

Chapter 7

CONCLUSION AND FUTURE DIRECTIONS

This thesis proposed new statistical processing algorithms for improving the detection and estimation performance of multiple objects in two current applications: tracking multiple radar targets in urban environments and underwater acoustic (UWA) communications for multiple users.

7.1   Conclusion

For tracking in urban environments, we proposed a multiple target tracking algorithm for tracking time-varying number of targets in urban environments where one target may generate more than one measurement due to multipath reflections. We used the probability hypothesis density (PHD) filter, implemented using a particle filter (PF), to track multiple targets without requiring the computation of measurement-to-track associations. We then modified the PF-PHD to incorporate multipath-to-measurement association as the different measurements from different received paths are characterized by different models. Instead of propagating the likelihood probability at each scan, the proposed algorithm uses the path likelihood probability obtained by maximizing all possible path likelihoods. In addition, since a single target state model cannot describe all possible target kinematic models, we used the interactive multiple model approach to allow for targets moving at constant velocity as well as maneuvering targets. We have also adapted the k-means clustering algorithm to estimate both the number of target as well as their corresponding states at the end of each time step. Using a test urban environment, we derived the measurement models for different regions, based on their location with respect to the target and the radar.

112

Specifically, we derived models for line-of-sight (LOS) only measurements, measurements with multiple multipaths, and combinations of these two measurements. We have also considered a clutter model for urban environments, and we incorporated it into the PD-PHD-MMA approach. At last, The performance of the proposed algorithm was demonstrated using simulations for the test urban environment for both a fixed number and a time-varying number of targets.

For wideband UWA communications, we first proposed an algorithm for estimating both the UWA channel spread time delay spread and Doppler scaling spread as well as the wideband spreading function (WSF) coefficients. The proposed adaptive clustering estimation algorithm integrates adaptive clustering with direct least-squares (DLS) estimation and matching pursuit decomposition (MPD) feature extraction to improve the estimation performance when compared to either the DLS or MPD approaches. In addition, we have shown a matching signaling scheme is presented to exploit the inherent diversity of the UWA communication channel. We first considered the time scale canonical representation of wideband linear time-varying channels and their inherent joint multipath-scale diversity. We then designed a signaling scheme, using hyperbolic frequency modulated signals, which is matched to this canonical representation. In particular, we derived conditions on the FM rates for representing different information symbols. Combined with CDMA, the signaling scheme was extended to multiple users and demonstrated better BER performance. Furthermore, we extended our signaling scheme to multi-user communications using hyperbolic frequency modulated signals. In particular, another condition is derived to minimize the multiple access interference.

7.2 Future Directions

For the urban multiple target tracking, the future research directions can be following.

- In order to further improve the performance of the PF-PHD-MMA algorithm, we can make use of the path likelihood functions for all possible measurement-to-path associations instead of selecting only the maximum one. As this modification can be computationally intensive, we need to determine trade-offs between tracking performance and computational complexity.

- The electro-optical (EO) sensor can be added into the tracking algorithm to improve the tracking accuracy. The EO sensor and RF sensor can be dependent, then the embedded exponential family (EEF) approach can be used to calculate the joint likelihood probality.

For the underwater acoustic communication, some future research directions include the following.

- The communication through shallow dispersive channel can be analyzed, and the performance can be compared to the wideband channel. The dispersive channel model is proportional to the communication depth, thus by estimating channel parameters, we can extract the depth information.

- For the wideband UWA channel, the received signal contains all possible paths including LOS or multipath reflections. It has been shown that different signal paths can be associated to unique Doppler scale and time shift combinations. After the UWA channel support estimation, the classified path groups can be filtered, in order to only keep paths with useful information. This is expected to improve the overall tracking performance for multiple targets.

114

REFERENCES

[1] B. Chakraborty, J. J. Zhang, A. Papandreou-Suppappola, and D. Morrell, "Urban terrain tracking in high clutter with waveform-agility," in *IEEE International Conference on Acoustics, Speech and Signal Processing*, May 2011, pp. 3640–3643.

[2] Y. Bar-Shalom and T. E. Fortman, *Tracking and Data Association*. Academic Press, New York, 1998.

[3] B. Ristic, S. Arulampalam, and N. Gordon, *Beyond the Kalman Filter: Particle Filters for Tracking Applications*. Boston: Artech, 2004.

[4] E. J. Baranoski, "Urban operations, the new frontier for radar," in *in Proceedings of the 24th DARPA Systems and Technology Symposium*, Anaheim, CA, USA, August 2005, pp. 155–159.

[5] C. Gierull, "Statistical analysis of multilook SAR interferograms for CFAR detection of ground moving targets," *IEEE Transactions on Geoscience and Remote Sensing*, vol. 42, no. 4, pp. 691–701, April 2004.

[6] D. Musicki and S. Suvorova, "Tracking in clutter using IMM-IPDA-based algorithms," *IEEE Transactions on Aerospace and Electronic Systems*, vol. 44, no. 1, pp. 111–126, January 2008.

[7] D. Musicki and B. La Scala, "Multi-target tracking in clutter without measurement assignment," *IEEE Transactions on Aerospace and Electronic Systems,*, vol. 44, no. 3, pp. 877–896, July 2008.

[8] S. P. Sira, A. Papandreou-Suppappola, and D. Morrell, "Dynamic configuration of time-varying waveforms for agile sensing and tracking in clutter," *IEEE Transactions on Signal Processing*, vol. 55, no. 7, pp. 3207–3217, July 2007.

[9] Y. Li, S. P. Sira, A. Papandreou-Suppappola, D. Cochran, and L. Scharf, *Maximizing Detection Performance with Waveform Design for Sensing in Heavy Sea Clutter*. IEEE/SP 14th Workshop on Statistical Signal Processing,, Aug 2007.

[10] Y. Li, W. Moran, S. P. Sira, A. Papandreou-Suppappola, and D. Morrell, "Adaptive waveform design in rapidly-varying radar scenes," in *2009 International Waveform Diversity and Design Conference*, February 2009, pp. 263–267.

[11] S. Blackman, *Multiple Target Tracking with Radar Applications*. Boston: Artech, 1986.

[12] R. Singer, "Estimating optimal tracking filter performance for manned maneuvering targets," *IEEE Transactions on Aerospace and Electronic SystemsShalom*, vol. AES-6, no. 4, pp. 473–483, July 1970.

[13] Y. Bar-Shalom, F. Daum, and J. Huang, "The probabilistic data association filter," *IEEE Control Systems*, vol. 29, no. 6, pp. 82–100, December 2009.

[14] T. Kirubarajan and Y. Bar-Shalom, "Probabilistic data association techniques for target tracking in clutter," *Proceedings of the IEEE*, vol. 92, no. 3, pp. 536–557, March 2004.

[15] T. E. Fortmann, Y. Bar-Shalom, and M. Scheffe, "Sonar tracking of multiple targets using joint probabilistic data association," *IEEE Journal of Oceanic Engineering*, vol. 8, no. 3, pp. 173–184, July 1983.

[16] S. Blackman and R. Popoli, *Design and Analysis of Modern Tracking Systems*, Norwood, Ed. Artech House, 1999.

[17] I. Goodman, R. P. Mahler, and H. T. Nguyen, *Mathematics of Data Fusion*, 1st ed. Springer, 1997.

[18] R. Mahler, "An introduction to multisource-multitarget statistics and its applications," Lockheed Martin, Technical Monograph, 2000.

[19] R. P. Mahler, "Multitarget Bayes filtering via first-order multitarget moments," *IEEE Transactions on Aerospace and Electronic Systems*, vol. 39, no. 4, pp. 1152–1178, October 2003.

[20] M. Canaud, L. Mihaylova, N. Faouzi, R. Billot, and J. Sau, "A probabilistic hypothesis density filter for traffic flow estimation in the presence of clutter," in *7th Workshop on Sensor Data Fusion: Trends, Solutions, Applications*, September 2012, pp. 31–36.

[21] R. Prasanth and H. Hoang, "Probability hypothesis density tracking for interacting vehicles in traffic," in *Signal Processing, Sensor Fusion, and Target Recognition XXI*, vol. 8392, 2012.

[22] R. Mahler, "Urban multitarget tracking via gas-kinetic dynamics models," in *Signal Processing, Sensor Fusion, and Target Recognition XXII*, vol. 8745, 2013.

[23] A. Jakubiak, "Modelling and simulation of urban multipath propagation," in *15th International Conference on Microwaves, Radar, and Wireless Communications*, vol. 3, May 2004, pp. 1013–1015.

[24] P. Closas, C. Fernandez-Prades, and J. Fernandez-Rubio, "Bayesian dll for multipath mitigation in navigation systems using particle filters," in *IEEE International Conference on Acoustics, Speech and Signal Processing*, no. 4, May 2006.

[25] B. Krach, M. Lentmaier, and P. Robertson, "Joint Bayesian positioning and multipath mitigation in GNSS," in *IEEE International Conference on Acoustics, Speech and Signal Processing*, March 2008, pp. 3437–3440.

[26] B. D. Rigling, "Urban RF multipath mitigation," in *IET Radar, Sonar and Navigation*, vol. 2, no. 6, December 2008, pp. 419–425.

[27] B. Krach and R.Weigel, "Markovian channel modeling for multipath mitigation in navigation receivers," in *3rd European Conference on Antennas and Propagation*, March 2009, pp. 1441–1445.

[28] J. Krolik, J. Farrell, and A. Steinhardt, "Exploiting multipath propagation for GMTI in urban environments," in *IEEE Conference on Radar*, April 2006, pp. 65–68.

[29] [Online]. Available: http://www.darpa.mil/STO/solicitations/baa09-01/presentations/MER Industry Day.pdf

[30] M. Mertens and M. Ulmke, "Precision GMTI tracking using road constraints with visibility information and a refined sensor model," in *IEEE Radar Conference*, May 2008, pp. 1–6.

[31] A. Goldsmith, *Wireless Communications.* New York, NY, USA: Cambridge University Press, 2005.

[32] I. Koffman and V. Roman, "Broadband wireless access solutions based on ofdm access in ieee 802.16," *IEEE on Communications Magazine*, vol. 40, no. 4, pp. 96–103, April 2002.

[33] B. Li, S. Zhou, M. Stojanovic, L. Freitag, and P. Willett, "Non-uniform Doppler compensation for zero-padded OFDM over fast-varying underwater acoustic channels," in *OCEANS Europe*, 2007, pp. 1–6.

[34] K. Tu, T. M. Duman, M. Stojanovic, and J. G. Proakis, "Multiple-resampling receiver design for OFDM over Doppler-distorted underwater acoustic channels," *IEEE Journal of Oceanic Engineering*, vol. 38, no. 2, pp. 333–346, 2013.

[35] E. Calvo and M. Stojanovic, "Efficient channel-estimation-based multiuser detection for underwater CDMA systems," *IEEE Journal of Oceanic Engineering*, vol. 33, no. 4, pp. 502–512, 2008.

[36] S. A. Aliesawi, C. C. Tsimenidis, B. S. Sharif, and M. Johnston, "Iterative multiuser detection for underwater acoustic channels," *IEEE Journal of Oceanic Engineering*, vol. 36, no. 4, pp. 728–744, 2011.

[37] L. Zhang, X. Xu, W. Feng, and Y. Chen, "HFM spread spectrum modulation scheme in shallow water acoustic channels," in *MTS/IEEE OCEANS Conference*, 2012, pp. 1–6.

[38] S. Machineni, H. Shen, and A. Papandreou-Suppappola, "Multi-user schemes using nonlinear time-varying modulation," in *IEEE International Conference on Acoustics, Speech, and Signal Processing*, Montreal, Canada, May 2004, pp. 941–944.

[39] C. Gupta, T. Mumtaz, M. Zaman, and A. Papandreou-Suppappola, "Wideband chirp modulation for FH-CDMA wireless systems: coherent and non-coherent receiver structures," *IEEE International Conference on Communications*, vol. 4, pp. 2455–2459, 2003.

117

[40] A. Kocian and D. Dahlhaus, "Downlink performance analysis of a CDMA mobile radio system with chirp modulation," *IEEE Vehicular Technology Conference*, vol. 1, pp. 238–242, 1999.

[41] H. Liu, "Multicode ultra-wideband scheme using chirp waveforms," *IEEE Journal on Selected Areas in Communications*, vol. 24, pp. 885–891, 2006.

[42] M. A. Khan, R. K. Rao, and X. Wang, "Performance of multiuser MIMO communication system using chirp modulation," in *International Symposium on Performance Evaluation of Computer and Telecommunication Systems*, 2013, pp. 115–119.

[43] G. Griffiths, *Technology and Applications of Autonomous Underwater Vehicles*, ser. (Ocean Science and Technology).   Taylor & Francis, 2002.

[44] Y. Xiao, *Underwater Acoustic Sensor Networks*, 1st ed.   Boston, MA, USA: Auerbach Publications, 2009.

[45] M. Stojanovic and J. Preisig, "Underwater acoustic communication channels: Propagation models and statistical characterization," *IEEE Communications Magazine*, vol. 47, no. 1, pp. 84–89, 2009.

[46] N. F. Josso, J. J. Zhang, D. Fertonani, A. Papandreou-Suppappola, and T. M. Duman, "Time-varying wideband underwater acoustic channel estimation for OFDM communications," in *IEEE International Conference on Acoustics Speech and Signal Processing*, 2010, pp. 5626–5629.

[47] N. F. Josso, J. J. Zhang, A. Papandreou-Suppappola, C. Ioana, and T. M. Duman, "Nonstationary system analysis methods for underwater communications," *EURASIP Journal on Advances in Signal Processsing*, vol. 11, 2011.

[48] Y. Jiang and A. Papandreou-Suppappola, "Discrete time-scale characterization of wideband time-varying systems," *IEEE Transactions on Signal Processing*, vol. 54, no. 4, pp. 1364–1375, 2006.

[49] ——, "Discrete time-frequency characterizations of dispersive linear time-varying systems," *IEEE Transactions on Signal Processing*, vol. 55, no. 5, pp. 2066–2076, May 2007.

[50] J. Zhang, A. Papandreou-Suppappola, B. Gottin, and C. Ioana, "Time-frequency characterization and receiver waveform design for shallow water environments," *IEEE Transactions on Signal Processing*, vol. 57, no. 8, pp. 2973–2985, August 2009.

[51] B. Ristic, B.-N. Vo, D. Clark, and B.-T. Vo, "A metric for performance evaluation of multi-target tracking algorithms," in *IEEE Transactions on Signal Processing*, vol. 59, no. 7, July 2011, pp. 3452–3457.

[52] P. Bello, "Characterization of randomly time-variant linear channels," *IEEE Transactions on Communications Systems*, vol. 11, no. 4, pp. 360–393, December 1963.

[53] R. S. Kennedy, *Fading Dispersive Communication Channels.* John Wiley and Sons, Inc, 1969.

[54] L. A. Zadeh, "Frequency analysis of variable networks," *Proceedings of IRE*, vol. 38, March 1950.

[55] L. J. Ziomek, *Underwater Acoustics: A Linear Systems Theory Approach.* Academic Press, 1985.

[56] G. B. Folland, *Harmonic Analysis in Phase Space.* Univerity Press, 1989.

[57] W. Kozek, "Time-frequency representation of linear time-varying systems using the Weyl symbol," *Proceedings of 6th International Conference on Digital Signal Processing of Signals in Communications*, pp. 25–30, Sepember 1991.

[58] ——, "On the generalized Weyl correspondence and its application to time-frequency analysis of linear time-varying systems," in *Proceedings of the IEEE-SP International Symposium Time-Frequency and Time-Scale Analysis*, October 1992, pp. 167–170.

[59] R. Shenoy and T. Parks, "The Weyl correspondence and time-frequency analysis," *IEEE Transactions on Signal Processing*, vol. 42, no. 2, pp. 318–331, February 1994.

[60] D. E. Vakman, *Sophisticated Signals and the Uncertainty Principle in Radar.* New York: Springer-Verlag, 1968.

[61] W. Kozek and A. Molisch, "Nonorthogonal pulseshapes for multicarrier communications in doubly dispersive channels," *IEEE Journal on Selected Areas in Communications*, vol. 16, no. 8, pp. 1579–1589, October 1998.

[62] H. Bolcskei, P. Duhamel, and R. Hleiss, "Design of pulse shaping OFDM/OQAM system for high data-rate transmission over wireless channels," *Proceedings of International Conference on Communications*, pp. 559–564, June 1999.

[63] R. Haas and J. Belefiore, "A time-frequency well-localized pulse for multiple carrier transmission," *Wireless Personal Communications*, vol. 5, pp. 1–18, 1997.

[64] A. M. Sayeed and B. Aazhang, "Communication over multipath fading channels: A time-frequency perspective," in *Wireless Communications: TDMA Versus CDMA.* Kluwer academic publishers, 1997, pp. 73–98.

[65] A. Papandreou-Suppappola, *Time-frequency processing: A tutorial on principles and practice*, A. papandreou-suppappola ed. Boca Raton, FL: CRC Press, January 2002.

[66] T. J. Sutton, H. Griffiths, A. Hetet, Y. Perrot, and S. A. Chapman, "Experimental validation of autofocus algorithms for high-resolution imaging of the seabed using synthetic aperture sonar," *IEE Proceedings of Radar, Sonar and Navigation*, vol. 150, no. 2, pp. 78–83, April 2003.

[67] L. G. Weiss, "Time-varying system characterization for wideband input signals," *Signal Processing*, vol. 55, pp. 295–304, 1996.

[68] L. Sibul, M. Roan, and K. Hillsley, "Wavelet transform techniques for time varying propagation and scattering characterization," in *Thirty-Second Asilomar Conference on Signals, Systems and Computers*, vol. 2, November 1998, pp. 1644–1649.

[69] M. Stojanovic, "Recent advances in high-speed underwater acoustic communications," *IEEE Journal of Oceanic Engineering*, vol. 21, no. 2, pp. 125–136, April 1996.

[70] B. Sharif, J. Neasham, O. Hinton, and A. Adams, "A computationally efficient Doppler compensation system for underwater acoustic communications," *IEEE Journal of Oceanic Engineering*, vol. 25, no. 1, pp. 52–61, January 2000.

[71] D. Iverson, "Coherent processing of ultra-wideband radar signals," *IEE Proceedings of Radar, Sonar and Navigation*, vol. 141, no. 3, pp. 171–179, June 1994.

[72] N. Felix, L. Ratsimandresy, and L. Dufait, "High bandwidth, high density arrays for advanced ultrasound imaging," in *IEEE Ultrasonics Symposium*, vol. 2, 2001, pp. 1123–1126.

[73] B. S. Krongold, A. Sayeed, M. Moehring, J. Ritcey, M. Spencer, and D. Jones, "Time-scale detection of microemboli in flowing blood with doppler ultrasound," *IEEE Transactions on Biomedical Engineering*, vol. 46, no. 9, pp. 1081–1089, September 1999.

[74] B. G. Iem, *Generalization of the Weyl Symbol and the Spreading Function via timefrequency warpings: Theory and application*. Ph.D. dissertation, University of Rhode Island, 1998.

[75] J. Proakis and M. Salehi, *Digital Communications*. McGraw-Hill Education, 2007.

[76] U. Soergel, K. Schulz, U. Thoennessen, and U. Stilla, "Determination of optimal SAR illumination aspects in build-up areas," in *Proceedings of IEEE Geoscience and Remote Sensing Symposium*, vol. 6, July 2003, pp. 3662–3664.

[77] W. Lee, "Analytical investigation of urban SAR features having a group of corner reflectors," vol. 3, pp. 1282–1284, 2001.

[78] J. Krolik, J. Farrell, and A. Steinhardt, "Exploiting multipath propagation for GMTI in urban environments," in *IEEE Conference on Radar*, April 2006, p. 4.

[79] D. Schuhmacher, B. T. Vo, and B. N. Vo, "A consistent metric for performance evaluation of multi-object filters," *IEEE Transactions on Signal Processing*, vol. 58, no. 8, pp. 3447–3457, Aug. 2008.

[80] S. Mallat and Z. Zhang, "Matching pursuits with time-frequency dictionaries," *IEEE Transactions on Signal Processing*, vol. 41, no. 12, pp. 3397–3415, December 1993.

[81] A. Papandreou-Suppappola and S. Suppappola, "Analysis and classification of time-varying signals with multiple time-frequency structures," *IEEE Signal Processing Letters*, vol. 9, no. 3, pp. 92–95, March 2002.

[82] K. Ni, Y. Qi, and L. Carin, "Multiaspect target detection via the infinite hidden Markov model," *Journal of the Acoustical Society of America*, vol. 121, pp. 2731–2742, 2007.

[83] Y. Qi, J. W. Paisley, and L. Carin, "Music analysis using hidden Markov mixture models," *IEEE Transactions on Signal Processing*, vol. 55, pp. 5209–5224, 2007.

[84] D. Ting, G. Wang, M. Shapovalov, R. Mitra, M. I. Jordan, and R. L. D. Jr., "Neighbor-dependent Ramachandran probability distributions of amino acids developed from a hierarchical Dirichlet process model," *PLoS Computational Biology*, vol. 6, 2010.

[85] E. B. Fox, E. B. Sudderth, M. I. Jordan, and A. S. Willsky, "A sticky HDPHMM with application to speaker diarization," *Annals of Applied Statistics*, vol. 5, pp. 1020–1056, 2011.

[86] D. Young, "An overview of mixture models," *Statistics Surveys*, pp. 1–24, 2008.

[87] D. Gorur and C. Rasmussen, "Dirichlet process Gaussian mixture models: choice of base distribution," *Journal of Computer Science and Technology*, vol. 25, pp. 615–626, 2010.

[88] M. D. Escobar and M. West, "Bayesian density estimation and interference using mixtures," *Journal of the American Statistical Association*, vol. 96, pp. 577–588, 1995.

[89] M. Jordan, "Bayesian nonparametric learning: Expressive priors for intelligent systems," *Heuristics, Probability and Causality: A Tribute to Judea Pearl*, pp. 167–186, 2010.

[90] J. Sethuraman, "A constructive definition of Dirichlet priors," *Statistica Sinica*, vol. 4, pp. 639–650, 1994.

[91] T. S. Ferguson, "A Bayesian analysis of some nonparametric problems," *The Annals of Statistics*, vol. 1, pp. 209–230, 1973.

[92] D. Blackwell and J. B. MacQueen, "Ferguson distributions via polya urn schemes," *The Annals of Statistics*, vol. 1, pp. 353–355, 1973.

[93] C. E. Antoniak, "Mixtures of Dirichlet processes with applications to Bayesian nonparametric problems," *The Annals of Statistics*, vol. 2, pp. 1152–1174, 1974.

[94] M. West, P. Muller, and M. D. Escobar, *Hierarchical priors and mixture models, with applications in regression and density estimation*, P. R. freeman and A. F. smith ed. John Wiley, 1994.

[95] W. R. Gilks, S. Richardson, and D. J. Spiegelhalter, *Markov Chain Monte Carlo in Practice*. CRC press, 1996, vol. 2.

[96] H. Ishwaran and L. F. James, "Gibbs sampling methods for stick-breaking priors," *Journal of the American Statistical Association*, vol. 96, pp. 161–173, 2001.

[97] R. A. Altes and E. L. Titlebaum, "Bat signals as optimally Doppler tolerant waveforms," *Journal of the Acoustical Society of America*, vol. 48, October 1970.

[98] A. Papandreou-Suppappola, "Time-varying processing: Tutorial on principles and practice," in *Applications in Time-Frequency Signal Processing*, A. Papandreou-Suppappola, Ed. CRC Press, 2002, pp. 1–84.

[99] S. W. Golomb, *Shift Register Sequences*. Holden-Day, Inc., 1967.

[100] M. Zhou, J. Zhang, A. Papandreou-Suppappola, and T. Duman, "An underwater acoustic communications scheme with inherent scale diversity for multiple users," in *MTS/IEEE OCEANS Conference*, September 2013.